

Respiratory Motion-Compensation in ^{82}Rb Cardiac PET/CT

by

Amir Pourmoghaddas, B.Sc.

A Thesis Submitted to
the Faculty of Graduate Studies and Research
in Partial Fulfillment of
the Requirements for the Degree of
Master of Science

Ottawa-Carleton Institute for Physics
Department of Physics, Carleton University
Ottawa, Ontario, Canada

Copyright © Amir Pourmoghaddas 2010



Library and Archives
Canada

Published Heritage
Branch

395 Wellington Street
Ottawa ON K1A 0N4
Canada

Bibliothèque et
Archives Canada

Direction du
Patrimoine de l'édition

395, rue Wellington
Ottawa ON K1A 0N4
Canada

Your file *Votre référence*
ISBN: 978-0-494-64432-4
Our file *Notre référence*
ISBN: 978-0-494-64432-4

NOTICE:

The author has granted a non-exclusive license allowing Library and Archives Canada to reproduce, publish, archive, preserve, conserve, communicate to the public by telecommunication or on the Internet, loan, distribute and sell theses worldwide, for commercial or non-commercial purposes, in microform, paper, electronic and/or any other formats.

The author retains copyright ownership and moral rights in this thesis. Neither the thesis nor substantial extracts from it may be printed or otherwise reproduced without the author's permission.

AVIS:

L'auteur a accordé une licence non exclusive permettant à la Bibliothèque et Archives Canada de reproduire, publier, archiver, sauvegarder, conserver, transmettre au public par télécommunication ou par l'Internet, prêter, distribuer et vendre des thèses partout dans le monde, à des fins commerciales ou autres, sur support microforme, papier, électronique et/ou autres formats.

L'auteur conserve la propriété du droit d'auteur et des droits moraux qui protègent cette thèse. Ni la thèse ni des extraits substantiels de celle-ci ne doivent être imprimés ou autrement reproduits sans son autorisation.

In compliance with the Canadian Privacy Act some supporting forms may have been removed from this thesis.

While these forms may be included in the document page count, their removal does not represent any loss of content from the thesis.

Conformément à la loi canadienne sur la protection de la vie privée, quelques formulaires secondaires ont été enlevés de cette thèse.

Bien que ces formulaires aient inclus dans la pagination, il n'y aura aucun contenu manquant.


Canada

Abstract

PET is the gold standard for measuring myocardial perfusion in vivo. CT scans provide fast low-noise transmission maps for attenuation correction. However, single CT scans only capture a short portion of the respiratory cycle while the PET image corresponds to an average over multiple respiratory cycles. The misalignment caused by this difference leads to artifacts in the attenuation corrected image. Additionally, respiratory motion of the heart degrades image quality by blurring the acquired counts over the path of movement.

Motion blurring can be reduced through respiratory gating, which sorts the acquired counts according to the phase of the respiratory cycle. In this work, automated methods are introduced for realignment of gated emission images, and show feasibility for improving image characteristics of normal and abnormal studies. The combined effect of accurate attenuation correction approaches and respiratory phase alignment is evaluated in a series of simulated and live-subject experiments.

Acknowledgements

I would like to express my sincere gratitude to my advisor Dr. R. Glenn Wells for his exemplary mentorship and constant support throughout my research. I have learned a great deal from him, and physics is only the beginning. I also would like to thank Dr. Joanna Cygler for her support and kindness.

I would like to thank Stephanie Thorn and the animal care group at the University of Ottawa Heart Institute for their help with the animal studies. I am also grateful to my fellow students in the Image Analysis group and employees at the Heart Institute whose companionship has made my experience here an enjoyable one.

This work is dedicated to my parents, Parvaneh and Hossein. Thank you for all your love and support. I owe any success in life to you.

Table of Contents

ABSTRACT.....	II
ACKNOWLEDGEMENTS.....	III
GLOSSARY OF ACRONYMS	V
LIST OF TABLES.....	VI
LIST OF FIGURES	VII
CHAPTER 1 INTRODUCTION	1
1.1 PROJECT OVERVIEW	1
1.2 THE PHYSICS OF PET.....	4
1.2.1 Positron Decay	4
1.2.2 Detection of Annihilation Photons	6
1.2.3 Classification of Detected Events.....	8
1.2.4 2D vs 3D Data Acquisition	10
1.3 DATA CORRECTION	12
1.3.1 Dead-time Correction.....	12
1.3.2 Normalization.....	12
1.3.3 Correction for Random Coincidences	14
1.3.4 Scatter Correction.....	14
1.3.5 Attenuation Correction.....	17
1.4 IMAGE RECONSTRUCTION	22
1.5 MODES OF ACQUISITIONS	25
1.5.1 Static Acquisitions	25
1.5.2 Dynamic Acquisitions	25
1.5.3 Gated Acquisitions	27
1.6 HEART ANATOMY.....	30
1.7 TRACER KINETICS.....	31
1.8 CT IMAGE ACQUISITION.....	37
1.9 RESPIRATORY MOTION ARTIFACTS	40
1.9.1 Errors in Attenuation Correction.....	41
1.9.2 Motion Blurring	44
1.10 THESIS OBJECTIVE.....	46
CHAPTER 2 MOTION COMPENSATION FOR RESPIRATORY-GATED ⁸²Rb-PET.....	49
2.1 SIMULATION STUDY.....	49
2.1.1 The NCAT phantom.....	50
2.1.2 SimSET Simulations	52
2.1.3 Respiratory phase alignment	54
2.1.4 Phase alignment accuracy	56
2.1.5 Results	59
2.1.6 Discussion	70
2.2 RESPIRATORY MOTION CORRECTION FOR SWINE CARDIAC PET/CT IMAGING.....	73
2.2.1 Methods.....	73
2.2.2 Results	76
2.2.3 Discussion	86
CHAPTER 3 IMPROVED MEASUREMENT OF DEFECT SIZE AND SEVERITY USING RESPIRATORY MOTION COMPENSATION IN CARDIAC PET/CT.....	90
3.1 METHODS.....	90
3.2 RESULTS.....	93
3.3 DISCUSSION.....	97
CHAPTER 4 CONCLUSIONS	100
References.....	104

Glossary of Acronyms

4DCT	4 Dimensional Computed Tomography
AC	Attenuation Correction
ACF	Attenuation Correction Factor
ASNC	American Society of Nuclear Cardiology
BGO	Bismuth Germinate
CAD	Coronary Artery Disease
CT	Computed Tomography
CTAC	CT-based Attenuation Correction
EF	Ejection Fraction
FBP	Filtered Backprojection
FOV	Field of View
FWHM	Full Width at Half Maximum
Ge	Germanium
GUI	Graphical User Interface
GSO	Germanium Oxyorthosilicate
keV	Kilo Electronvolt
LOR	Line of Response
LV	Left Ventricle
LYSO	Lutetium Yttrium Orthosilicate
MBF	Myocardial Blood Flow
MBq	Mega Becquerel
MC	Motion Compensation
mCi	Milli Curie
MeV	Mega Electronvolt
MLEM	Maximum-Likelihood Expectation Maximization
MPI	Myocardial Perfusion Imaging
MRI	Magnetic Resonance Imaging
NCAT	Nonuniform Nurbs-Based Cardiac Torso phantom
OSEM	Ordered Subsets Expectation Maximization
PET	Positron Emission Tomography
Rb	Rubidium
RMSE	Root Mean squared Error
SF	Scatter Fraction
SD	Standard Deviation
SMPE	Segmental Mean Percentage Error
SPS	Summed Perfusion Score
TAC	Time-Activity Curve
TBV	Total Blood Volume
UOHI	University of Ottawa Heart Institute

List of Tables

TABLE 1.1 COMMONLY-USED PET TRACERS AND THEIR USES [4].....	3
TABLE 1.2 DECAY CHARACTERISTICS FOR COMMONLY-USED PET RADIO-NUCLIDES [6].....	5
TABLE 3.1 SUMMED PERFUSION SCORES (SPS) FOR THE CLINICAL AND SIMULATED STUDIES BEFORE AND AFTER MOTION-CORRECTION.....	97
TABLE 3.2 DEFECT SIZE DIFFERENCE AS A PERCENTAGE OF THE MOTION-FREE DEFECT SIZE, BEFORE AND AFTER MOTION-CORRECTION.....	97

List of Figures

FIGURE 1.1 A SCHEMATIC ILLUSTRATION OF THE DATA ACQUISITION PROCESS IN PET IMAGING. A POSITRON EMITTING RADIOACTIVE TRACER IS INJECTED INTO THE BODY AND FOLLOWS ITS BIOLOGICAL PATHWAY TO BE TAKEN UP IN AN ORGAN OF INTEREST. THE POSITRON TRAVELS A TWISTED PATH DUE TO THE INTERACTIONS WITH SURROUNDING MATTER AND FINALLY ANNIHILATES WITH AN ELECTRON AT REST, GIVING RISE TO TWO 511 KEV PHOTONS WHICH ARE DETECTED BY THE SCANNER VIA COINCIDENCE DETECTION.	7
FIGURE 1.2 A DIAGRAM SHOWING THE RELATIONSHIP BETWEEN AN LOR AND ITS CORRESPONDING ELEMENT IN THE SINOGRAM.....	8
FIGURE 1.3 ILLUSTRATION OF DIFFERENT COINCIDENCE EVENT TYPES IN PET IMAGING. A) TRUE COINCIDENCE, B) SCATTERED COINCIDENCE, C) MULTIPLE COINCIDENCE AND D) RANDOM COINCIDENCE. THE TRUE PATH IS SHOWN BY A SOLID LINE WHILE THE CORRESPONDING LOR IS SHOWN WITH A DASHED LINE.....	9
FIGURE 1.4 SCHEMATIC ILLUSTRATION OF AN ANNIHILATION EVENT OCCURING IN DEPTH x IN A MEDIUM WITH AN ATTENUATION COEFFICIENT OF M	18
FIGURE 1.5 TIME-ACTIVITY CURVES FOR ARTERIAL BLOOD AND DIFFERENT SECTIONS OF THE HEART ARE SHOWN. "CAVITY" REFERS TO THE ACTIVITY OF THE BLOOD INSIDE THE LEFT VENTRICLE (LV) OF THE HEART, "BASE" REFERS TO THE BASAL SECTION OF THE LV, THE MEDIAN ACTIVITY OF THE LEFT VENTRICULAR BLOOD IS ALSO SHOWN. "MYOCARDIUM" REFERS TO THE MUSCLE TISSUE OF THE LV.....	27
FIGURE 1.6 A: SCHEMATIC REPRESENTATION OF THE HEART. THE DASHED LINES REPRESENT THE AXES OF THE HEART WHILE THE SOLID LINES RELATE TO THE BODY AXES. B: A CROSS SECTIONAL SCHEMATIC OF THE LEFT AND RIGHT VENTRICLES, COMMONLY KNOWN AS THE "SHORT AXIS VIEW". C: VERTICLE LONG AXIS VIEW. D: HORIZONTAL LONG AXIS VIEW. HEART IMAGE WAS TAKEN FROM HTTP://WWW.NIAAA.NIH.GOV/ ...	31
FIGURE 1.7 THE ONE-COMPARTMENT MODEL USED FOR Rb PET BLOOD FLOW ANALYSIS. $C_1(t)$ AND $C_a(t)$ DENOTE THE MYOCARDIAL TISSUE AND ARTERIAL BLOOD RADIOACTIVITY CONCENTRATIONS RESPECTIVELY. K_1 AND K_2 REPRESENT THE INFLUX AND EFFLUX, INTO AND OUT OF THE MYOCARDIAL TISSUE [7].	32
FIGURE 1.8 A DIAGRAMMATIC REPRESENTATION OF THE SPILLOVER OF MEASURED ACTIVITY FROM THE MYOCARDIUM TO THE BLOOD AND VICE VERSA. (A) SHOWS SCHEMATICALLY A SHORT AXIS CUT THROUGH	

THE LV MYOCARDIUM (B) DEPICTS AN ACTIVITY PROFILE OF THE CROSS SECTION SHOWN IN (A). (C) SHOWS AN ACTIVITY PROFILE FROM THE SAME CROSS SECTION WHEN THE BLOOD ACTIVITY IS HIGH AND THE MYOCARDIAL TRACER UPTAKE IS LOW.34

FIGURE 1.9 POLAR MAP REPRESENTATION OF THE 3D SHAPE OF THE LV36

FIGURE 1.10 THE 17 SEGMENT MODEL37

FIGURE 1.11 4DCT IMAGE ACQUISITION PROCESS39

FIGURE 1.12 A: GOOD REGISTRATION BETWEEN PET/CT IMAGES RESULTING IN ACCURATE AC IN (C). B: SEVERE MISREGISTRATION BETWEEN PET/CT IMAGES. THE OVERLAPPING SECTIONS OF THE HEART AND LUNG IN THE FUSED IMAGE RESULTS IN A ARTIFACTUAL PERFUSION DEFECT SEEN IN THE ANTERIOR PORTION OF THE LV CAVITY (D).42

FIGURE 1.13 A CORONAL SLICE FROM A DIGITAL PHANTOM SIMULATING FUSED (OVERLAYED) PET/CT IMAGES. THE GRAYSCALE BACKGROUND REPRESENTS THE CT IMAGE WHILE THE COLORED CAVITY REPRESENTS THE PET IMAGE OF THE HEART. IMAGE (A) IS THE IDEALISTIC CASE WHERE NO MOTION-BLURRING IS SEEN AS A SNAPSHOT VIEW OF THE RESPIRATORY CYCLE IS CAPTURED. IMAGE (B) SHOWS THE EFFECT OF MOTION BLURRING.44

FIGURE 2.1 SIMULATION FLOW-CHART.49

FIGURE 2.2 TIME-ACTIVITY CURVES SHOWING THE IDEALIZED ACTIVITY DISTRIBUTION OF THE BLOOD AND HEART CAVITIES THAT ARE USED IN GENERATING THE PHANTOM51

FIGURE 2.3 A TRANSAXIAL SLICE FOLLOWED THROUGH NCAT ACTIVITY MAPS FOR EACH DYNAMIC FRAME, SHOWING THE RELATIVE ACTIVITY DISTRIBUTION IN THE MYOCARDIUM52

FIGURE 2.4 FIGURE 2.3 A TRANSAXIAL SLICE FOLLOWED THROUGH SIMULATED PET IMAGES SHOWING THE RELATIVE ACTIVITY DISTRIBUTION IN THE MYOCARDIUM IN EACH DYNAMIC FRAME.....53

FIGURE 2.5 A SAMPLE FROM THE REGISTRATION SOFTWARE SHOWING THE MYOCARDIUM (CLOCKWISE FROM TOP LEFT): TRANSAXIAL VIEW, VERTICAL LONG AXIS VIEW, SHORT AXIS VIEW AND THE HORIZONTAL LONG AXIS VIEW.55

FIGURE 2.6 LATERAL VIEWS OF FIVE RESPIRATORY FRAMES SHOWING FUSED (OVER-LAYED) EMISSION AND TRANSMISSION IMAGES. THE LV (SHOWN IN GOLD) SHOWS AXIAL TRANSLATION ACROSS THE FIVE RESPIRATORY FRAMES. LUNG INFLATION CAN ALSO BE SEEN FROM LEFT TO RIGHT.....56

FIGURE 2.7 TRANSVERSE AND CORONAL VIEWS OF 2 SUPER-IMPOSED HALF-ELLIPSOIDS GENERATED FOR PHASE ALIGNMENT ACCURACY TEST57

FIGURE 2.8 COORDINATES OF THE CENTER OF THE HALF-ELLIPSOIDS MEASURED BY THE FITTING ALGORITHMS. THE BLUE (SOLID) LINE SHOWS THE AVERAGE OF THE MEASURED DATA POINTS AND THE RED (DASHED) LINE REPRESENTS THE COORDINATES USED TO GENERATE THE HALF-ELLIPSOIDS.....58

FIGURE 2.9 BLAND-ALTMAN PLOTS FOR X, Y AND Z PIXEL COORDINATES OF THE MEASURED CENTER POSITIONS OF THE ELLIPSOIDS COMPARED TO THE EXPECTED POSITIONS (10 COMPARISONS AT EACH POSITION). THE BLACK (DASHED) LINES INDICATE THE $\pm 2SD$ OF DIFFERENCES AND ARE 1.022, 1.120 AND 0.830 PIXELS FOR X, Y AND Z RESPECTIVELY. THE BLUE (SOLID) LINES REPRESENT THE MEAN DIFFERENCE FOR EVERY PLOT (-0.066,-0.070,-0.050).59

FIGURE 2.10 ABSOLUTE UPTAKE POLAR MAPS SHOWING IMPROVEMENT IN IMAGE UNIFORMITY AFTER MOTION COMPENSATION. A REDUCTION IN UPTAKE IS SEEN IN THE ANTERIOR-LATERAL, POSTERIOR-SEPTAL AND APICAL REGIONS WHERE MOST MOTION-AVERAGING OCCURS. IMAGE UNIFORMITY IMPROVES AFTER MOTION-CORRECTION (SECOND ROW). THE MOTION-FREE IMAGE CORRESPONDS TO THE IMAGE FROM A SINGLE RESPIRATORY PHASE (END-EXPIRATION). IN THIS FIGURE, S=SEPTAL, L=LATERAL, P=POSTERIOR (INFERIOR) WALL OF THE HEART.61

FIGURE 2.11 PERCENTAGE DIFFERENCE POLAR MAPS FOR THE UPTAKE POLAR MAPS SHOWN IN FIGURE 2.10 COMPARED TO THE MOTION-FREE IMAGE.63

FIGURE 2.12 SEGMENTAL MEAN PERCENTAGE ERRORS FOR THE ABSOLUTE UPTAKE MAPS SHOWN IN FIGURE 2.10, RELATIVE TO THE MOTION-FREE IMAGE. THE STANDARD DEVIATION (SD) OF THESE ERRORS SERVE AS A MEASURE OF IMAGE UNIFORMITY.....64

FIGURE 2.13 SELF NORMALIZED UPTAKE POLAR MAPS. THE POLAR MAPS SHOWN IN FIGURE 2.10 WERE SEGMENTED FOLLOWING THE 17 SEGMENT MODEL AND THE AVERAGE OF UPTAKE VALUES IN EACH SEGMENT

WERE USED TO REPRESENT THAT SEGMENT. IMAGES WERE THEN PRESENTED AS A PERCENTAGE OF THE
MAXIMUM SEGMENTAL VALUE IN EACH POLAR MAP.66

FIGURE 2.14 SEGMENTAL MEAN PERCENTAGE ERROR CALCULATION FOR NORMALIZED UPTAKE IMAGES,
RELATIVE TO THE MOTION-FREE POLAR MAP.....67

FIGURE 2.15 ABSOLUTE BLOOD FLOW POLAR MAPS SHOW IMPROVEMENT IN SIMILARITY WITH THE MOTION-
FREE AFTER MOTION COMPENSATION. THE MOTION-FREE MAP IS THE BLOOD-FLOW DISTRIBUTION FOR A
SINGLE RESPIRATORY PHASE TAKEN AT END-INSPIRATION AND SERVES AS OUR MOTION-FREE STANDARD.
ALL POLAR MAPS ARE EXPRESSED IN ABSOLUTE UNITS OF BLOOD FLOW: ML/MIN/G. BLOOD-FLOW
SIMILARITY WITH THE MOTION-FREE IMAGE IMPROVES AFTER MOTION CORRECTION.68

FIGURE 2.16 PERCENT DIFFERENCE MAPS SHOWN FOR THE ABSOLUTE BLOOD FLOW POLAR MAPS SHOWN
ABOVE IN FIGURE 2.15, COMPARED TO THE MOTION-FREE MAP. THE LARGEST ERRORS ARE SEEN IN THE
POSTERIOR REGION.....69

FIGURE 2.17 ABSOLUTE SEGMENTAL MEAN PERCENTAGE ERRORS FOR THE ABSOLUTE BLOOD FLOW MAPS
SHOWN IN FIGURE 2.15 RELATIVE TO THE MOTION-FREE MAP.....69

FIGURE 2.18 DISPLACEMENTS MEASURED FROM GATED PET IMAGES ON X, Y AND Z AXES, USING PHASE #4 AS
THE ZERO POSITION. ERROR BARS ARE TAKEN FROM THE POOLED STANDARD DEVIATION OF RESULTS FROM
THE PHASE-ALIGNMENT ACCURACY TEST (SECTION 2.1.4)).....77

FIGURE 2.19 UPTAKE POLAR MAPS SHOWING THE DISTRIBUTION OF ACTIVITY VALUES IN LATER DYNAMIC
FRAMES. A REDUCTION OF ACTIVITY IS SEEN IN THE APEX WHICH IS CAUSED BY THINNER APICAL THICKNESS
OF THE HEART.78

FIGURE 2.20 PERCENTAGE DIFFERENCE POLAR MAPS FOR THE UPTAKE POLAR MAPS SHOWN IN FIGURE 2.19
COMPARED TO THE MOTION-FREE IMAGE.79

FIGURE 2.21 ABSOLUTE SEGMENTAL MEAN PERCENTAGE ERRORS FOR THE UPTAKE POLAR MAPS SHOWN IN .
FIGURE 2.19 RELATIVE TO THE MOTION-FREE POLAR MAP.80

FIGURE 2.22 UPTAKE POLAR MAPS SHOWN IN FIGURE 2.19 THAT ARE NORMALIZED TO THE SELF-MAXIMUM
SEGMENTAL VALUE.....81

FIGURE 2.23 SEGMENTAL MEAN PERCENTAGE ERROR CALCULATION FOR NORMALIZED UPTAKE IMAGES, RELATIVE TO THE MOTION-FREE POLAR MAP SHOWN IN FIGURE 2.22.....	83
FIGURE 2.24 ABSOLUTE BLOOD-FLOW POLAR MAPS SHOWING IMAGE UNIFORMITY BEFORE AND AFTER MOTION CORRECTION.....	84
FIGURE 2.25 PERCENT DIFFERENCE MAPS FOR THE ABSOLUTE BLOOD FLOW MAPS SHOWN ABOVE IN.....	85
FIGURE 2.26 SEGMENTAL MEAN PERCENTAGE ERRORS FOR THE ABSOLUTE BLOOD FLOW MAPS SHOWN IN FIGURE 4.5 RELATIVE TO THE MOTION-FREE MAP	86
FIGURE 3.1 ORTHOGONAL VIEWS OF THE HEART SHOWING (A) CORONAL, (B) SAGITTAL AND (C) TRANSAXIAL VIEWS FOR PHANTOMS WITH A 50 MM LESION (FIRST ROW) AND 30 MM LESION (SECOND ROW) IN THE LATERAL WALL OF THE LEFT VENTRICLE.....	91
FIGURE 3.2 FIRST ROW: UPTAKE POLAR MAPS SHOWN FOR THE LARGE SIMULATED DEFECT. SECOND ROW: PERCENTAGE DIFFERENCE POLAR MAPS FOR THE POLAR MAPS SHOWN IN THE FIRST ROW COMPARED TO THE MOTION-FREE IMAGE. THIRD ROW: SEGMENTAL MEAN PERCENTAGE ERRORS FOR THE MOTION-CORRECTED AND MOTION BLURRED POLAR MAP COMPARED TO THE MOTION-FREE POLAR MAP IN THE FIRST ROW.	94
FIGURE 3.3 POLAR MAP COMPARISONS, SIMILAR TO FIGURE 3.2, FOR THE SMALL SIMULATED DEFECT. FIRST ROW: UPTAKE POLAR MAPS SHOWN FOR THE SMALL SIMULATED DEFECT. SECOND ROW: PERCENTAGE DIFFERENCE POLAR MAPS FOR THE POLAR MAPS SHOWN IN THE FIRST ROW COMPARED TO THE MOTION-FREE IMAGE. THIRD ROW: SEGMENTAL MEAN PERCENTAGE ERRORS FOR THE MOTION-CORRECTED AND MOTION BLURRED POLAR MAP COMPARED TO THE MOTION-FREE POLAR MAP IN THE FIRST ROW.	95
FIGURE 3.4 POLAR MAP COMPARISONS FOR THE PATIENT STUDY. FIRST ROW: UPTAKE POLAR MAPS. SECOND ROW: PERCENTAGE DIFFERENCE POLAR MAPS FOR THE POLAR MAPS SHOWN IN THE FIRST ROW COMPARED TO THE MOTION-FREE IMAGE. THIRD ROW: ABSOLUTE SEGMENTAL MEAN PERCENTAGE ERRORS FOR THE MOTION-CORRECTED AND MOTION BLURRED POLAR MAP COMPARED TO THE MOTION-FREE POLAR MAP IN THE FIRST ROW.....	96

Chapter 1 Introduction

1.1 Project overview

Positron Emission Tomography (PET) is a non-invasive diagnostic medical imaging modality that produces tomographic images of the distribution of a radionuclide-labeled pharmaceutical in the body. These images can reveal on-going biochemical functions and are called *functional* images accordingly, as opposed to *structural* images that are typically generated by modalities such as computed tomography (CT) and Magnetic Resonance Imaging (MRI). The radionuclide-labeled pharmaceutical, also called a radiotracer (or simply – tracer), is administered to the patient and is taken up in a tissue of interest after following a particular biological process. The isotope then decays, giving rise to energy particles (photons) that are detected by the PET scanner and are subsequently processed to form tomographic images of the tracer distribution. The intensity of the images at any given location, relates directly to the amount of tracer uptake at that particular location in the body. Such information can be used to characterize the underlying function, which is of diagnostic value.

Myocardial perfusion imaging (MPI) refers to the non-invasive measurement of the flow of blood through the heart tissues. This method is the widely used for the diagnosis of ischemic heart disease, and is based on the fact that diseased areas of the heart receive less blood flow than the normal areas. Myocardial blood flow (MBF) can be determined on absolute and relative scales. PET is considered the gold standard for measuring myocardial perfusion in vivo [1]. Determination of absolute MBF is possible

using PET imaging and is defined as the rate of blood supplied to a given volume or mass of tissue in units of mL/min/g.

A number of PET tracers have been used for imaging of the heart, the most common of which are listed in Table 1.1. Many of these tracers are produced in cyclotrons by bombarding specific nuclei with high energy protons. Due to the high cost and complexity of this process and the limited availability of on-site cyclotrons, there has been an interest in using generator produced tracers such as rubidium-82 (^{82}Rb). ^{82}Rb is the product of strontium-82 (^{82}Sr) decay. ^{82}Sr is produced in large cyclotrons that are capable of bombarding metallic Rb or RbCl solutions with high energy photons (~80 MeV) [2]. ^{82}Sr has a half life of 25.5 days and can be used to continuously generate ^{82}Rb activity. The $^{82}\text{Sr}/^{82}\text{Rb}$ generators are used to produce ^{82}Rb . In order to extract the produced ^{82}Rb , the generator consists of a tin-oxide (SnO_2) ion-separation column which strongly binds to Sr isotopes. The ^{82}Rb atoms bind much more weakly to the ion-column than Sr and when the column is flushed with a solution such as 0.9% sodium-chloride (NaCl) saline, Rb takes the place of Na (sodium) and the ^{82}Rb is extracted in the form of RbCl [2].

The Rb cation (Rb^+) is a biological analog of the potassium cation (K^+) and is actively transported across the cell membrane and into the heart tissue where it is naturally retained. The short 76 second half-life of ^{82}Rb allows for rapid repeated studies for MBF. ^{82}Rb is directly infused into the patient in the form of $^{82}\text{RbCl}$ using automated infusion systems [3].

Table 1.1 Commonly-used PET tracers and their uses [4]

Tracer	Half-life (min)	Application	Method of Production
¹⁸ F-FDG	109.8	Metabolism	Cyclotron
¹⁸ C-Acetate	20.4	Metabolism	Cyclotron
¹⁸ NH ₃	9.97	Perfusion	Cyclotron
¹⁵ O-Water	2.03	Perfusion	Cyclotron
⁸² Rb	1.27	Perfusion	Generator

The left ventricle (LV) is the heart's main pumping chamber, circulating oxygenated blood throughout the body via the aorta. Being the heart's thickest muscle tissue, the LV retains a large amount of tracer and is highly visible in ⁸²Rb-PET images. ⁸²Rb-PET is used to diagnose ventricular dysfunction and coronary artery disease (CAD).

As a result of interactions with matter, the photons generated by the decay of the PET radiotracers inside the body become attenuated as they travel from the site of decay to the PET detectors. In order to accurately depict the tracer uptake, one must correct for the loss of signal due to photon attenuation. This is possible by measuring the attenuation properties of the body (attenuation map). With the advent of combined PET/CT scanners, the CT scan can provide the attenuation map as well as accurate anatomical localization of tracer signals in the body.

Typical diagnostic PET scans are obtained over several minutes. At the University of Ottawa Heart Institute (UOHI), ⁸²Rb-PET scans are acquired following a 10 minute scanning protocol. The resulting images represent a time-averaged picture of the distribution of activity in the body. However the CT scan for the same study is acquired rapidly (< 1 second per slice). This discrepancy can cause an issue with the use of CT-based attenuation correction (CTAC), because of the inconsistencies between the attenuation map and the PET data caused by breathing motion. These inconsistencies can introduce errors in the attenuation-corrected images, affecting diagnostic interpretation.

Additionally, respiratory motion of the heart has been shown to degrade image quality by blurring the acquired counts along the path of movement. A reduction in motion blurring is possible through the use of respiratory gating, which bins the acquired signal based on the phase of the respiratory cycle. This technique ultimately generates a separate image for each phase of the respiratory cycle; (respiratory phases). Each respiratory-phase image is noisy because the acquired PET data have been divided into several different phases (typically 4-10) [5]. Realignment of the respiratory-phase images allows summing of the images together to reduce noise while maintaining the improved temporal resolution obtained by respiratory gating.

The objectives of this research were to develop a method for alignment of the respiratory phases to correct for motion blurring and to investigate the combined effect of realignment and respiratory-motion-compensated CT-based attenuation correction. The results of this work are expected to improve image quality of cardiac ^{82}Rb PET imaging, leading to an improvement in diagnostic accuracy of this imaging modality.

1.2 The Physics of PET

1.2.1 Positron Decay

The radioactive tracers used in PET imaging have an over-abundance of protons which prompts their radioactive decay to a more stable nuclear state. Proton-rich nuclei decay via a mixture of two processes, *electron capture* and *positron decay*. The lighter elements that are most commonly used in PET imaging decay primarily via positron decay. The general scheme of positron decay is illustrated below:



where X is the parent atom with atomic mass A and atomic number Z , Y is the daughter atom, β^+ is the positron and ν_e is the electron-neutrino. The kinetic energy of the positron and the neutrino equals the difference between the parent and daughter energies minus 1.02 MeV (two times the resting energy of an electron). The kinetic energy is shared between the positron and neutrino, resulting in a continuum of possible energies for the positron. The mean and maximum positron energies for commonly used positron-emitting isotopes are listed below [6].

Table 1.2 Decay characteristics for commonly-used PET radio-nuclides [6]

Isotope	Half life (min)	Max Range in Water (mm)	Max Energy (MeV)	Mean Energy (MeV)
11C	20.4	4.1	0.96	0.386
13N	9.98	5.4	1.19	0.492
15O	2.03	8.0	1.73	0.735
18F	109.8	2.4	0.63	0.250
82Rb	1.27	16.5	3.36	1.5

Once the positron is released from the nucleus, it will travel through surrounding matter while constantly losing its energy through ionization events with other atoms, or by Bremstrahlung radiation after inelastic scattering. These events cause deflections in the path of the positron, causing it to have an extremely twisted path through matter. Eventually, once the positron has essentially come to rest, it combines with an electron from the surrounding material, producing two 511 keV photons that are emitted in opposite directions. This event is known as *positron annihilation*. The data acquired using in this manner are called *emission data*, referring to the fact that the data originates from a subject that has been injected with a positron-emitting isotope.

1.2.2 Detection of Annihilation Photons

The detection of the annihilation photons forms the basis of PET imaging and is illustrated in Figure 1.1. Most PET scanners use multiple rings of gamma ray detectors that surround the subject. However, some models use partial rings of detector with a rapidly rotating gantry in order to reduce cost. In this thesis, we will assume the more common full detector ring model. Because two photons are created with each annihilation event, PET uses the coincidence detection of these two photons to help reduce background and localize the point of annihilation. The line connecting the two detectors - or more accurately, the volume between two detector elements - is referred to as a “line of response” or LOR. The LOR defines the path taken by the photons through the field of view FOV.

If an annihilation event occurs within the FOV of the scanner, the two detectors connected by the line of response of the annihilation will produce an electrical signal. If the signal amplitudes on both detectors have the correct energy to be a 511keV photon and both are detected within a specified timing window, the event is registered as a coincidence. The timing window is commonly known as the *coincidence timing window* (2τ) and is in the order of several nanoseconds.

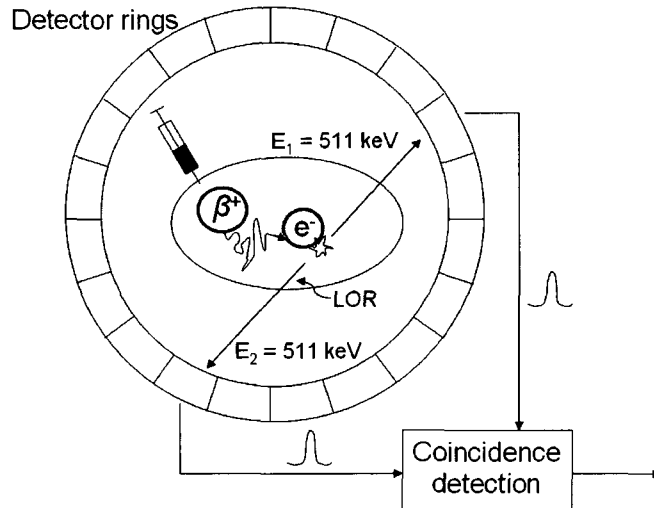


Figure 1.1 A schematic illustration of the data acquisition process in PET imaging. A positron emitting radioactive tracer is injected into the body and follows its biological pathway to be taken up in an organ of interest. The positron travels a twisted path due to the interactions with surrounding matter and finally annihilates with an electron at rest, giving rise to two 511 keV photons which are detected by the scanner via coincidence detection.

Every coincidence detection has a corresponding LOR. The LORs can be completely described by the radial, angular and axial coordinates of the two detectors involved. In histogram-based acquisitions, data from all coincidences are gathered in a histogram, where each entry corresponds to a unique angular and radial (and axial) location in the FOV of the scanner (Figure 1.2). This histogram is also known as a sinogram since a point source at a radius (r) from the center of the FOV of the scanner creates a sinusoidal path in the histogram as a function of the projection angle θ [7]. In dynamic acquisitions, where the distribution of activity over time is of interest, the data are acquired in consecutive time-frames and a separate set of sinograms is acquired for each time frame. Dynamic data acquisition will be described in more detail in section 1.5.2. In order to transform sinograms into images, image reconstruction needs to be performed, which will be described in section 1.4.

An alternative to histogram-based acquisitions is to acquire in “list-mode”, where each event is individually recorded with information about the two detectors at which the

annihilation photons interacted as well as the time of interaction and the energies of the detected photons. List-mode acquisitions allow for reprocessing of the same data in multiple different ways. In dynamic studies, the time of the event is used to sort the data into time-bins upon completion of the study. Sinograms can then be created retrospectively for each time bin.

Physiological signals can also be incorporated into the event list in order to study specific characteristics. For instance, if electro-cardiogram (ECG) signals of the heart are recorded during the PET acquisition and included in the list, list-mode events can be sorted using these signals to ultimately generate ECG-gated images which show an image of the heart for each phase of the cardiac cycle. These images provide important diagnostic and prognostic information to clinicians. The same concept can be used to acquire respiratory-gated images (see section 1.5.3).

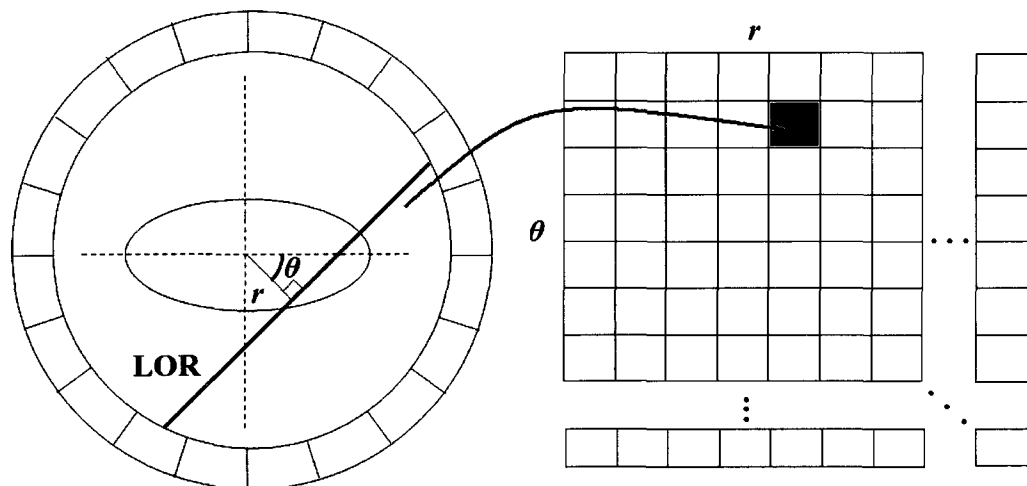


Figure 1.2 A diagram showing the relationship between an LOR and its corresponding element in the sinogram

1.2.3 Classification of Detected Events

Under ideal conditions, all coincidences recorded by the scanner would correspond to annihilation events. However, due to imperfect temporal and energy

resolution, incomplete solid-angle coverage of the detectors, and photon interactions within the patient, measured coincidences are contaminated with undesirable events, that include *scattered*, *multiple* and *random* coincidences (see Figure 1.3).

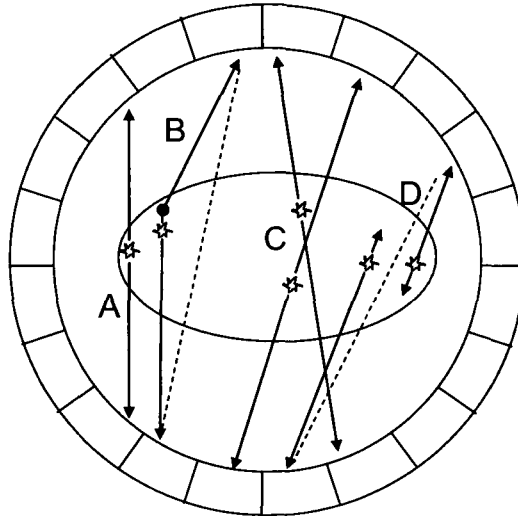


Figure 1.3 Illustration of different coincidence event types in PET imaging. A) true coincidence, b) scattered coincidence, c) Multiple coincidence and d) Random coincidence. The true path is shown by a solid line while the corresponding LOR is shown with a dashed line.

In true coincidences, both annihilation photons escape the body and are detected by a pair of detectors and the LOR is properly measured (Figure 1.3A). In scattered events, at least one of the photons is deflected inside the body due to an interaction with the surrounding matter, most commonly a Compton scattering event. Consequently, it will deviate from its initial path and the event will be assigned to an incorrect LOR (Figure 1.3B). At high count-rates, it is possible that annihilation events will occur in rapid succession and lead to three or more detectors registering a photon signal within a single timing window. In this case, the orientation of the LOR becomes ambiguous (Figure 1.3C), and therefore these *multiple* coincidences are usually discarded. In *Random* coincidences, photons corresponding to unrelated annihilation events are detected within a single coincidence timing window (Figure 1.3D). These coincidences

can produce an undesired background in the final images. Correction methods for these coincidences are described in section 1.3.3.

An additional point to consider is that the majority of photons detected by the PET scanner are *single* events, in which only one of the two annihilation photons is detected. The partner photon may not have enough energy upon striking the detector to be registered or may not reach the detector at all. These events are discarded by the scanner, but contribute to multiple and random coincidences. Single events also contribute to pulse pileup in detector electronics that prevents processing of events for short periods of time. This effect is called *detector dead-time* and correction for this form of signal loss will also be described briefly in section 1.3.1.

A special type of singles event that occurs in Rb-82-PET is a prompt. This is a high-energy gamma-ray (776keV) that is frequently emitted (~10%) at the same time as the annihilation event. This photon can scatter and be detected in coincidence with a true annihilation photon creating an addition scatter-type event.

1.2.4 2D vs 3D Data Acquisition

PET data can be acquired in 2D or 3D modes. As briefly mentioned above, the detector blocks in most PET scanners are housed in multiple rings around the patient. When acquiring in 2D mode, only the coincidences occurring between detector elements within the same detector ring, or between detectors in two adjacent detector rings are used. In order to obstruct annihilation photons incident at larger angles, thin shield usually made from tungsten or lead and referred to as *septa* are inserted between detector rings. This helps keep scatter and random coincidence event rates low, and reduces the single-photon flux from outside the field of view. However, sensitivity of the camera is

also limited since the overall count rates on the detectors are reduced. This acquisition mode is commonly referred to as 2D mode since the data collection is restricted to a set of almost parallel 2D planes.

The data acquired in 2D mode are sufficient for reconstructing the entire image volume [8, 9]. However, in order to increase image sensitivity and improve the signal-to-noise ratio of the reconstructed data, additional coincidence plane combinations can be included in the process. This requires the retracting the septa that would otherwise block these oblique lines of responses. This acquisition mode is commonly referred to as 3D since the coincidence planes are no longer only limited to parallel planes. The 3D mode typically improves sensitivity by a factor of 5 to 7 compared to the 2D acquisition [10, 11] and can also be used to reduce imaging time or the amount of radioactivity that is injected. However, the lack of septa results in a three- to fourfold increase in the fraction of scattered events detected [7]. Randoms rates also increase and so the subtraction of random coincidences leads to an elevated level of noise at lower activity concentrations than in 2D because each detector sees more of the radioactivity in the body and has a higher singles rate. The increase in randoms and scatter events leads to challenges in accurately correcting for these events. Recent studies have shown that the 3D acquisition mode is feasible for use in quantitative cardiac imaging [4, 12]. At the UOHI, ^{82}Rb imaging is routinely done in 3D mode as accurate scatter and randoms corrections exist and provide for accurate quantitative measurements of MBF.

1.3 Data correction

In order to produce an accurate image, where each pixel represents the true distribution of activity in the tissue, a number of physical corrections need to be applied to the sinogram data. The most common corrections are briefly discussed here.

1.3.1 Dead-time Correction

Dead time is an effect that arises when a photon strikes a detector while an event is already being processed by the system. Due to this effect, PET detectors are unable to accurately process incoming events for short periods of time. The main source of dead time in most PET systems is the processing of each event in the detector front-end electronics. Other contributions to dead time come from coincidence event processing, real-time sorting of data into sinograms and data transfer. This effect reduces the detectable count-rate of the scanner and produces a non-linear relationship between count rate and activity in the field of view of the scanner. Two models are commonly used to describe dead-time losses. In the *paralysable model*, if a second event is detected before the first event is finished processing, both are discarded. This results in observed count rates dropping to zero as true count rate increases. In the *non-paralysable model*, the second event is ignored and processing of the first event continues. Therefore, observed count rates plateau at a constant level for these systems. Scaling factors can be calculated using these models to correct the acquired counts for deadtime losses [13-15].

1.3.2 Normalization

In order to account for the variation in detector efficiencies and variable spacing between detector pairs, acquired counts are corrected by a multiplicative correction factor that is specific to each LOR. The correction factors can be acquired by placing a uniform

source of activity in the FOV [7]. The acquired counts will be corrected to provide an equal amount of activity for all angles, and the correction factors are thus retrieved. The source is chosen to be of relatively low activity to avoid dead-time effects. However, in order to provide a good estimate of the efficiencies, an adequate number of counts per LOR should be acquired to minimize the statistical noise [16]. Thus the acquisition of normalization factors (normalization scans) require lengthy scan times, typically 12hrs or more. Some common source are a cylindrical phantom that is placed at the center of the scanner or a rotating rod source that uniformly rotates close to the detector surfaces outside of the imaging FOV. Long-lived isotopes such as germanium-68 (^{68}Ge , $t_{1/2} = 271$ days) are suitable for this purpose.

This degree of normalization is sufficient for relative PET where the images are interpreted visually without reference to the absolute values in each volume element of the image (voxel). However for many PET studies, it is desirable to be able to relate the number of counts recorded in a voxel to the amount of tracer activity (MBq) in a voxel. This is needed for kinetic analysis of myocardial perfusion images. For example, to relate image values to an arterial input function that was obtained with blood sampling, the radioactivity is measured in a radiation detector, such as a well counter. This provides the means to measure blood flow in units of MBq/min/g. Therefore an accurate calibration between the PET scanner and the well counter is needed which can be calculated by scanning a known uniform activity concentration (measured in the well counter) [13]. Blood flow measurements are discussed in more detail in section 1.7.

1.3.3 Correction for Random Coincidences

Random coincidences ultimately add an undesirable uniform background to the images. Two main methods can be used to correct for random coincidences. In the first method, the randoms rate is calculated from the rate of singles detection. The rate of random coincidences (randoms per second, N_R) in a pair of detectors is given by the equation below:

$$N_R = 2\tau N_1 N_2 \quad (3.3.1)$$

where 2τ is the coincidence timing window, and N_1 and N_2 are the single photon detection rates in the paired detectors. Ultimately, N_R is subtracted from the total number of coincidences that are recorded for that LOR. In the second method, a parallel coincidence detection circuit is added to the main coincidence detection circuit. The logic pulse from one of the two detectors is delayed in time in comparison to the other circuit, such that the detector pair cannot produce any true coincidences. Consequently, any coincidences seen in this circuit will be caused by random coincidences, which can then be subtracted from the total coincidences recorded for corresponding LORs in the main circuit [7]. Random coincidences approximately consist of 70% of total coincidences in routine studies.

1.3.4 Scatter Correction

After the random coincidences are removed by methods described above, the remaining events are *true* and *scattered* coincidences. Scattered coincidences contaminate the data by increasing background counts that can lead to decreased contrast in the measured signal. As shown in Figure 1.3, scattered photons often undergo substantial interactions in the body prior to detection. These photons, that initially have 511 keV of

energy, interact with the soft tissue and bone found in the body, primarily through *Compton scattering* [17]. In Compton scattering, a photon collides with an electron, and transfers a portion of its energy to the electron, liberating it from its host atom. The trajectory of the in-coming photon changes by angle α , and its exiting energy (E') can be calculated by the equation below:

$$E' = \frac{E}{1 + \frac{E}{E_e}(1 - \cos\alpha)} \quad (3.3.2)$$

Where E is the initial photon energy and E_e is the resting mass of the electron expressed as an energy. As a result, scattered photons have reduced energy, and can be identified by the detectors during data acquisition.

In most PET scanners, *Scintillation detectors* are used to detect gamma rays. In these detectors, a dense crystalline material, (a *scintillator*), is used to absorb the incident gamma rays and convert it into visible light. The intensity of the emitted light is proportional to the energy absorbed in the scintillator. This light is then detected by visible light photon detectors and ultimately converted into electrical currents.

Because the amount of light emitted is proportional to the energy of the incident photon, scintillation detectors can also measure the incident photon energy. As scattered photons have lower energy, they can thus be distinguished from unscattered photons and rejected by the camera. This is commonly known as *energy discrimination*. Unfortunately, scintillators have limited energy resolution, thus all of the scattered events cannot be removed by energy discrimination.

Typical energy resolutions range from 9% (germanium oxyorthosilicate or GSO scintillation crystals) to 18% (bismuth germinate or BGO) for 511keV photons [18] and are usually measured by scanning a line source in air (such as ^{68}Ge) and calculating the

full width at half maximum of the detected signal. The energy resolution of the Discovery DRx PET/CT scanner (GE Healthcare) currently used at the UOHI is 14% (using lutetium yttrium orthosilicate or LYSO crystals) and uses an energy window of 425-650 keV for energy discrimination [19].

Even with energy discrimination, a large number of scattered photons are still detected by the PET scanner. The fraction of scattered coincidences to the total recorded coincidences is commonly known as the *Scatter Fraction* (SF) and can range from 15% to well over 50% in typical PET studies depending on the size of the object and the geometry and energy resolution of the scanner. The scatter fraction for the scanner used at the UOHI is 32.1% (3D acquisitions) [19]. To correct for scatter, it is first necessary to estimate the scatter distribution of scattered photons detected the camera and several different methods have been developed for doing this as is discussed below. After the scattered distribution is calculated, it can be subtracted from the recorded data to produce a scatter-corrected sinogram. In iterative reconstruction algorithms, an alternative approach to scatter correction is to incorporate it as a step in the iteration.

Over the past years, scatter correction has been discussed in much detail and a variety of algorithms have been proposed to address this problem [20-23]. Methods of estimating the scatter distribution consist of mathematical models to calculate it as well as analytical approaches which estimated it from projection or image data [24-26]. One of the more accurate methods is the calculation approach outlined by Watson *et al.* [27]. They begin with 2D emission and transmission scans. An estimate of the probability of detecting photons scattered from any point within the emission image was then derived, using the Klein-Nishina probability function [17], from the attenuation coefficients map,

photon energies before and after scattering, and the scattering angle. The distribution of photons that underwent a single scatter was then estimated for points in projection space by integrating the probability of detecting scattered photons from each image point, scaled by the activity at each point as given by the emission image. The integration is performed over the entire scattering medium volume. The calculated scatter distribution was then subtracted from the emission image. Although the scatter calculated using this model is fairly accurate, it does not account for the scatter that comes from sources outside of the FOV of the scanner [20, 27].

Analytical functions are also used to do scatter correction. One common method is the convolution-subtraction algorithm. In a method by Bailey *et al.* [28], photopeak projections were convolved with an exponential function, assuming an existing relationship between scatter and photopeak data, to estimate the scatter distribution prior to subtraction. Convolution based algorithms are faster than model based algorithms and are often sufficiently accurate. At the UOHI, a model based scatter correction method is used [29] for 3D imaging whereas convolution-subtraction is used for 2D acquisitions.

1.3.5 Attenuation Correction

If annihilation photons interact with matter prior to exiting the body, they are attenuated from their original path, resulting in a loss in the total number of photons detected. These interactions are primarily through the process of Compton scattering, which was introduced in section 1.3.4, though other processes such as photoelectric absorption may contribute. As a result, the probability of exiting the body and detection decreases exponentially as a function of the distance traveled through the body. This probability is given by the equation below, for every photon:

$$I(x) = I_0 e^{-\int \mu(E,x) dx} \quad (3.3.3)$$

where I_0 and I are the original and exiting photon fluxes, respectively. The linear attenuation coefficient (μ) is in units of cm^{-1} and is a function of photon energy and atomic number of the attenuating medium. The argument of the exponential is integrated over the photon path length and, therefore, the photons that originate deeper inside the subject, travel through a greater amount of tissue before exiting and are typically more attenuated. For instance, if the length that photons must travel through the body is 20cm only 15% of them will escape the body without scattering or total absorption, assuming uniform attenuation equal to that of water. For a path length of 40cm (as in heavier patients), this fraction reduces to 2%. This can cause an underestimation in the activity measured in organs that reside deeper inside the body. In other words, regions near the edge of the body would appear more intense in images.

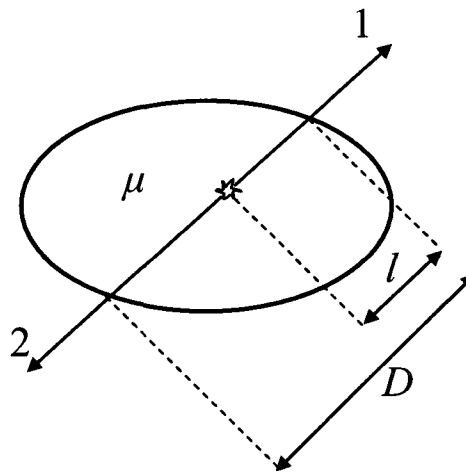


Figure 1.4 Schematic illustration of an annihilation event occurring in depth x in a medium with an attenuation coefficient of μ

In the case of homogeneous material, if one considers the LOR along which the annihilation has occurred, the exiting photon fluxes of the first and second annihilation photons are given by:

$$I_1(x) = I_0 e^{-\mu l}, \quad I_2(x) = I_0 e^{-\mu(D-l)} \quad (3.3.4)$$

where D is the thickness of the subject along the LOR; as shown in Figure 1.4.

The probability that annihilation photon 1 will exit the subject is shown below:

$$p_1 = \frac{I_1(x)}{I_0} = e^{-\mu l} \quad (3.3.5)$$

The probability that annihilation photon 2 will exit is:

$$p_2 = \frac{I_2(x)}{I_0} = e^{-\mu(D-l)} \quad (3.3.6)$$

Consequently, the probability that both annihilation photons will exit the subject is the product of the individual probabilities:

$$P_{12} = e^{-\mu l} \times e^{-\mu(D-l)} = e^{-\mu D} \quad (3.3.7)$$

As can be seen from the equation above, the reduction in detection probability is independent of the location of the annihilation event along the LOR and dependant only on the thickness of the subject and the attenuation coefficient along the desired LOR. This property is unique to PET imaging, and provides for highly accurate attenuation correction.

In order to correct for the attenuation occurred, an attenuation correction factor (ACF) needs to be applied to the emission data and is given by the reciprocal of equation (3.3.7):

$$ACF = e^{\mu D} = \frac{I_0}{I(D)} \quad (3.3.8)$$

The ACF is specific to each LOR and so this process is repeated for all LORs in the FOV of the scanner.

Attenuation correction can be applied assuming a simple geometrical shape with a constant attenuation coefficient. In order to simulate the density and geometry of the human body, physical and digital models are frequently used for scanner quality assurance and are commonly known as *phantoms*. When using a physical phantom, an estimation of the attenuation coefficients in the body is possible, where the shape of the phantom is known, and the attenuation coefficient is typically uniform. This method is very prone to artifacts in more complex imaging subjects, due to the approximations made [7].

In a more accurate method, attenuation correction factors are determined through direct measurements. As shown in equation (3.3.7), the amount of photon attenuation is independent of the location of photon origination, therefore, the amount of attenuation would be the same if photons were produced outside of the subject. By rotating positron emitting isotopes such as ^{68}Ge around the outside of the patient, the attenuation caused by the transmission of 511 keV photons through the body can be measured; this measurement is named a *transmission scan*. A reference or *blank scan* is acquired without the subject inside the scanner to measure I_0 from equation (3.3.8). Then the transmission scan is done for all LORs connecting detectors i and j , with the subject inside the scanner to provide $I(D_{i,j})$. The ACFs are given by the ratio between the blank sinograms and the transmission sinograms. Gamma emitting sources such as ^{137}Cs (single 662 keV photon emitter) are also used [30], however the ACFs using these sources need to be scaled to the equivalent 511 keV values [31] due to the dependence of μ on E .

The advantage of measuring attenuation directly is that it avoids approximation regarding the geometry and attenuation coefficients of the subject. The drawback is that sufficient time must be allowed so that an adequate number of counts are acquired along each LOR in order to obtain accurate ACFs. This requirement elongates the total scan time, and may not be well tolerated in all patients. In cardiac imaging, transmission acquisitions may take 3 – 10 minutes, depending on scanner design [32]. Patient movement is more likely to occur during this time, and can introduce errors in the measured attenuation maps. Since transmission images acquired by this method are often of low quality, they are often smoothed or segmented before being applied to the emission data to prevent noise propagation in the emission data.

More recently, combined PET/CT scanners have been developed which allow the use of high quality CT images for calculating the ACFs. In these systems, the PET scanner is integrated with a modern multi-slice CT scanner. As a result, the patient can receive both the CT and the PET scans while lying on the same scanner bed. In CT scans, polyenergetic X-ray beams are transmitted through the body as the X-ray source is rotated inside the gantry. The CT values obtained are then scaled to the appropriate 511 keV values to be used for the correction method [33]. A brief introduction to CT image acquisition follows in section 1.8.

The main advantage of CT-based transmission imaging is the high quality of the acquired transmission maps leading to potentially more accurate correction, and the speed of the acquisition which results in reduced imaging times and greater patient comfort. However, CT-based transmission scans are acquired rapidly, taking less than a second for each slice and therefore represent a snapshot of the body while the PET emission scans

take several minutes and represent a temporal-averaged image. This fact leads to a relatively high frequency of misregistration errors between the attenuation and emission image [34] and will be discussed in more detail in section 1.8.

1.4 Image Reconstruction

Image reconstruction is an inverse problem. A PET scanner acquires data from the detected annihilation photons, but we would like an image of the distribution of tracer within the patient. Reconstruction is necessary because the raw data only restrict the annihilation event to be along the LOR and do not specify the exact spatial coordinates in the subject. Image reconstruction produces 3D tomographic images of the subject.

Reconstruction can be performed using analytic methods, such as filtered backprojection (FBP) [35, 36], in which a linear superposition of backprojections shapes the reconstructed image. Firstly, an image matrix is defined and for valid lines of responses (such as those shown in Figure 1.2), a line is drawn between the detectors and through the image matrix. The number of counts detected by the detector pair connecting the LOR in question, is added to each pixel that is intersected by the line. Consequently, the counts from each detector pair are being projected back along the line from which they originated. This process is repeated for all valid detector pairs in the system and the counts from each subsequent detector pair is added to the counts backprojected from preceding detector pairs, hence generating a superposition of backprojections.

Simple backprojection results in an image that is an estimation of the true distribution of radioactivity in the object. The reconstructed image pixels are a blurred representation of the object since counts are distributed equally along the line from which they originated. This blurring is proportional to $1 / r$ where r is the distance from the

source of activity. Mathematically, it can be shown that the backprojected image $I_1(x,y)$ and the true activity distribution $I(x,y)$ are related by a convolution with $1/r$:

$$I_1(x, y) = I(x, y) \otimes \frac{1}{r} \quad (3.4.1)$$

where \otimes represents the operation of convolution.

In order to eliminate the $1/r$ blurring factor, deconvolution of the image is needed. One common method is to simplify the deconvolution by filtering (multiplying) the image with a ramp filter $R(f)=f$ in the Fourier domain. The effect of the ramp filter is to amplify high spatial frequencies and thus a low-pass filter may also be applied at this stage to reduce the amplification of noise in the high-frequency regions of the image. Subsequently, the inverse Fourier Transform is applied and the result is backprojected through the FOV. After this process is repeated for all angles (rows) in the sinogram, the image is generated. Since FBP is an exact analytical solution to the inverse problem of image reconstruction, only a single backprojection step is needed which requires little computation power. FBP is the method typically used to reconstruct CT images and has frequently been used in PET imaging due to its short computation times. However, FBP is not favored in low count-density images, or when wide variations in activity concentration is involved, and is prone to image artifacts [34].

An alternative to FBP is to use iterative reconstruction techniques, in which an initial image estimate is made; usually blank or uniform. A forward projection is then taken and compared to the measured projection by taking a difference, for example. Adjustments are then made to the estimated image and the process is repeated until the difference in the estimated and measured projections is minimal. Although iterative reconstruction algorithms are more computationally intensive, they are generally

preferred over FBP since models of system geometry and counting statistics may be introduced into the reconstruction algorithm to improve accuracy.

The most common iterative technique is known as maximum-likelihood expectation maximization (MLEM) [37]. Likelihood is a statistical quantity that is maximized when the difference between the measured and estimated projection data is minimized, and the expectation maximization algorithm iteratively maximizes this likelihood under a Poisson data model [7]. The algorithm accounts for the statistical noise by assuming a Poisson distribution for the projection data determined by the counting statistics in each projection bin, which increases its performance for low-count sinogram data. A system model is derived from the geometry and detection response function of the scanner, which provides the probability of a gamma ray being detected within a specific LOR. This model can be derived from simulations of point sources placed inside the scanner. The algorithm then uses this system model to find a match between the measured and estimated projections. Since there are multiple projection and backprojection steps, the algorithm is more local in nature compared to FBP and is less prone to certain image artifacts, such as streaking and activity spillover (discussed in section 1.7). However, image noise is amplified with increasing number of iterations, thus stopping criteria, regularization methods or post-reconstruction filtering or a combination of the three is implemented is used to prevent excessive noise in the final image.

To accelerate the convergence of image estimates in the MLEM algorithm, a modified version of MLEM was introduced [38]. This is known as ordered-subsets expectation maximization (OSEM). This algorithm proceeds in a similar manner to

MLEM, but in this case only a fraction of the angular data must be processed before updating the image estimate for each iteration. OSEM accelerates image convergence by a factor roughly equal to the number of subsets used.

From the point of view of cardiac PET, FBP often performs well for cardiac PET since myocardial count density is sufficiently high in most study protocols. Also, FBP is usually preferred for dynamic PET imaging using kinetic modeling to estimate absolute perfusion values, because of its exact nature, even though image quality is often poorer than with OSEM. OSEM may be a better choice in situations in which extra-cardiac activity is present or in which count density is low [34].

1.5 Modes of Acquisitions

1.5.1 Static Acquisitions

Emission data can be acquired using different protocols in order to capture different information from the PET study. A *Static acquisition* is the most basic protocol where all of the data collected during the PET scan is used to reconstruct a single image. The static PET thus represents the average tissue activity concentration during the length of the scan. This acquisition mode is used mostly in studies where the tissue activity distribution remains relatively static during data collection, or only a static image of the activity distribution is required.

1.5.2 Dynamic Acquisitions

In some studies however, the dynamic change of the tracer activity distribution in a specific organ is of interest, and can provide valuable information regarding the function of that organ. In *dynamic acquisitions*, we are interested in how that tracer

enters, is retained, and then clears from different organs over the course of the PET acquisition. To acquire this information, the data are collected in a series of separate time frames, which start at the time of injection and continue over a fixed period of time. For instance, at the UOHI, dynamic data for cardiac imaging are acquired with the following protocol for ^{82}Rb , consisting of N time frames $\times M$ seconds (frame length): $9 \times 10\text{s}$, $3 \times 30\text{s}$, $1 \times 60\text{s}$, $1 \times 120\text{s}$, $1 \times 240\text{s}$ for a total of 10 min, 15 frames. This time series is designed to capture the rapidly changing tracer distribution immediately following injection but provide higher statistics (longer integration times) in those later frames where the distribution is changing more slowly and the count rates are lower due to radioactive decay.

As time passes, tracer radioactivity leaves the blood to accumulate within the myocardium. Being the heart's thickest muscle tissue, the LV retains a large amount of tracer and is highly visible in the later dynamic frames. These dynamic frames are used to measure the tracer uptake into the tissue which can give a qualitative measure of MBF. An image of the tracer uptake in the myocardium is formed from the mean of the last few time frames, which are commonly known as *uptake frames*. Absolute blood and myocardial activity concentrations can then be obtained via image-based methods that involve tracking the tracer within the LV. Measurements of activity over time are usually shown in time-activity curves (TAC) (Figure 1.5).

TACs are used to enable the assessment of tracer kinetics for the quantification of parameters such as MBF. The basics of kinetic modeling of radiotracer distribution will be discussed in section 1.7

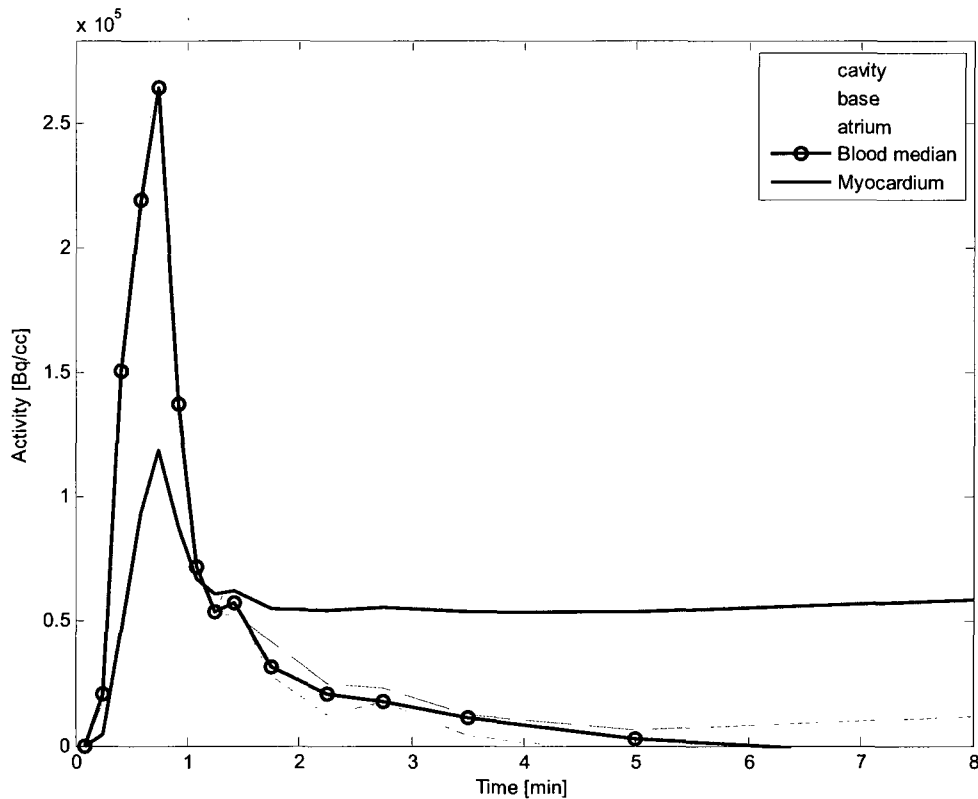


Figure 1.5 Time-activity curves for arterial blood and different sections of the heart are shown. “Cavity” refers to the activity of the blood inside the left ventricle (LV) of the heart, “base” refers to the basal section of the LV, the median activity of the left ventricular blood is also shown. “Myocardium” refers to the muscle tissue of the LV.

1.5.3 Gated Acquisitions

Gated imaging refers to the process of sampling different phases of repetitive physiological cycles during the course of imaging such as the cardiac or respiratory cycles. In the absence of gating, the data are unavoidably averaged over many cardiac and respiratory cycles as a result of lengthy PET acquisitions which are usually on the order of several minutes in duration. During gated PET acquisitions, external devices are used to send a trigger signal to the scanner every time a certain phase of the motion cycle has been reached. The trigger signal is included in the list-mode data, and the acquired data are retrospectively sorted into separate time bins with respect to this signal.

Alternatively, the trigger signal can be used directly to sort the data ‘on-the-fly’ into separate sinograms. The final gated data set represents a series of images that each correspond to a phase in the repetitive motion cycle.

In cardiac-gated PET protocols, electro-cardiogram (ECG) signals of the heart are used as the trigger signal. The resultant images allow for volumetric measurements of the left ventricle at different points in the cardiac cycle [39]. These measurements enable for calculation of the *ejection fraction* (EF) which reflects the ability of the LV to pump blood and is an important prognostic indicator of heart disease. Systolic wall thickening and wall motion can also be determined [40].

The downside to this or any gating approach is that the total number of counts is divided by the number of bins, resulting in reduced count statistics for each gated image. In order to compensate for this fact, image acquisition times are longer for gated images, which come at the expense of increased patient discomfort and reduced scanner throughput. The use of improved scintillation detectors and three-dimensional image acquisition help overcome these limitations [7].

Respiratory-gating provides images of each phase of the respiratory cycle and reduces the amount of motion-blurring due to respiratory-induced motion. This technique has been investigated to reduce breathing motion artifacts in lung cancer imaging [41, 42] as well as in cardiac imaging [43-45] and will be discussed in more detail in section 1.9. The trigger signal used for respiratory-gated PET images, often comes from an external marker such as a chest marker that uses chest wall elevation during respiration as a measure of determining the phase of the breathing cycle.

At the UOHI, the Varian® Real-time Position Management system is used which is a video-based system. A reflector block is placed on the patient's chest and the supplied infra-red camera tracks chest wall motion. The system has the ability to send trigger signals based on the phase of the breathing cycle, as well as signals based on absolute amplitude of chest wall movement. Other methods have been used in the past to obtain a reference for respiratory motion. In some systems, a spirometer is used in which the pressure of an air bag is monitored or pneumotachography is used [46-48]. However, these systems are not widespread due to the discomfort caused by forced spirometry. In other systems, strain gauges with abdominal elasticized belts, temperature sensors detecting the temperature of air flowing into the lungs and laser displacement sensors have also been used [47, 49].

As opposed to the methods mentioned above which rely on external sensors, data-driven techniques have been explored to derive the respiratory state [50-52]. These methods solely rely on measured PET emission data rather than using additional equipment that measure external motion, which may not correlate well with internal organ motion. Also, in gated acquisitions, a certain amount of motion remains in the gated frames which depends on the speed of the motion and the temporal size of each gate. This averaging of motion can be reduced when using data-driven methods.

These methods operate on the fact that the integration of counts in the region containing a moving target, varies linearly with the displacement of the edge of that moving target. In these methods, the Fourier spectrum of the sinogram data is analyzed. Pixels of the sinogram data that are subject to periodic motion during the length of the scan will exhibit a peak in the frequency spectrum at the dominant frequency of the

periodic motion. This frequency is used to extract the respiratory signal from the list-mode data. Binning of the original list mode data is then done according to the estimated respiratory signal.

1.6 Heart Anatomy

The focus of this thesis is the application of PET imaging to the heart. The heart can be broken up into four chambers that work as two separate pumping systems (Figure 1.6). Deoxygenated blood flowing back from the body's organs empties into the right atrium and is then pumped into the right ventricle after passing through the tricuspid valve. The right ventricle pumps this deoxygenated blood to the lungs where it is reoxygenated. Oxygenated blood, returning from the lungs is emptied into the left atrium where it is further pumped into the left ventricle after passing through the mitral valve. The left ventricle has the thickest muscle because it is this portion of the heart that pumps the oxygenated blood via the aorta and circulates it through the rest of the body.

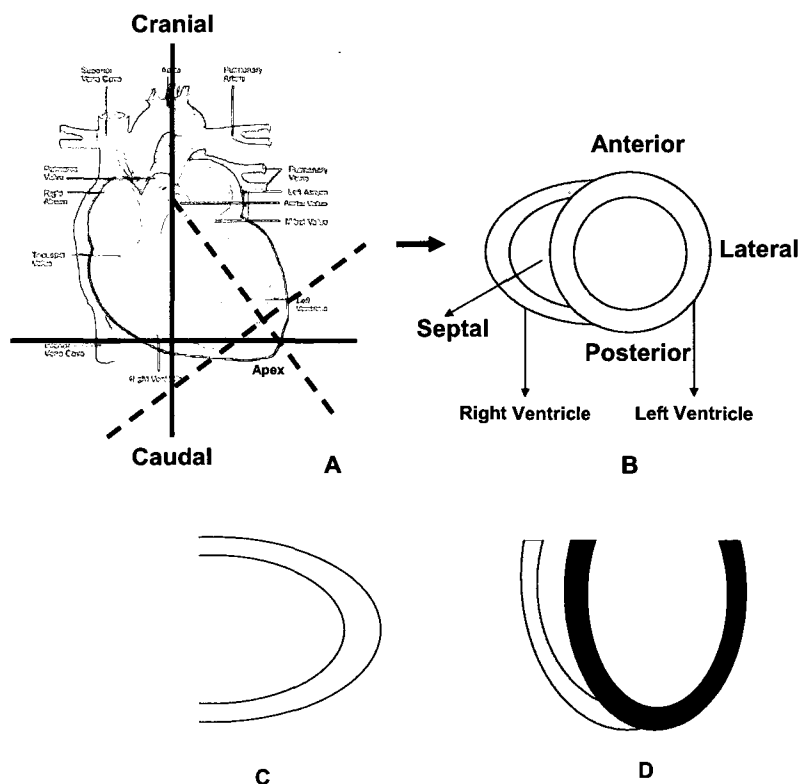


Figure 1.6 A: Schematic representation of the heart. The dashed lines represent the axes of the heart while the solid lines relate to the body axes. B: A cross sectional schematic of the left and right ventricles, commonly known as the “short axis view”. C: Vertical long axis view. D: Horizontal long axis view. Heart image was taken from <http://www.niaaa.nih.gov/>

As shown in the figure, the heart is situated at an angle with respect to the body’s axis. Consequently, transaxial slices (perpendicular to the long axis of the body) do not depict the ventricular cavities clearly. Therefore, the images are usually reoriented in such a way that the heart axes (shown with dashed lines in the figure) become orthogonal to the display (Figure 1.6 - B). These planes through the heart are referred to as the short axis, horizontal long axis, and vertical long axis views (Figure 1.6).

1.7 Tracer Kinetics

As introduced in section 1.5.2, dynamic PET acquisitions allow for the measurement of activity distributions over time. In order to retrieve parameters of

interest, such as myocardial blood flow (MBF), the physiobiological processes of tracer uptake and clearance from the tissue must be modeled mathematically by *kinetic models*. In kinetic modeling, the biochemical states and locations of the tracers of interest are each represented by a *compartment*. For instance, the tracer that is trapped in the myocardium is represented by one compartment (the myocardium) in the one-compartment model, as shown in Figure 1.7.

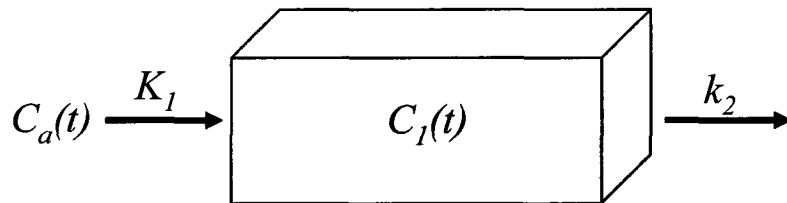


Figure 1.7 The one-compartment model used for Rb PET blood flow analysis. $C_I(t)$ and $C_a(t)$ denote the myocardial tissue and arterial blood radioactivity concentrations respectively. K_1 and K_2 represent the influx and efflux, into and out of the myocardial tissue [7].

The speed at which the radiolabeled tracer is transported across the cell membrane is characterized by rate constant K_1 (mL/min). Once the tracer is taken up inside the myocardial tissue, the radiolabelled molecules may be bound to cell-surfaces or trapped within the cells by different mechanisms. The binding or retention of the tracer may not be permanent, and the rate at which the tracer leaves the tissue to return to circulation is described with rate constant k_2 . $C_a(t)$ represents the concentration of tracer in the blood (MBq/mL). It is referred to as the arterial input function and is given by the blood TAC (see Figure 1.5). $C_I(t)$ is the tracer concentration in the myocardium (MBq/mL). The rate, J , at which radioactivity leaves the blood to accumulate within a given mass of tissue depends linearly on the concentration of the radiotracer in the arterial blood supply (C_a). The constant of this proportionality is in fact K_1 :

$$J = K_1 C_a \quad (3.11.1)$$

Additionally, J can be shown to be equal to the difference between the arterial flux into the tissue and the venous flux out of the tissue (C_V):

$$J = F.C_a - F.C_V = F.(C_a - C_V) \quad (3.11.2)$$

where F is the blood flow in units of mL/min/g of heart tissue. Equations (3.11.1) and (3.11.2) may be combined to give the J as the product of flow:

$$J = K_1.C_a = F.\frac{C_a - C_V}{C_a}.C_a = F.E.C_a \quad (3.11.3)$$

where E is defined as the fraction of tracer that moves from the capillaries to the extravascular space in the tissue of interest on a single pass through local blood vessels, and is commonly known as *extraction fraction*.

The differential equation used to describe the rate of tracer exchange in the one-compartment model is shown below (3.13.1), along with the solution (3.13.2):

$$\frac{dC_1(t)}{dt} = K_1C_a(t) - k_2C_1(t) \quad (3.13.1)$$

$$C_1(t) = e^{-k_2t} \otimes K_1C_a(t) \quad (3.13.2)$$

The one-dimensional convolution operator is represented by \otimes [34].

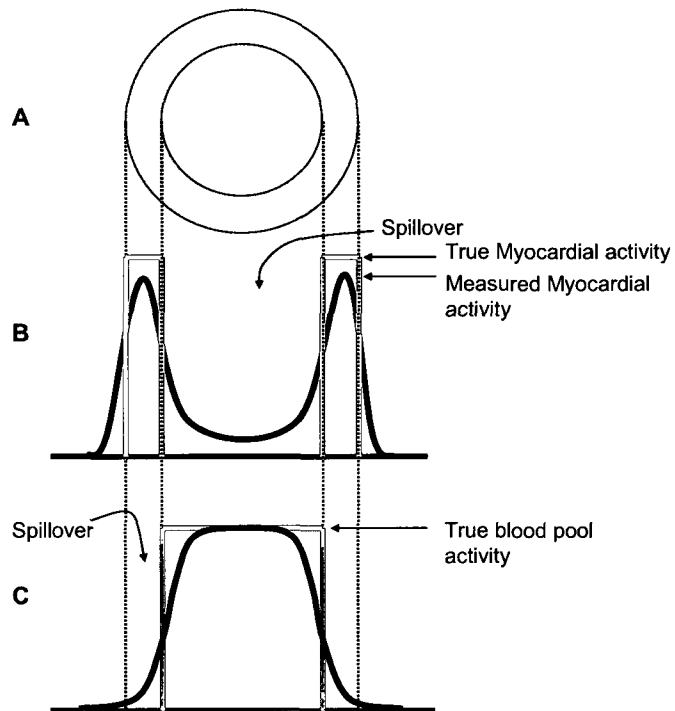


Figure 1.8 A diagrammatic representation of the spillover of measured activity from the myocardium to the blood and vice versa. (A) Shows schematically a short axis cut through the LV myocardium (B) Depicts an activity profile of the cross section shown in (A). (C) Shows an activity profile from the same cross section when the blood activity is high and the myocardial tracer uptake is low.

Blood pool activity measured in a tissue voxel pool is known as spillover from the blood to the tissue (Figure 1.8B). This is also known as total blood volume (TBV) and is given by the fraction of blood in the sampled voxel, ranging from 0 to 1 [53]. The compartment model equation that includes TBV is as follows:

$$C_{measured}(t) = (1 - TBV)C_1(t) + TBVC_a(t) \quad (3.13.3)$$

which describes that the measured signal $C_{measured}(t)$ consists of the tracer concentration in the myocardium $C_1(t)$ with spillover losses $(1 - TBV)$ combined with blood activity spillover into the tissue $TBVC_a(t)$.

At the UOHI, processing of PET images is done using an in-house developed package called FlowQuant© [54], leading to measurement of the variables mentioned above. Using this software, the LV is located using an automated graphical user interface

(GUI), based on the high contrast between the LV and surrounding tissue. Firstly, the LV is located in the FOV by fitting partial ellipses to the LV in 3 orthogonal planes. The coordinates of the partial ellipses help fit the LV to an ellipsoid. Secondly, the ellipsoid is reoriented from the original reference into short axis sections that are taken perpendicular to the long axis of the LV, starting from the apex and continuing to the base of the LV. Finally, the activity distribution of the myocardium is identified by fitting to a mathematical model (13 point deformable spline model). Each of the processing steps are optimized by minimizing a cost function:

$$C = \sum_{p \in image} \frac{I_{max} - I_p}{I_{max}} \quad (3.13.4)$$

where I_{max} is the maximum pixel intensity in the image and $0 \leq I_p \leq I_{max}$ for all pixels in the image. Therefore, the cost of each pixel is in the range (0-1); the high intensity pixels overlapping with the spline model have a low cost and low intensity pixels overlapping with the model are penalized with a high cost [54]. A 3-Dimensional representation of the LV shape is then constructed by sampling activity values in a combined conical and planar coordinate system. If need be, user intervention is allowed at each step of the fit.

Myocardial activity in the LV is commonly shown in a 2D format called a *polar map* where the center represents the apex and the outermost ring represents the base of the LV. An example of a polar map with its corresponding 3D representation of the LV is shown in Figure 1.9 where activity values are scaled to the local maximum and are shown using a colorscale. Red indicates maximal uptake and green shows a decrease of uptake.

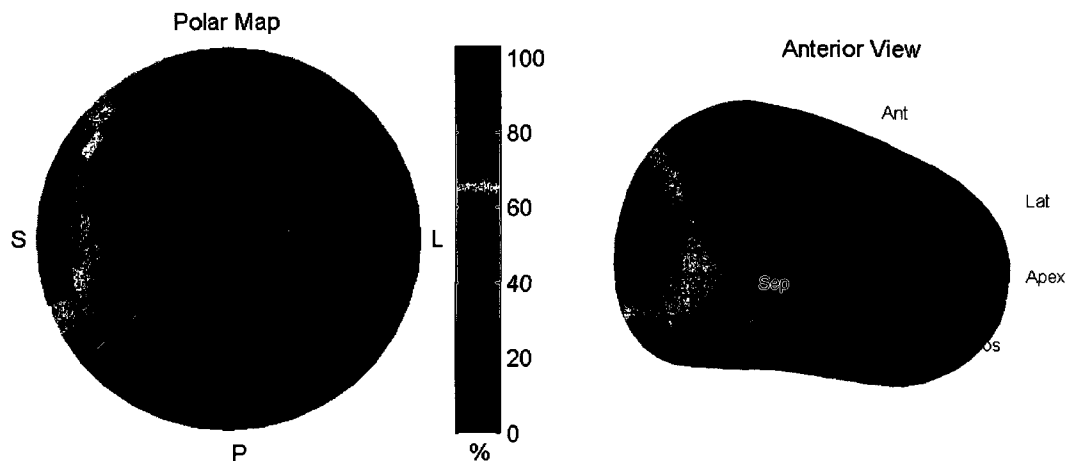
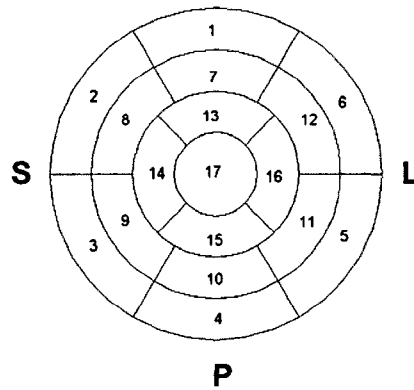


Figure 1.9 Polar map representation of the 3D shape of the LV

Segment models are used to divide polar maps of the LV into smaller regions to allow for regional quantification and localized assessment of disease. In the 17 segment model, the polar map is divided into 17 smaller regions with the outer ring representing the base of the heart and the innermost region representing the apex. This model has been recommended by ASNC (American Society of Nuclear Cardiology) as the standardized structure for myocardial perfusion imaging reports, as it allows for intra- and cross-modality comparison of myocardial perfusion data and provides the best agreement with the available anatomical data [55, 56]. This is also the clinical standard used at the UOHI. The names of the regions corresponding to the numbers displayed on the polar map are listed below.



- | | |
|------------------------|-----------------------|
| 1. Basal Anterior | 10. Mid Inferior |
| 2. Basal Anteroseptal | 11. Mid Inferolateral |
| 3. Basal Inferoseptal | 12. Mid Anterolateral |
| 4. Basal Inferior | 13. Apical Anterior |
| 5. Basal Inferolateral | 14. Apical Septal |
| 6. Basal Anterolateral | 15. Apical Inferior |
| 7. Mid Anterior | 16. Apical Lateral |
| 8. Mid Anteroseptal | 17. Apex |
| 9. Mid Inferoseptal | |

Figure 1.10 The 17 segment model

1.8 CT image acquisition

X-ray computed tomography (CT) is a non-invasive imaging modality and is used to examine internal structures of the body. During the CT scan, an X-ray source and a series of detectors rotate in synchrony around the body. X-rays are produced in a range of energies that travel through a cross-section of the subject. The detectors measure the intensity of the exiting beam in each projection; which is the integration of intensities along the line connecting the X-ray source and the detector. The measured intensity at each detector is given by:

$$I_d = \int_0^{E_{max}} S_0(E) e^{-\int_0^d \mu(x,E) dx} dE \quad (3.18.1)$$

where $S_0(E)$ is the X-ray spectrum, E_{max} is the maximum energy of the spectrum and μ is the linear attenuation coefficient. Since only the integration of all energies is measured by the detectors, the information for individual spectral energies is lost and image reconstruction using equation (3.18.1) is mathematically intractable. Alternatively, the concept of *effective energy* (\bar{E}) is used, which is defined as the energy of a mono-energetic beam which will produce the same measured intensity I_d in a given material, as measured using the poly-energetic spectrum. Consequently, equation (3.18.1) can be simplified:

$$I_d = I_0 e^{-\int_0^d \mu(x, \bar{E}) dx} \quad (3.18.2)$$

where I_0 is the X-ray intensity measured for each detector without the subject in the scanner and is acquired prior to the imaging session. The measurement of I_d provides the line integral of the linear attenuation coefficient of the particular projection. After this process is repeated for a series of angles, the distribution of attenuation coefficients is obtained through image reconstruction [36]. The FBP method is used most commonly for CT reconstruction because of its speed and accuracy [57].

In early generations of CT scanners, each slice was acquired as the X-ray source and detectors completed a full rotation inside the gantry while the patient remained static. The scan then continued by incremental movements of the examination table as it was fed through the scanner in a step-and-shoot fashion. More recently, in helical (or spiral) CT scanners, the source-detector set rotates continuously while the patient is moved at a uniform rate. The data obtained are equivalent to the patient remaining stationary and the source-detector following a spiral trajectory around the patient. With helical CT, acquisition time is reduced and the reconstruction of any number of slices is possible,

retrospectively. The slices are digitally stacked to form an accurate three-dimensional rendering.

Similar to emission scans, CT scans can be acquired in either static or gated modes. These gated scans are also called 4 dimensional CT (4DCT or cine CT) scans and allow for more accurate assessment of moving body organs.

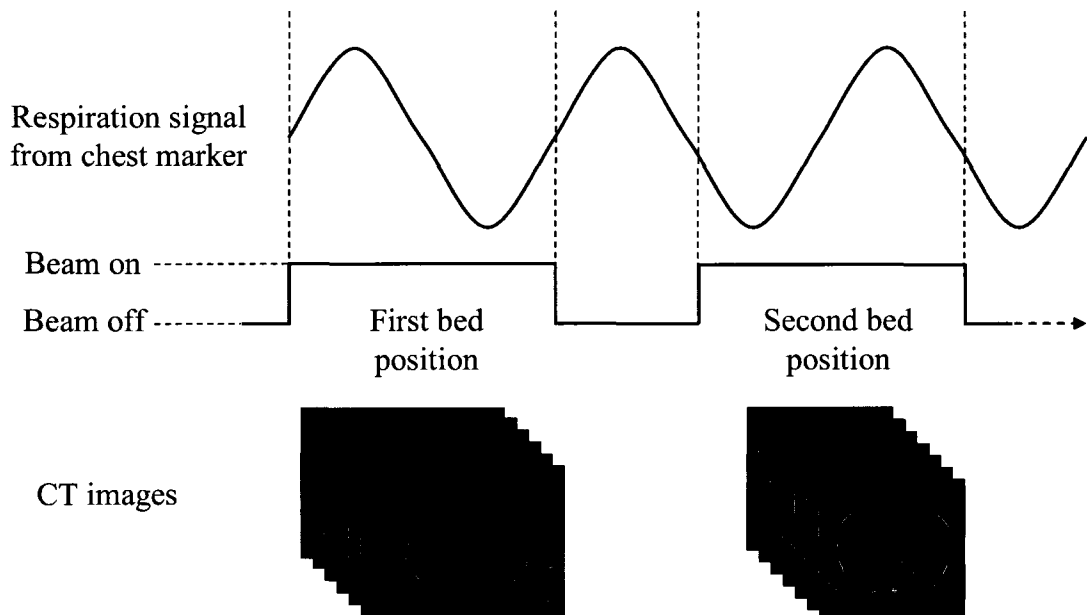


Figure 1.11 4DCT image acquisition process

In respiratory-gated scans, CT data are acquired continuously for a period of time lasting one breathing cycle at the least. If the length of the body to be imaged is more than the detector width of the CT scanner, the acquisition is repeated as the patient is moved through the scanner in a 'step and shoot' fashion. In this case, the scan incorporates multiple *bed positions*, and the 4D acquisition is repeated for every bed position. 4DCT data are sorted into several bins using a gating signal, similar to gated emission acquisitions [43, 58, 59].

1.9 Respiratory motion artifacts

Patient motion is among many sources of degradation of image quality in PET imaging. In order to reduce radiation exposure, the dose of radionuclides in PET tracers is limited, which results in low count rates during PET acquisitions. In order to compensate for this fact, scan times are prolonged and are usually in the order of minutes. During this time, voluntary and involuntary organ motions occur and are usually unavoidable.

Respiratory motion is the major contributor of involuntary organ movement in the thorax and abdomen. The mechanics of respiration involve the movement of the rib cage, diaphragm, lungs and the heart. During inspiration, the diaphragm contracts, forcing the abdominal contents downward and forward. The external intercostal muscles of the ribs contract, pulling the ribcage upward and forward, while the ribs rotate along an axis through their costal necks. During expiration, the diaphragm relaxes and the abdomen moves upward and inward and the volume of the thorax decreases. The change in thorax volume, results in inflation and deflation of the lungs [60].

The diaphragm moves about 1-2 cm during tidal (resting) breathing, and up to 10 cm during exercise. Studies suggest that the movement of the heart during respiration is correlated with the diaphragm, and can be represented primarily as a simple body translation in the Superior-Inferior direction [61, 62]. Breathing motion leads to degradation of PET images by two major mechanisms: 1) misregistration between CT and PET data leading to errors in attenuation correction and 2) averaging of the signal from multiple locations throughout the respiratory cycle producing loss of spatial resolution.

1.9.1 Errors in Attenuation Correction

Respiratory-induced motion of the heart can lead to image artifacts by introducing mis-registrations between the emission and attenuation images. With the advent of combined PET/CT scanners, CT scans took the place of transmission scans that were previously done with sources such as ^{68}Ge . The large number of photons produced by x-ray sources in CT scans provides sufficient image statistics for a more accurate AC [63]. The new generation of CT scanners is able to scan each 15cm bed position in just a few seconds, and is a big improvement over transmission scans which took about 3-10 min per bed position. Nowadays, most clinical PET/CT machines no longer include transmission sources and solely rely on CT-based AC.

The problem that was soon noted with CT-based AC was the high frequency of errors introduced when a misalignment exists between the emission and transmission data. This problem had been long known in the days of ^{68}Ge transmission scans in the context of misalignments caused by voluntary patient movement [64, 65]. While doing CT-based AC, respiratory and cardiac motion also contribute to misregistration errors [1, 66, 67]. The artifact produced usually occurs at borders between neighboring tissues with high difference in attenuation coefficients, such as in organs surrounding the lungs.

For instance, if one considers the border between the heart and the lung in myocardial perfusion scans: the photons emitted by the tracer within the heart tissue, are attenuated by centimeters of soft tissue (heart). This results in an attenuation of those photons. If the PET and CT scans are aligned, the CT-transmission scan detects the presence of attenuating soft tissue in that area and an appropriate ACF (large) is calculated. When applying AC, the measured number of photons from the area is multiplied by the ACF and the correct value of myocardial uptake is calculated.

However, if the spatial coordinates of the heart are different in the emission scan from the transmission scan, as a result of respiratory motion or patient movement, a portion of the heart could appear in the lung field. Consequently, the computer application used for AC would assume that those photons have passed through centimeters of lung tissue, resulting in a much lower ACF. The AC would not increase the measured photon count to the appropriate value and myocardial uptake is greatly underestimated. A decrease in myocardial uptake is normally diagnosed as a perfusion defect, therefore these artifacts could mistakenly lead to a diagnosis of coronary artery disease (CAD) [68, 69].



Figure 1.12 A: Good registration between PET/CT images resulting in accurate AC in (C). B: Severe misregistration between PET/CT images. The overlapping sections of the heart and lung in the fused image results in a artifactual perfusion defect seen in the anterior portion of the LV cavity (D).

Many solutions have been proposed to correct for this problem. In a study done by de Juan *et al.*, patients were asked to hold their breath at end-expiration during the CT, where the position of the heart is closest to average displacement [70]. However, regardless of which part of the cycle that is captured by the CT, it would not match the averaged representation that is inherent in the emission and ^{68}Ge -transmission scans. Automated alignment of the CT and PET data was explored in the work by Khurshid and colleagues [71]. The proposed image based method, aligned the PET and CT data by

calculating the distance between the cardiac boundaries of the PET and CT. Fuzzy clustering [72] was used to identify the portion of the PET image containing the heart and edge detection algorithms [73] were used to obtain the boundaries of the cardiac region. The software successfully resolved the hypoperfusion seen in 44% of the unaligned PET images that were the result of artifactual defects caused by the misregistration.

Pan *et al.* suggested using CT data that are averaged over many respiratory cycles [74, 75]. The attenuation map obtained by this method would represent a motion-averaged image similar to that obtained from a ^{68}Ge -transmission scan. In order to create the motion-averaged CT data in these studies, the rotation speed of the x-ray tube was slowed down so that each revolution would take one respiratory cycle to complete. This method is not favored, however, since every projection represents a different arrangement of organs at the respective respiratory phase, and this leads to artifacts in the reconstructed image. Another approach would be to acquire a cine CT scan, then average the respiratory-gated data to arrive at a respiratory averaged image [76]. Radiation exposure of the patient increases in this method, but could be controlled by lowering the CT tube current as proposed by Kamel *et al.* [63].

In a study by Alessio *et al.*, AC of cardiac PET studies was compared using intensity-maximum, and respiratory-averaged cine CT data. The intensity-maximum CT image was generated by taking the maximum intensity of every pixel over all respiratory-gates of the cine data. Images from 10 clinical studies were reprocessed using AC with a standard helical CT map, an average CT map, and an intensity-maximum CT map. The alignment of the CT and PET images and the presence of visible artifacts in the PET images were assessed. The authors found that properly aligned images without visible

artifacts were obtained in 77% of cases with average-CT and in 88% of cases with max-intensity CT suggesting that the max-intensity approach might also be beneficial [77].

Cine-CT data can also be synchronized to the gated emission data so that each phase of the respiratory cycle in the emission scan is corrected using its corresponding attenuation map. Nehmeh *et al* [43] evaluated this approach in the context of lung cancer imaging. The accuracy of the co-registration in this study was evaluated by measuring the displacement between lesion centroids in 4D-PET/CT-helical and clinical CT, and that between 4D PET/CT and 4D-CT. The phase-matched method improved co-registration between PET-CT images by as much as 41%.

1.9.2 Motion Blurring

The second disadvantage of motion is image blurring. During long PET acquisitions, the motion of the source of radioactive emission causes the spread of activity values along the path of movement. This leads to motion blurring which is characterized by loss of contrast in PET images, and is proportional to the magnitude of the motion. The final image represents a motion-averaged picture of tracer distribution in the body (Figure 1.13 B).

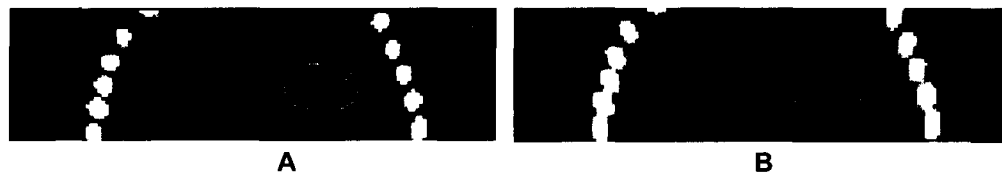


Figure 1.13 A coronal slice from a digital phantom simulating fused (overlaid) PET/CT images. The grayscale background represents the CT image while the colored cavity represents the PET image of the heart. Image (A) is the idealistic case where no motion-blurring is seen as a snapshot view of the respiratory cycle is captured. Image (B) shows the effect of motion blurring.

By using gated acquisitions (see section 1.5.3), one can reduce motion blurring. However, image statistics are limited as the total number of counts is divided by the

number of gating bins. In order to improve statistics, image volumes can be registered to one reference frame, and then summed; or averaged alternatively to preserve quantitative accuracy.

Various methods have been proposed for aligning these images. Manual registration of gated images data is possible but time consuming and prone to errors due to inter- and intra- observer variability. Therefore, many sophisticated methods have been developed in order to allow computer-based registration.

A crucial step in registering images is to estimate the motion of the organs between phases. In some studies, respiratory motion of organs is estimated using gated CT images [78, 79]. Although these studies are often successful due to the high resolution of CT imaging, the increase in radiation dose for the patient is not justifiable for most diagnostic procedures. Optical flow algorithms have been proposed to calculate the motion between the gated image frames [80-82]. In the work by Dawood *et. al.* [82] motion vectors between pixel positions of the myocardium were calculated for every gated image using optical flow algorithms. These vectors were then inverted in order to move these images to a reference position, while deforming the 3D image according to the motion vector field. The registered images were then summed in order to generate a motion-free data set. Clinical ^{18}F -FDG images were used for clinical evaluation which typically have better image statistics compared to ^{82}Rb -PET images, therefore applicability of the method to ^{82}Rb -PET imaging remains to be evaluated.

Slomka *et. al.* [83] have proposed a different approach to reduce blurring due to cardiac contraction in myocardial perfusion SPECT imaging. Although cardiac motion is substantially different from respiratory motion, methods that are used to identify the

spatial coordinates of the myocardium in ECG-gated images can be used towards respiratory gated studies. In this method, maximal-count circumferential profiles are identified on mid-ventricular transaxial slices that are manually segmented from the original image. The apex is then identified as the point of maximum gradient along this profile, and the line of minimum counts passing through the apex is used as a proxy for the LV's long axis. This process is repeated for all angles about the LV's long axis and a maximal-count myocardial surface is thus extracted. The surface is then fitted to a quadratic surface [84]. Using the spatial coordinates of the quadratic surfaces, gated images are warped to fit to a reference frame and then summed. This method has been shown to improve image contrast noise statistics when compared to non-corrected images. However, the improvement on image quantification was not assessed due to the inaccuracies caused by nonlinear warping of the images.

1.10 Thesis Objective

The objective of this work is to develop and validate a correction method for reducing inaccuracies caused by respiratory motion of the heart in ^{82}Rb -PET images. Application of this method will lead to a more accurate measurement of myocardial perfusion. To accomplish this, automated methods to localize the myocardium were adapted to detect the position of the myocardium in all phases of respiratory-gated PET images. New algorithms were then developed to align these images in order to reduce the amount of motion blurring. Accurate attenuation correction approaches were implemented to reduce image artifacts due to attenuation errors. Finally, the combined effect of respiratory phase-alignment and accurate attenuation correction techniques was evaluated.

The objective of this work is to develop and validate a correction method for reducing inaccuracies caused by respiratory motion of the heart in ^{82}Rb -PET images. Application of this method will lead to a more accurate measurement of myocardial perfusion. To accomplish this, automated methods were developed to localize the myocardium in respiratory-gated PET images and align these images in order to reduce the amount of motion blurring. Accurate attenuation correction approaches were also studied to reduce image artifacts due to attenuation errors. Finally, the combined effect of respiratory phase-alignment and accurate attenuation correction techniques was evaluated.

In Chapter 2, the effect of the correction methods to improve image uniformity was evaluated for homogeneous myocardial images. Computer simulations were used to simulate respiratory motion blurring effects in a controlled environment and the performance of the correction methods was studied on simulated PET images. The development of methods for respiratory-phase alignment of PET images is also illustrated in this chapter. Finally, to further support the simulation studies, the correction methods were applied to a ^{82}Rb -PET study of a swine. It is hypothesized that motion compensation in addition to accurate attenuation correction improves image homogeneity. Furthermore, we also hypothesize that phase-matched attenuation correction will lead to more accurate correction than other approaches.

In Chapter 3, the correction methods are applied to abnormal images. We hypothesize that respiratory phase alignment would help increase the accuracy of the size and contrast of defects (myocardial regions of reduced activity indicative of reduced perfusion) by reducing the errors introduced by motion blurring in the uptake images. In

order to show feasibility of applying the developed methods to clinical scans, the correction methods were applied to an anonymized patient's ^{82}Rb cardiac perfusion scan.

Chapter 2 Motion Compensation for Respiratory-Gated ^{82}Rb -PET

2.1 Simulation study

In order to evaluate the magnitude of errors introduced from respiratory motion of the heart and to verify the performance of the automated phase-alignment algorithm, simulated experiments are needed to analyze the problem in a controlled environment. Digital phantoms simulating the human anatomy and physiology were used in conjunction with a Monte-Carlo based PET simulator to produce simulated images of a respiratory-gated dynamic ^{82}Rb -PET acquisition. Image processing followed to align the myocardium to a reference frame in all image volumes. All images were then quantified and compared to study the performance of the applied correction. A flow-chart of the process is shown in Figure 2.1.

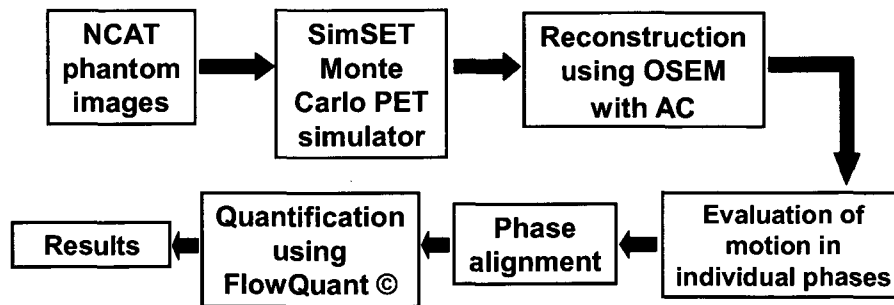


Figure 2.1 Simulation flow-chart.

2.1.1 The NCAT phantom

The nonuniform rational b-splines (NURBS)-based cardiac torso phantom (NCAT) was used for the experiments [85]. The NCAT phantom is a four-dimensional anthropomorphic digital phantom that models the average human torso. The phantom provides digital models for the human anatomy that can be easily altered to introduce variations in anatomy and activity distributions in various organs. Respiratory and cardiac motion specifics such as amplitude and frequency can also be controlled via editing input parameter files, and are based on 4D tagged MRI and 4DCT images of normal volunteers [85].

In this study, a 5 second respiratory period was chosen in which the displacement of the heart was 2 cm superior-inferior. No anterior-posterior or lateral movement of the heart was simulated as studies suggest that the movement of the heart due to respiration is primarily superior-inferior [61, 62]. No other changes were made with respect to the default settings of the phantom. The respiratory period was divided into 10 phases; an image was created for each phase of the period where phase 1 corresponds to the start of breathing and phase 10 corresponds to end-exhalation. These images will be called “respiratory phases” hereafter. All images were averaged over the 1s second cardiac cycle so that no cardiac contraction movement is modeled. No motion averaging was done over the time span of the length of the gate ($5\text{s} / 10 = 0.5\text{s}$), instead the center point of each time bin was taken. Using variables provided at input, the phantom generates two image volumes using variables provided at input: the activity and attenuation maps. Each image volume is $128 \times 128 \times 128$ pixels in size, starting at the top of the rib cage and ending under the diaphragm.

In order to model a respiratory-gated dynamic ^{82}Rb -PET acquisition, phantom images were generated to represent organ activity distributions for 17 time points in the course of image acquisition. The images corresponding to each time point form the *dynamic frames* of the dynamic data acquisition. The number of frames and their length are as follows: $12 \times 10\text{s}$, $2 \times 30\text{s}$, $1 \times 60\text{s}$, $1 \times 120\text{s}$, $1 \times 240\text{s}$ for a total of 10 min, 17 frames. The activity distributions for the 10 respiratory phases in each dynamic frame are the same however the arrangement of the organs differ due to respiratory motion. This results in 170 activity maps with matching attenuation maps.

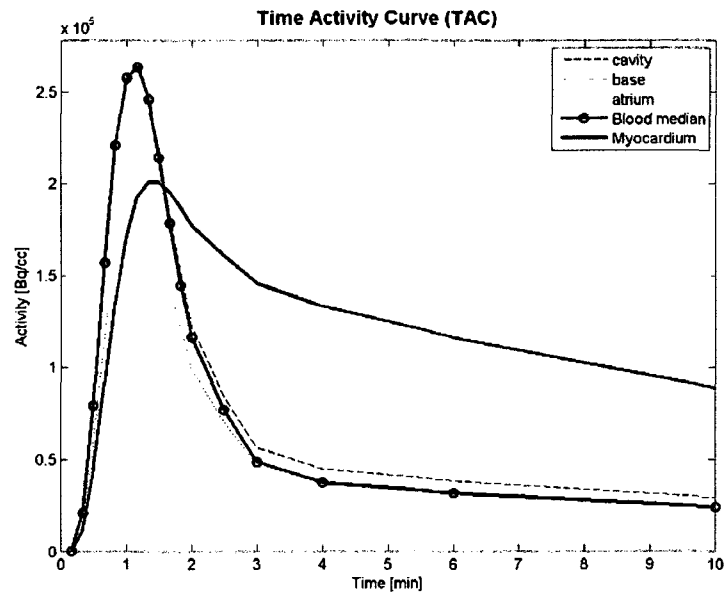


Figure 2.2 Time-activity curves showing the idealized activity distribution of the blood and heart cavities that are used in generating the phantom

The activity distribution in each image volume was modeled to represent clinical values. The arterial blood input function used, had been modeled according to [86] and the parameters were adjusted to fit to normal patient values [87]. Activity distribution in the myocardial walls were modeled using the input function and the one-compartment model for ^{82}Rb , which have been verified for ^{82}Rb kinetic modeling of clinical data [88]. Activity distributions for the liver, stomach wall, lungs and remaining soft tissues were

based on TAC curves measured from regions of interest applied to patient data. Lung attenuation coefficients were also extracted from clinical CT images and assigned to the attenuation maps, in accordance to each respiratory phase [87].

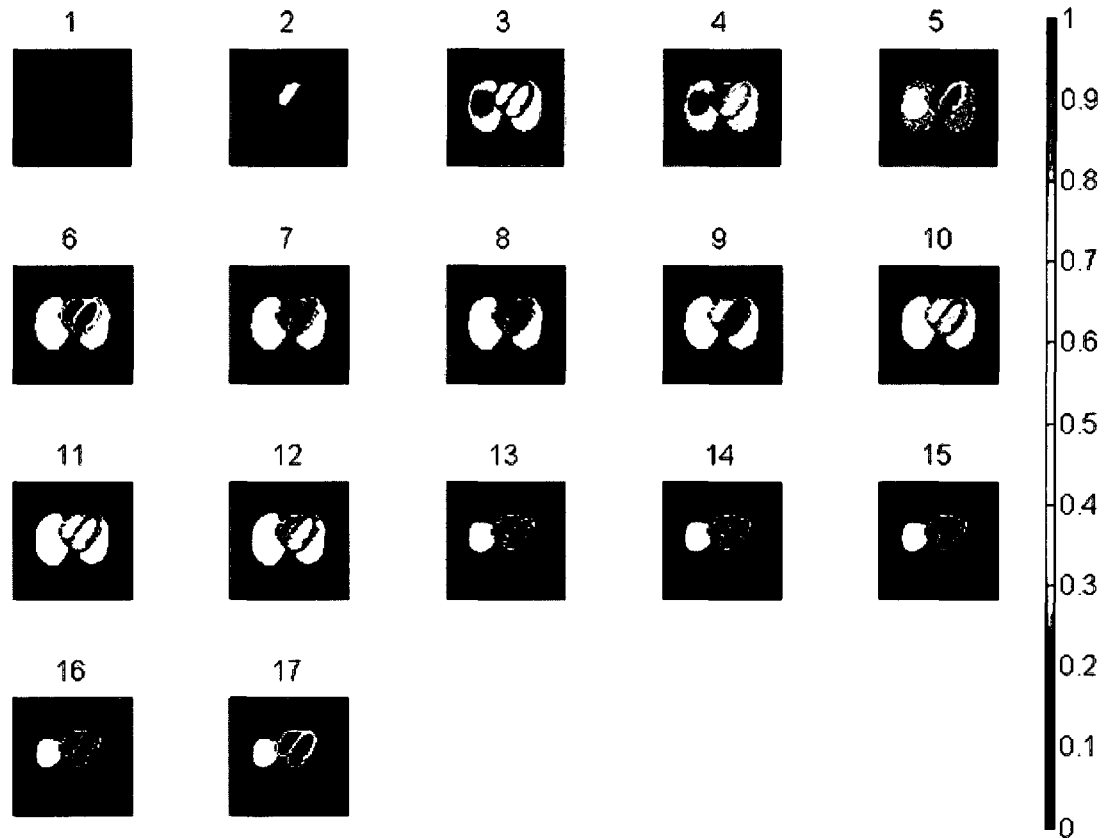


Figure 2.3 A transaxial slice followed through NCAT activity maps for each dynamic frame, showing the relative activity distribution in the myocardium

2.1.2 SimSET Simulations

A dynamic ^{82}Rb -PET acquisition was simulated using SimSET (University of Washington, Seattle) [89], a Monte Carlo based simulation software. System parameters were configured in order to model 2D acquisitions on the Discovery LS PET/CT scanner - General Electric Healthcare Technologies. The scanner has a 15 cm field of view and 18 bismuth germanium oxide crystal detector planes. Separate emission data were generated for each of the 170 respiratory phases. The number of photons simulated was 400 million

for each phase, which allowed for good quality images. Approximately 200-300 million of those photon were detected during the simulation. In a typical clinical study, the number of detected photons is approximately 200 million for the entire dynamic data set. Thus, our simulations have 170 times the clinical counts, corresponding to more than a $10\times$ decrease in noise. Note that system dead-time, randoms and scatter corrections were not included in this simulation in order to allow for examination of underlying effects of motion and attenuation correction without the presence of other potentially complicating factors. Other factors, such as system geometries, system spatial resolution and energy resolution were included in the simulation.

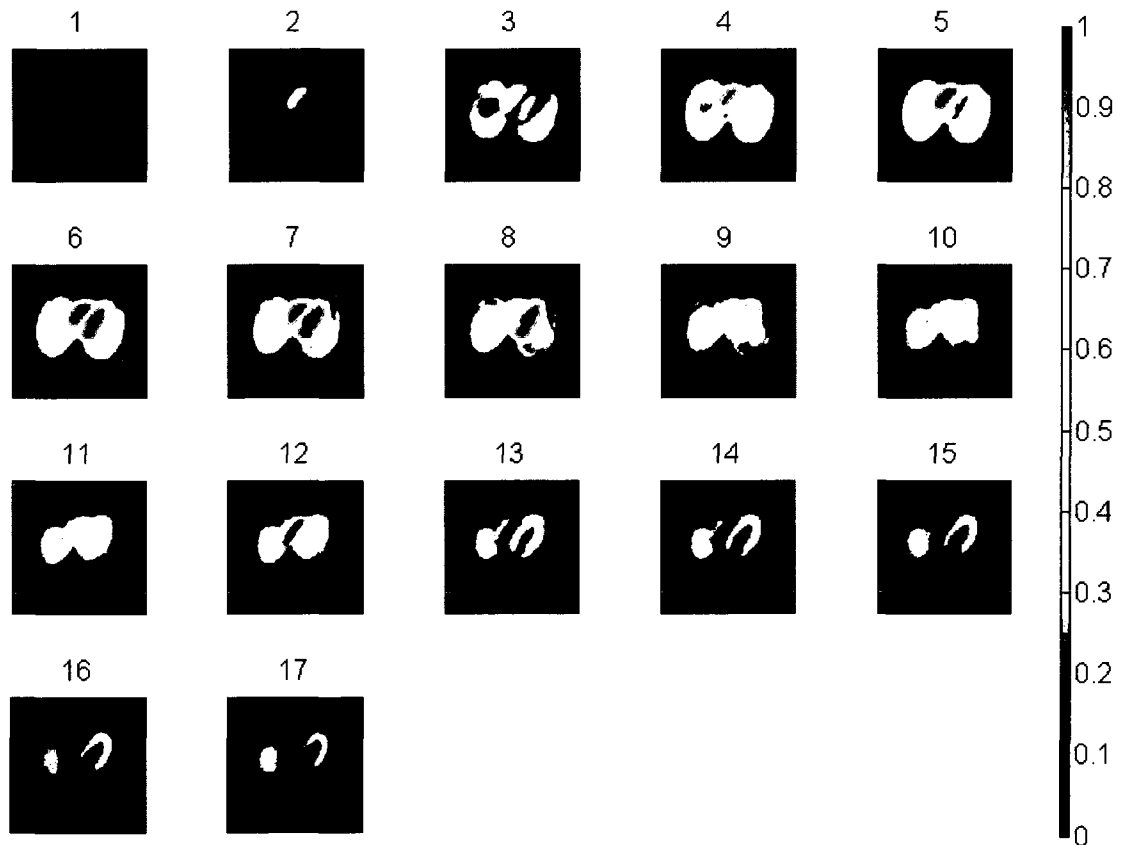


Figure 2.4 Figure 2.3 A transaxial slice followed through simulated PET images showing the relative activity distribution in the myocardium in each dynamic frame

Sinograms for each respiratory phase were reconstructed using an OSEM algorithm with CT-based attenuation correction (CTAC). Eight subsets were considered for the reconstruction and 3 iterations were completed for each image. The attenuation maps generated from the NCAT simulations were used to represent the CT maps for each respiratory phase. Thus emission and transmission images are automatically aligned. Three different CTAC approaches were considered:

1) Respiratory phase-matched CTAC. Each respiratory phase of the emission data is corrected using the attenuation map from its corresponding respiratory phase. This approach should provide the most accurate AC.

2) Respiratory averaged CTAC. Attenuation maps for all respiratory phases of each dynamic frame are averaged over the respiratory cycle. This approach has shown to be effective in minimizing errors in ungated cardiac PET studies [75].

3) Maximum intensity CTAC. The maximum intensity of every pixel position due to changes in attenuation during the respiratory cycle is taken. This approach which was proposed by Alessio *et al.* [77] showed better promise than the averaged CTAC in clinical cases.

After reconstruction, the images were smoothed using a 9 mm FWHM Gaussian filter. Post-reconstruction filtering is commonly applied to clinical images to reduce noise.

2.1.3 Respiratory phase alignment

Algorithms of an in-house developed program, FlowQuant® were used to automatically detect the heart in the simulated images. As introduced in section 1.7, the software automatically finds the size and location of the LV in each image by fitting

partial ellipses in 3 orthogonal planes, followed by registration to a deformable spline model. A sample of the registration is shown in Figure 2.5

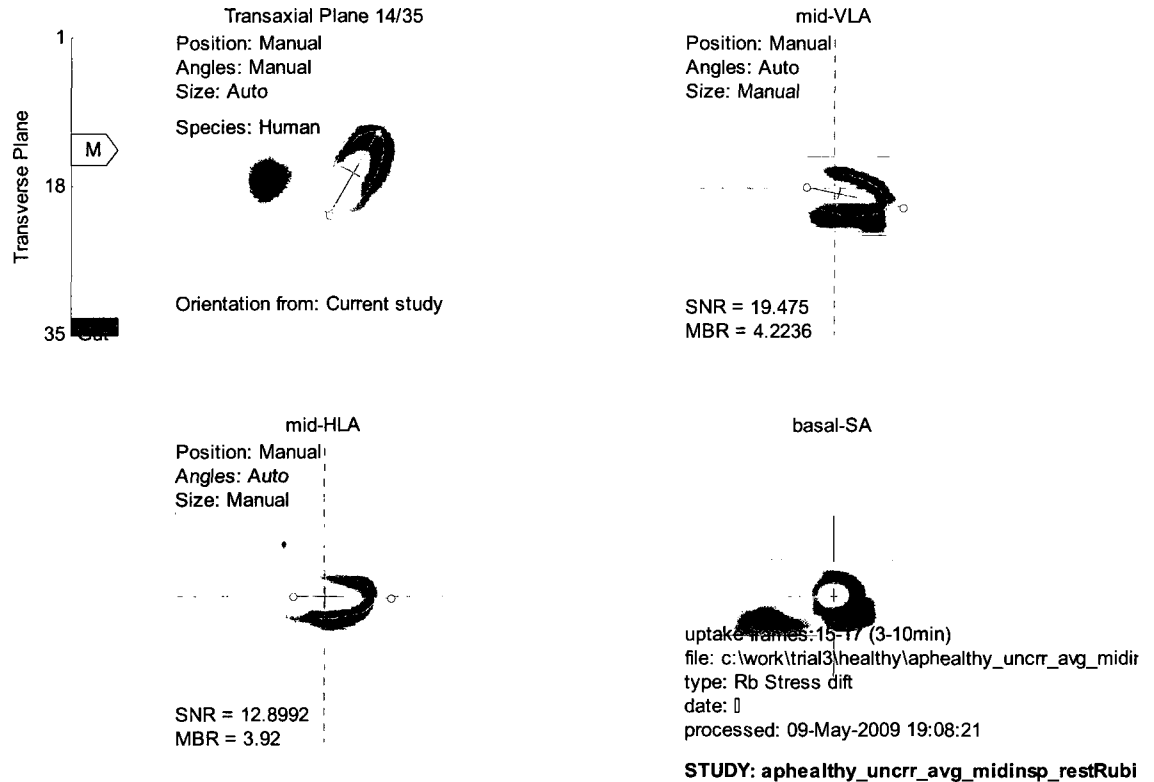


Figure 2.5 A sample from the registration software showing the myocardium (clockwise from top left): transaxial view, vertical long axis view, short axis view and the horizontal long axis view.

The sum of the last three dynamic frames was used to find the location of the LV, as later frames contain primarily myocardial uptake with little blood-pool activity making the LV more visible. The fitting algorithms mentioned above were modified to be applied to every respiratory phase, and the center point coordinates of the ellipsoid fitted to the LV was recorded. Using these coordinates, the entire set was translated in 3 dimensions using linear interpolation to align the centers of the LVs to a reference coordinate. In the course of fitting, rotation was considered but did not further improve the alignment due to limited spatial resolution.

In order to generate a motion compensated (MC) image set, the aligned respiratory phases were averaged over the respiratory cycle after AC. To create a motion-blurred image set, the images for each respiratory phase were averaged without alignment. To simulate a motion-free “true” image set, a single respiratory phase from the respiratory phase-matched CTAC dataset was selected for each dynamic frame.



Figure 2.6 Lateral views of five respiratory frames showing fused (over-layed) emission and transmission images. The LV (shown in gold) shows axial translation across the five respiratory frames. Lung inflation can also be seen from left to right.

2.1.4 Phase alignment accuracy

In order to assess the accuracy of the automated phase alignment process, image volumes were generated containing half-ellipsoids to simulate the LV in PET images. The half-ellipsoids were created with 100% contrast against a zero background, and then smoothed with a 9mm Gaussian kernel. The image volumes were $128 \times 128 \times 35$ pixels in size, similar to the simulated data. The images used in this analysis were noise-free. The fitting algorithms were applied to measure the spatial coordinates of the center of the half-ellipsoids and results were analyzed to examine the sensitivity and reproducibility of these algorithms.

In this experiment, 5 images were generated (without PET simulation) wherein the center of the half-ellipsoid in each image differs by 1 pixel on x, y and z axes between two consecutive images. This range of motion between images is aimed towards replicating a similar situation seen in the simulation data in which the maximum displacement of the heart between respiratory-gate images is approximately 2 cm along

the long axis of the body (z axis). This translates to approximately 4.6 pixels using a conversion factor of 4.285 mm/pixel which is assigned by the software that generates the phantom.

For all images, the long axis of the ellipsoids makes a 40° angle with the lateral (left-right) axis of the body on the transverse plane, and a -10° angle with the lateral axis of the body on the vertical long axis plane of the heart, similar to that seen in clinical images. A superimposed view of the first and last image volumes is shown in Figure 2.7.

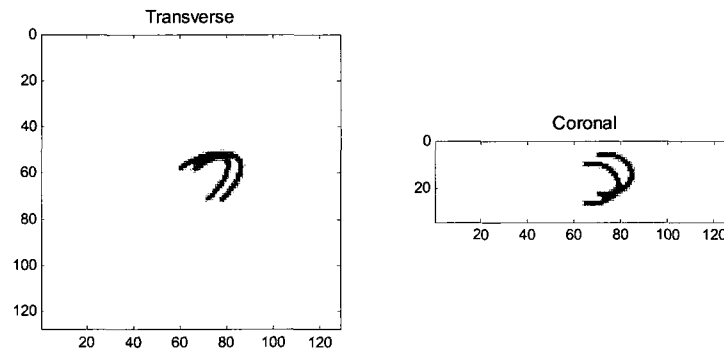


Figure 2.7 Transverse and Coronal views of 2 super-imposed half-ellipsoids generated for phase alignment accuracy test

The fitting process was repeated ten times for each of the 5 images. User interaction was often needed to optimize the fit. Figure 2.8 shows the measured coordinates compared to the coordinates used to generate the half-ellipsoids (the expected coordinates). The average of the measured coordinates is also shown. The source of variability in the measured data is believed to be a combination of the performance of fitting algorithm (see equation (3.13.4)) and user interaction in the fitting process.

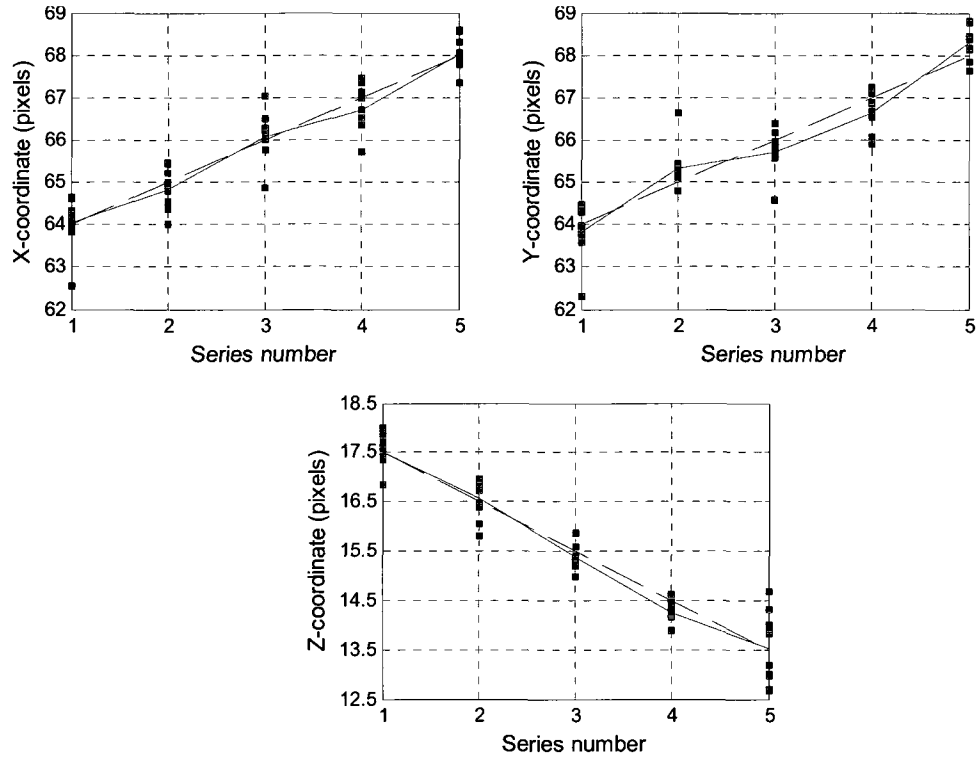


Figure 2.8 Coordinates of the center of the half-ellipsoids measured by the fitting algorithms. The blue (solid) line shows the average of the measured data points and the red (dashed) line represents the coordinates used to generate the half-ellipsoids.

A Bland-Altman assessment was used to demonstrate the difference between repeated measurements. This type of analysis plots the difference between the measured and expected coordinates for each known ellipsoid center position. Bland-Altman plots for x, y and z coordinates of the measured center positions of the ellipsoids compared to the expected positions are shown in Figure 2.9. The black (dashed) lines indicate ± 2 times the standard deviation of differences and are ± 1.022 , ± 1.120 and ± 0.830 pixels for x, y and z respectively. The blue (solid) lines represent the mean difference for every plot and are -0.066 , -0.070 and -0.050 for x, y and z which points to a slight negative bias.

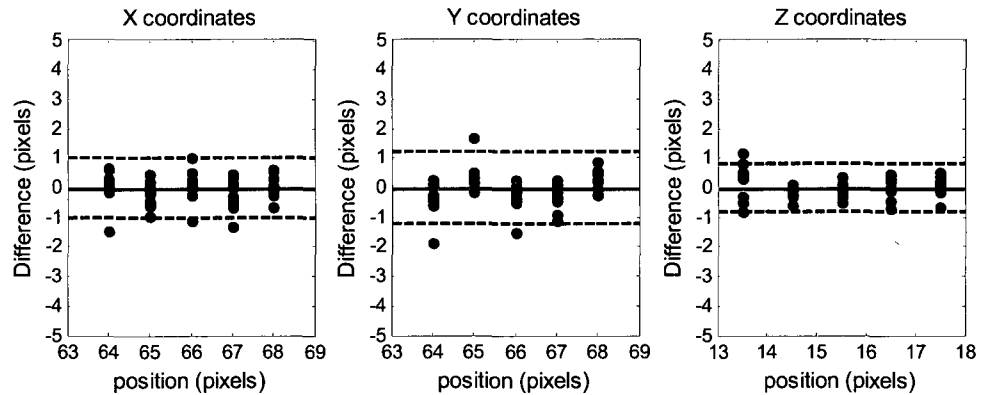


Figure 2.9 Bland-Altman plots for x, y and z pixel coordinates of the measured center positions of the ellipsoids compared to the expected positions (10 comparisons at each position). The black (dashed) lines indicate the $\pm 2SD$ of differences and are 1.022, 1.120 and 0.830 pixels for x, y and z respectively. The blue (solid) lines represent the mean difference for every plot (-0.066,-0.070,-0.050).

The standard deviation of differences are (0.511,0.600,0.415) pixels on x, y and z. These errors translate to (1.600,1.873,1.777) mm using a conversion factor of (3.125,3.125,4.285) for simulated images shown in Chapter 2. This results in an 8% uncertainty in comparison to the 20 mm range of motion on the z axis for the simulated data.

As seen in Figure 2.9, the accuracy of the algorithm in finding the coordinates of the LV is independent of the position of the LV in the image as no bias is seen across different center positions. This investigation evaluated the errors introduced through processing of the data. A more comprehensive evaluation is needed to investigate the additional errors potentially produced by the noise in the images.

2.1.5 Results

In-house software, FlowQuant® was used to obtain tracer uptake and flow values, and to generate polar map representations of the images. The polar maps were divided into 17 segments as described in section 1.7. In order to evaluate the performance of the

correction method, motion-compensated polar maps were compared with the motion-free polar maps. We hypothesize that motion compensation (MC) would help increase polar map uniformity by reducing the errors introduced by motion blurring in normal myocardium. Furthermore, we also hypothesize that phase-matched attenuation correction will lead to more accurate correction than other approaches. By comparing different attenuation correction techniques, the combined effect of MC and AC are investigated.

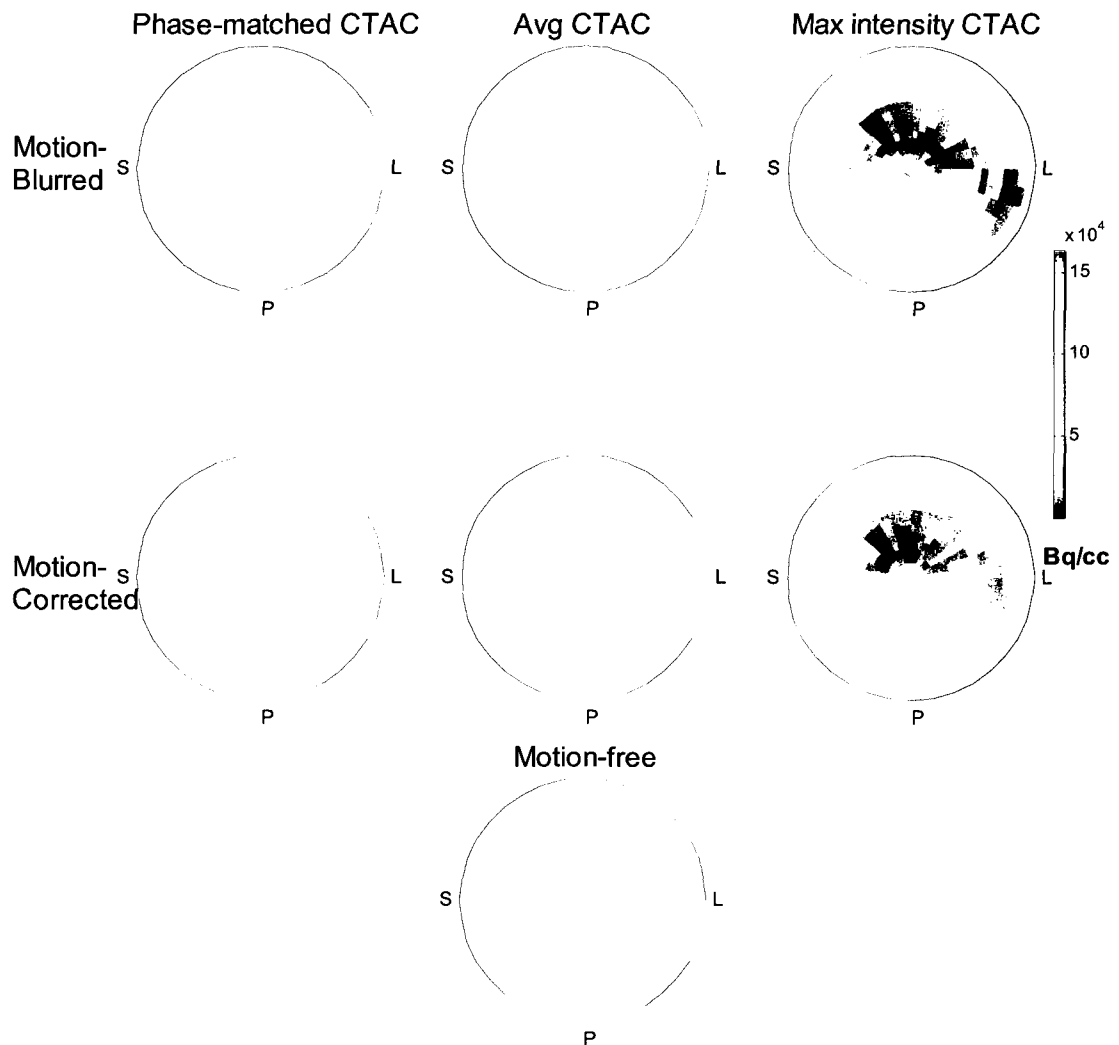


Figure 2.10 Absolute uptake polar maps showing improvement in image uniformity after motion compensation. A reduction in uptake is seen in the anterior-lateral, posterior-septal and apical regions where most motion-averaging occurs. Image uniformity improves after motion-correction (second row). The motion-free image corresponds to the image from a single respiratory phase (end-expiration). In this figure, S=septal, L=lateral, P=posterior (inferior) wall of the heart.

Uptake polar maps are shown in Figure 2.10 using a scale for which the voxel values have been expressed in units of absolute activity concentration. In the first row, a spatial average was taken from attenuation corrected gated PET images without applying MC. In the second row, MC followed AC and therefore motion-corrected PET images were averaged after MC. These plots allow us to compare the effect of different AC schemes, as well as their effect on the images before and after MC.

These polar maps represent the results for the average of the last 3 dynamic frames. For the normally perfused myocardium represented by these simulations, the distribution of activity in the polar maps should be completely uniform. As seen in the polar maps, MC reduces the non-uniformity seen in the septal-posterior and anterior-lateral regions. The apical regions show decreased values which relates to the rotation of the LV in addition to its superior-inferior movement, and the resultant motion blurring. These regions also show improvement in uniformity after MC. The septal wall of the LV is shorter than the lateral wall in the phantom heart model which causes the reductions in the baso-septal region that are noticeable in all polar maps. The fact that these regions with suppressed values are seen in the motion-free image, suggests that they are inherent non-uniformities, and not the result of a respiration artifact.

The uptake polar maps in Figure 2.10 were segmented following the 17 segment model (see section 1.7) and the average of uptake values in each segment were used to represent that segment (figure not shown). A paired T-test analysis was done in between the segmental values of the “motion-free” polar map, versus the “motion-blurred” and “motion-corrected” polar maps in Figure 2.10 in order to determine significance of differences. No significant differences were seen at the 5% significance level except for the max-intensity CTAC polar maps. However, the p values for the “motion-corrected” phase-matched and averaged CTAC methods were an order of magnitude larger than that for the “motion-blurred” polar maps ($p = 0.600, p = 0.120$ vs $p = 0.063, p = 0.065$ respectively). This suggests that MC is effective in reducing the differences with respect to ‘truth’.

In order to better visualize the differences between these polar maps and the motion-free polar map, a pixel-by-pixel percent difference map was generated (Figure 2.11). The non-uniformities seen in the septal-posterior and anterior-lateral regions of the non-corrected polar maps are believed to be caused by the motion averaging associated with the motion of the heart during respiration. Figure 2.11 shows that these errors can inflict point errors as high as 40% for the max-intensity CTAC image and approximately 16% for the phase-matched and averaged CTAC images which normalize after MC.

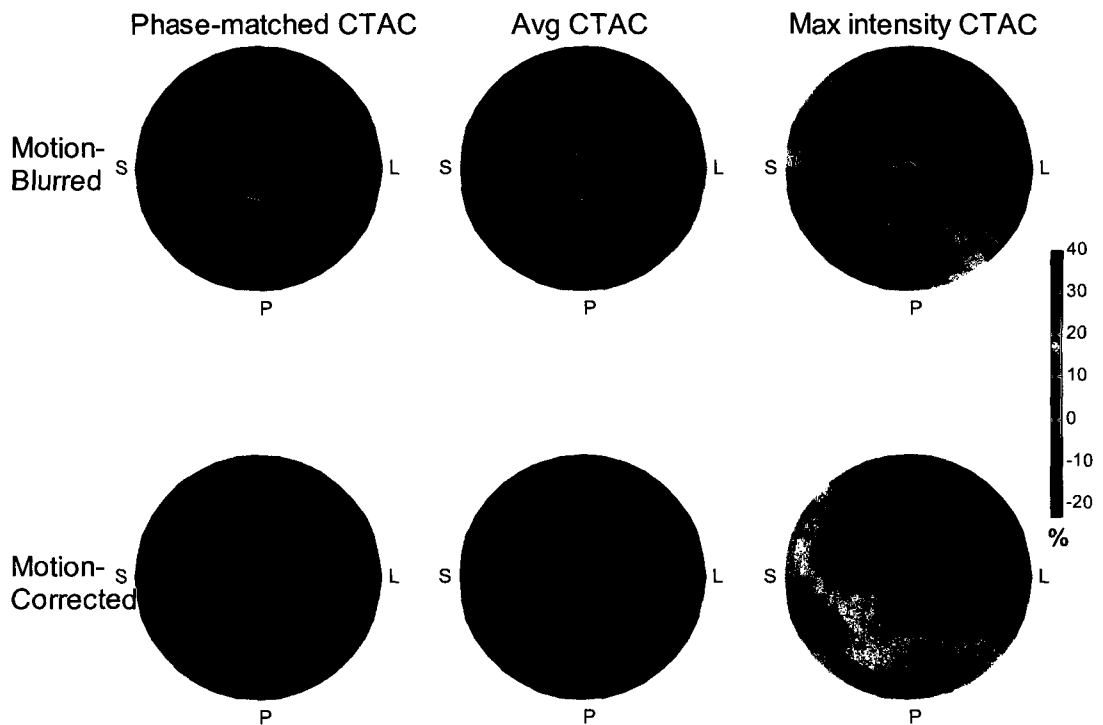


Figure 2.11 Percentage difference polar maps for the uptake polar maps shown in Figure 2.10 compared to the motion-free image.

In order to obtain a more regional measure of uniformity, the difference maps shown above were divided into 17 segments according to the 17 segment model (see section 1.7). The mean of the pixel-by-pixel errors in each segment was calculated. These errors are hereafter referred to as segmental mean percentage errors (sMPE).

The sMPE value for each segment is shown on the respective segment in Figure 2.12. The standard deviation of sMPE values for each polar map is used as a measure of uniformity of the differences from the motion free image.

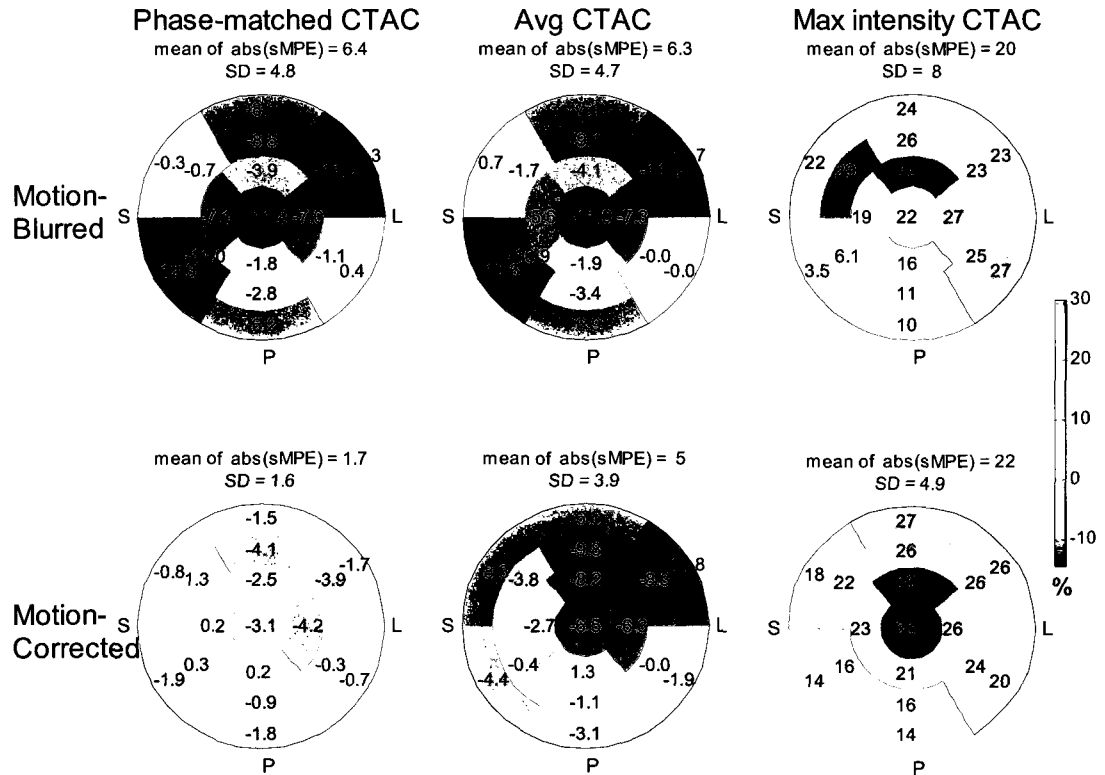


Figure 2.12 Segmental mean percentage errors for the absolute uptake maps shown in Figure 2.10, relative to the motion-free image. The standard deviation (SD) of these errors serve as a measure of image uniformity.

As seen in Figure 2.12, the uniformity of the differences with the motion-free image decreases after MC in all cases while the mean sMPE value decreases in all instances except for max intensity CT-AC images.

In order to determine the significance of differences due to MC, a paired T-test analysis was done between the sMPE error values in the motion-corrected and motion-blurred uptake polar maps for each CTAC method. Differences were significant at the 5%

significance level in the case of phase-matched CTAC ($p < 0.001$) and the averaged CTAC ($p = 0.0445$) but not for the maximum-intensity CTAC images ($p = 0.201$).

Uptake maps are usually evaluated on a relative basis in the clinic, as opposed to those shown in Figure 2.10 which have absolute units of Bq/cc . In order to evaluate relative change due to the correction methods, the polar maps shown in Figure 2.10 were segmented following the 17 segment model and the average of uptake values in each segment were used to represent that segment. Global uptake values were then normalized to the maximum segmental value in each polar map. The normalized polar maps are shown in Figure 2.13.

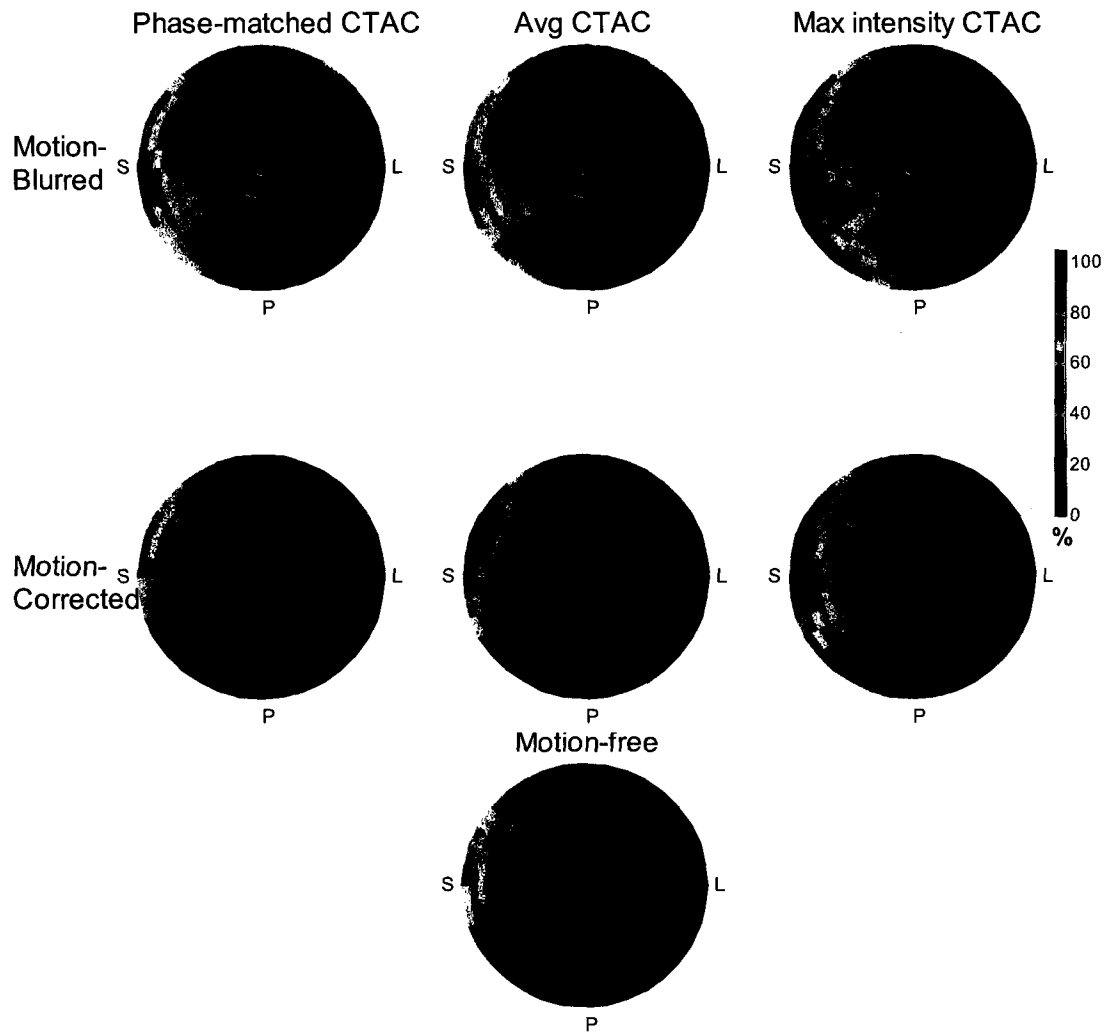


Figure 2.13 Self normalized uptake polar maps. The polar maps shown in Figure 2.10 were segmented following the 17 segment model and the average of uptake values in each segment were used to represent that segment. Images were then presented as a percentage of the maximum segmental value in each polar map.

Segmental mean percentage errors for these polar maps, compared to the normalized “motion-free” polar map were calculated and are shown in Figure 2.14. The error maps calculated from normalized data demonstrate a better estimation of relative image uniformity since normalization reduces the difference between the mean value in all polar maps and the motion-free map mean value. This is visibly seen by comparing the average errors of the max-intensity CTAC maps in Figure 2.14 and Figure 2.12. However, the remaining errors seen in the max-intensity CTAC correction method are

nevertheless larger than the phase-matched and average CTAC method which suggest that the overcorrection of attenuation is not distributed uniformly throughout the myocardium. Motion-compensation helps reduce non-uniformity by 2.3% in the max-intensity CTAC image. The uniformity and mean error value for the phase-matched and average CTAC methods remain similar to that of Figure 2.12.

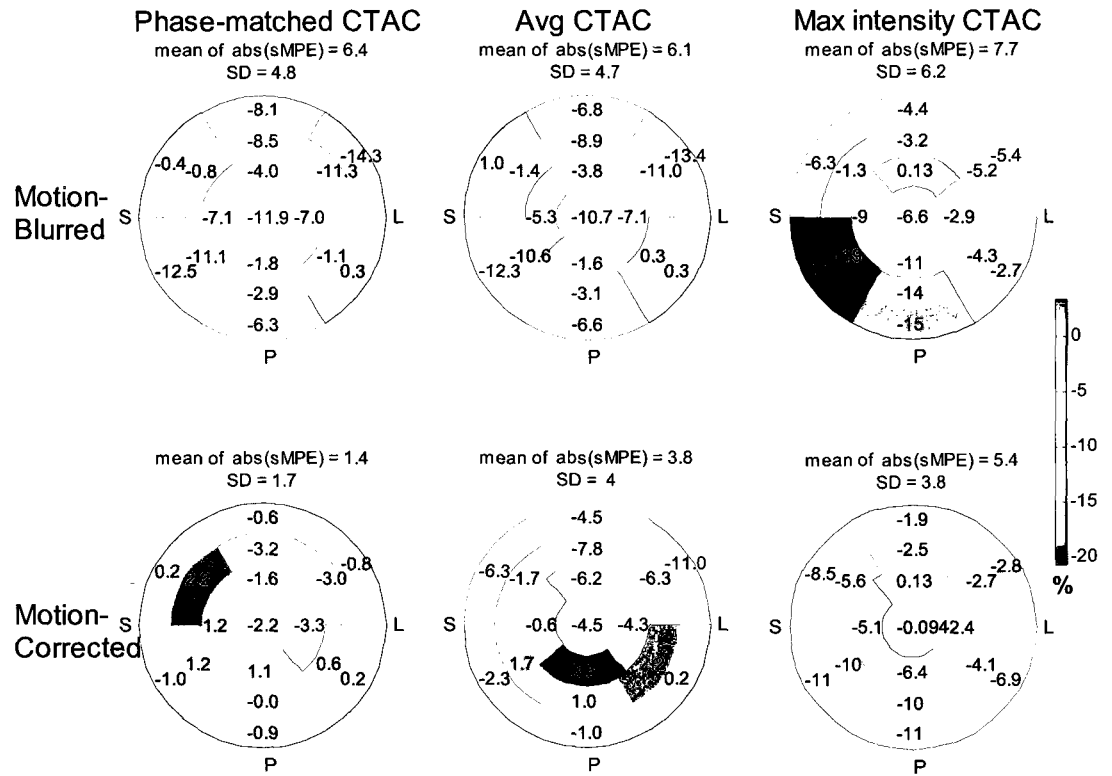


Figure 2.14 Segmental mean percentage error calculation for normalized uptake images, relative to the motion-free polar map

Similar analyses have been completed for blood flow values. Figure 2.15 shows flow distribution in the LV in units of $mL/min/g$ while Figure 2.16 shows the segmental mean percentage error calculation. In all instances, MC increases image similarity (decreases the SD of the differences) with the best improvement coming for phase-matched CTAC. Motion compensation reduces the sMPE in all cases.

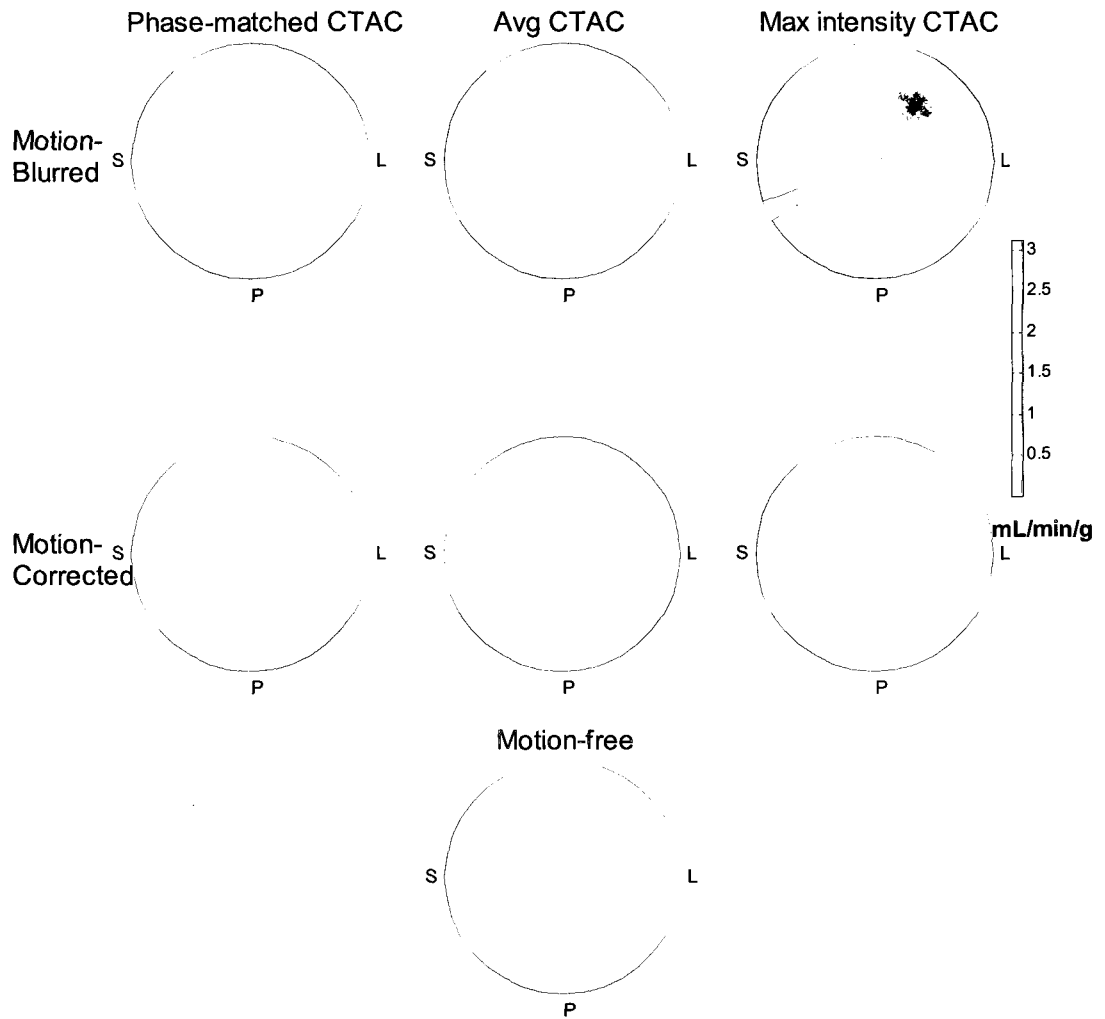


Figure 2.15 Absolute blood flow polar maps show improvement in similarity with the motion-free after motion compensation. The motion-free map is the blood-flow distribution for a single respiratory phase taken at end-inspiration and serves as our motion-free standard. All polar maps are expressed in absolute units of blood flow: mL/min/g. Blood-flow similarity with the motion-free image improves after motion correction.

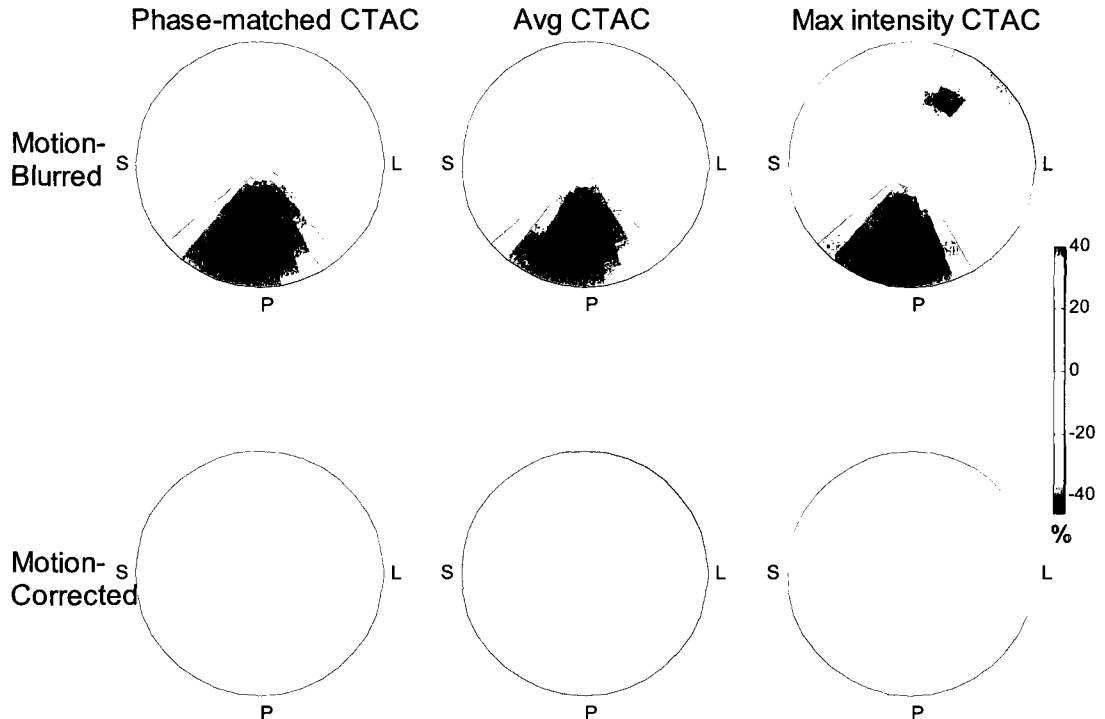


Figure 2.16 Percent difference maps shown for the absolute blood flow polar maps shown above in Figure 2.15, compared to the motion-free map. The largest errors are seen in the posterior region.

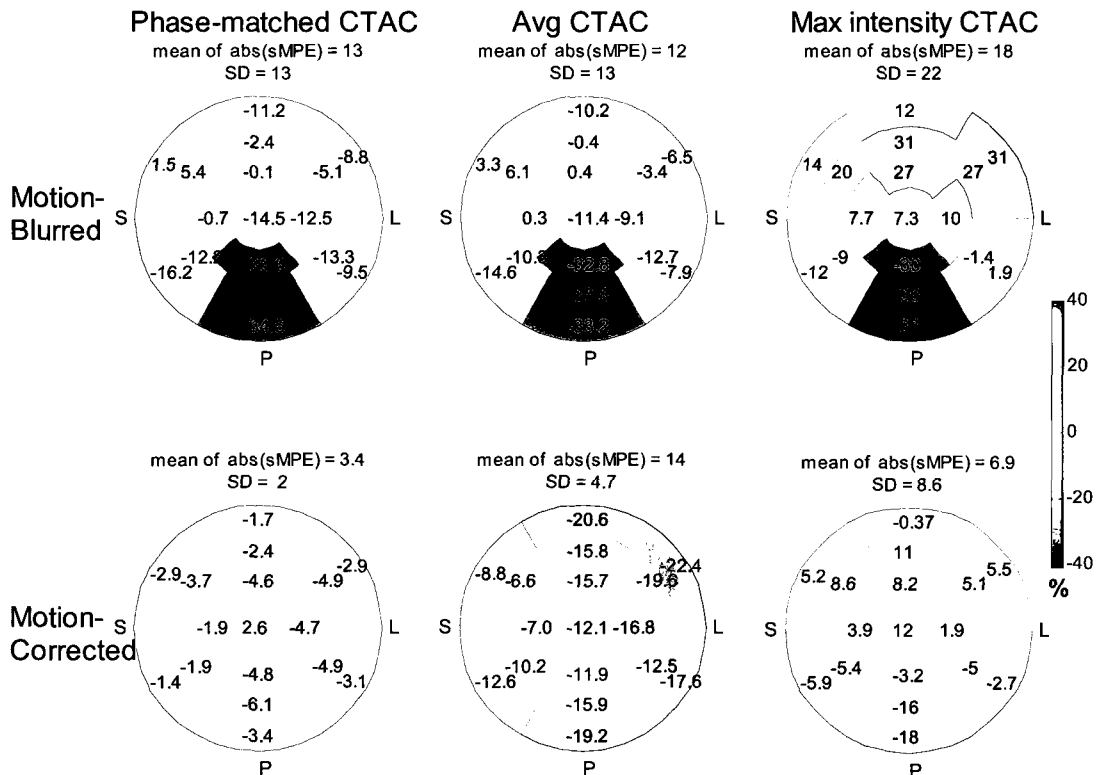


Figure 2.17 Absolute segmental mean percentage errors for the absolute blood flow maps shown in Figure 2.15 relative to the motion-free map

Similar to the uptake polar maps, a paired T-test analysis was done in between the segmental flow values of the “motion-free” polar map, versus the “motion-blurred” and “motion-corrected” polar maps in Figure 2.15 in order to determine significance of differences. No significant differences were seen at the 5% significance level except for the max-intensity CTAC polar maps. However, the p values for the “motion-corrected” phase-matched and averaged CTAC methods were an order of magnitude larger than that for the “motion-blurred” polar maps ($p = 0.400$, $p = 0.529$ vs $p = 0.056$, $p = 0.104$ respectively). This confirms the previous finding with the uptake images that MC is effective in reducing the differences with respect to ‘truth’.

The result of a paired T-test between the motion-corrected and motion-blurred blood flow polar maps show that significant differences were seen at the 5% significance level only in the case of the phase-matched CTAC images. The averaged CTAC ($p = 0.257$) and max-intensity images ($p = 0.554$) did not show significant differences at the 5% significance level after motion-correction.

2.1.6 Discussion

The corrected images show improvement in similarity with the motion-free image. Motion-corrected uptake images show point differences of up to 40% when compared to the motion-blurred data set. These differences occur mostly in the anterior-lateral, inferior-septal and apical regions where most motion-averaging occurs. In all cases, similarity with the motion-free image improves after motion-correction, with the least errors showing in respiratory phase-matched CT attenuation corrected images. The maximum-intensity CTAC images show large errors in relative uptake and blood flow

distributions compared to other AC approaches which are believed to be caused by an over-correction for attenuation.

The motion-blurred flow images show reduced values in the posterior region. This is believed to be caused by spillover of activity from the top of the stomach into the myocardial region. The stomach wall sits very close to the myocardium and strongly takes up ^{82}Rb . Motion of the magnitude simulated in these experiments would blur the activity from the stomach wall into the adjacent myocardial wall. The FlowQuant© software does not currently correct for spill-in from extra-cardiac sources of activity. These errors in the posterior wall are largely resolved after MC.

As shown in Figure 2.11, if no MC is applied, a similar distribution of motion-averaging errors is seen in respiratory phase-matched CTAC images and respiratory averaged CTAC images. This similarity suggests that if no MC is performed, then average-CTAC provides as accurate a correction as phase-matched CTAC. However, the differences between the two corresponding motion-corrected images indicate a need for more accurate AC (*i.e.* phase-matched CTAC) if motion-compensation is used.

It is worth noting that unlike in clinical images where the PET and CT images are manually aligned in order to perform CT based attenuation correction, manual alignment was not required for the simulated images as the NCAT program generates both PET and CT images and the two are always perfectly aligned. This eliminates the chance for misregistration errors in the simulated study.

One limitation of this simulation study was that degrading factors such as scatter or random events were not simulated which led to higher quality of images compared to that of clinical images. This was done in order to examine the underlying effects of

motion and AC without the presence of other potentially complicating factors. Accurate application of scatter and randoms correction would result in the same mean values in the projection data, but noise levels would potentially be higher. In addition, very low noise (high count, approximately 4×10^{10} photons detected per scan) simulations were used, again to clarify the underlying effects of motion and attenuation. However, in clinical images, there is significant noise due to the limited count statistics of ^{82}Rb imaging (approximately 2×10^8 photons detected per scan). The effect of noise on the conclusions of these studies has not been investigated.

Also, the range of motion that was simulated was much emphasized in order to observe the extent of the degrading effects of respiratory motion. In patient studies, the range of motion that has been observed is as high as 16.5mm [90], but typical values are under 1cm, much less than what was simulated. As the amplitude of breathing motion decreases, it is expected that the differences between the different approaches to AC and the impact of motion itself would also diminish. Determining the extent of the effects of motion range or scan duration (noise levels) would require a more comprehensive study.

Finally, we note that in Figure 2.5, there are artifacts at the edge of the lungs. This type of artifact may be caused by an inconsistency in the resolution of the PET and CT data sets [91]. Use of cine CT, particularly the average-CT approach, can introduce blurring into the CT map used for AC. This can lead to different degrees of resolution loss in the AC map depending on the correction approach used. This aspect of the simulation requires additional investigation and careful evaluation.

2.2 Respiratory Motion Correction for Swine Cardiac PET/CT Imaging

To further support the simulation studies, the correction methods described in the previous section were applied to a respiratory gated dynamic ^{82}Rb -PET study of a swine. It is hypothesized that motion compensation in addition to accurate attenuation correction can help improve image homogeneity. Furthermore, we also hypothesize that phase-matched attenuation correction will lead to more accurate correction than other approaches. This section describes the imaging protocol used and results from the correction methods applied to the animal data.

2.2.1 Methods

Cardiac PET/CT imaging of a pig was carried out on a Discovery DRx PET/CT scanner (GE Healthcare). The swine was put under total anesthesia and intubated. Respiration was controlled by a ventilator to ensure a constant respiration rate of 7.5 breaths per minute throughout the duration of the study. The swine was laid in a supine position to mimic human positioning during clinical exams. A 4DCT scan was obtained for the length of 1 breathing cycle (8 seconds, 2.5-mm slices, 10 mA, 120 kVp). The respiratory trigger for gated PET and CT scans was obtained using an RPM device (Varian Medical Systems) which optically tracks the transaxial motion of the chest using an external marker. Immediately after the CT scan, the pig was injected with 500 MBq of ^{82}Rb and a 10-minute respiratory-gated PET scan was obtained in list-mode, which allows for retrospective binning of the data. PET data were acquired in 3D.

List-mode data were exported offline and divided into 8 separate list files using the respiratory gating triggers. Each sub-list corresponds to a dynamic scan for a single

respiratory phase. The sub-lists were loaded back into the scanner console for dynamic rebinning and image reconstruction. For each sub-list, 15 dynamic frames with variable durations were sampled: $9 \times 10\text{s}$, $3 \times 30\text{s}$, $1 \times 60\text{s}$, $1 \times 120\text{s}$, $1 \times 240\text{s}$. This dynamic framing is that which is used clinically and provides adequate sampling to generate time-activity curves (TACs) for kinetic analysis. We note that this division of the acquisition into dynamic frames is slightly different than that used in the simulations. The division in the simulations was based on a different but similar protocol. Both provide sufficient sampling to allow for accurate kinetic analysis of the PET data. Image reconstruction was done using filtered backprojection (FBP) with attenuation correction followed by post-filtering with a 14mm 3D Hanning filter to reduce noise.

Cine CT data were retrospectively binned into 8 respiratory phases using vendor supplied software (Advantage 4D – Respiratory gating on an AWWolumeshare2 workstation, GE medical systems) to match the gating applied to the PET data, and different images were generated for attenuation correction (AC). As in the phantom simulation, AC was done using the following three approaches:

- 1) Respiratory phase-matched CTAC. Each respiratory phase of the emission data was corrected using the CT image from its corresponding respiratory phase. The CT phase images were manually aligned with each PET phase of the PET uptake image using vendor supplied software (ACQC) on the PET console so that the myocardium was aligned in the PET and the CT images. This approach was hypothesized to provide the most accurate AC.

- 2) Respiratory averaged CTAC. Attenuation maps for all respiratory phases of each dynamic frame were averaged over the respiratory cycle. Unfortunately, since

vendor software does not allow manually alignment of the averaged attenuation map to each respiratory phase image, the attenuation map was manually aligned to the average position of the PET phase images. This approach has shown to be effective in minimizing errors in non-gated cardiac PET studies [76].

3) Maximum intensity CTAC. The maximum intensity of every pixel position due to changes in attenuation during the respiratory cycle was calculated. Unfortunately, since vendor software does not allow manually alignment of the maximum intensity attenuation map to each respiratory phase image, the attenuation map was manually aligned to the average position of the PET phase images.. This approach which was proposed by Alessio *et al.* [77] showed better promise than the averaged CTAC in clinical cases.

An non-gated (static) image was also processed. Attenuation correction was done using the CT map at end-expiration aligned to the average (non-gated) PET image, as per the clinical standard at the UOHI. No motion-compensation was done for this image.

Uptake images corresponding to the last 7 minutes of the data were used for the evaluation of motion. Methods described in section 2.1.3 were used to fit the LVs to partial ellipses and translate in 3 dimensions to align the centers of the LVs to a reference frame, similar to the simulated data.

The aligned image volumes were averaged to generate a motion-corrected data set. The images were also averaged without alignment to represent a motion-blurred data-set. In order to generate a motion-free data-set, three respiratory phase image volumes at the exhalation stage of the breathing cycle were averaged (phases 4, 5 and 6 see Figure 2.18). These images were corrected using phase-matched CTAC. The resulting data set

was selected as the reference for comparison as it contains the least amount of motion blurring. This image is labeled “motion-free” in the following figures. The motion-blurred and motion-corrected images were compared to the motion-free image.

Image quantification and polar map generation was done using FlowQuant®, an in-house developed analysis program. The polar maps were segmented using the 17-segment model (see section 1.7) and Mean Percentage Errors from the motion-free image were calculated for each segment (sMPE). The standard deviation of the sMPE values for each polar map was used as a measure of similarity with the motion-free image.

2.2.2 Results

The maximum displacement between respiratory phase PET images was found to be (1.63,0.82,0.63) pixels on x,y and z axes which translates to (5.09,2.56,2.05) mm. The calculated shifts (see Figure 2.18) were applied to all dynamic frames to generate the motion-corrected image.

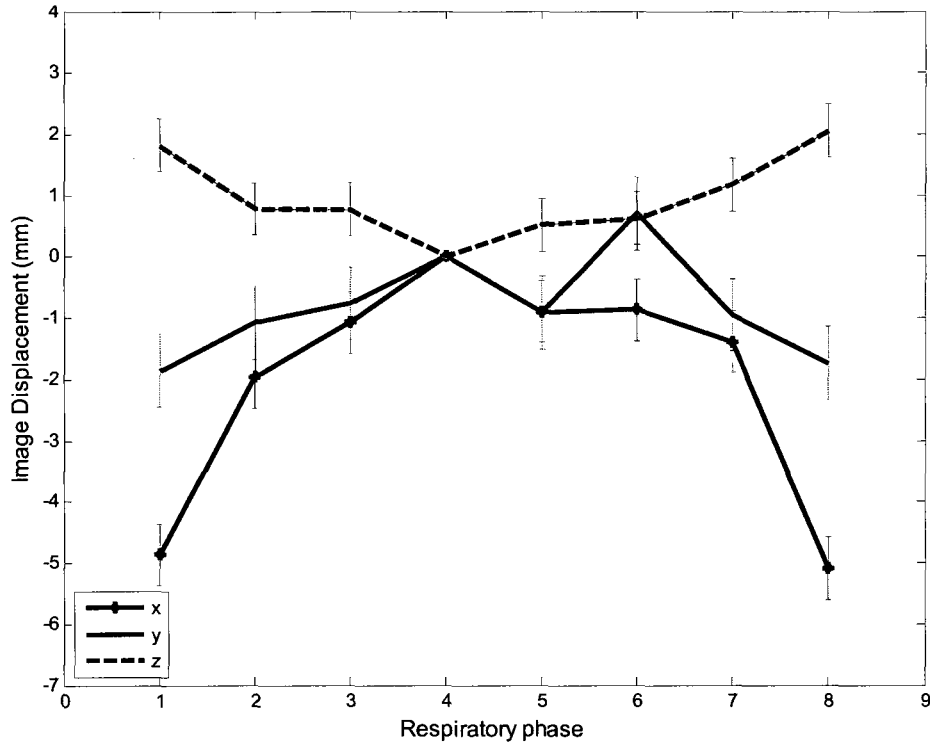


Figure 2.18 Displacements measured from gated PET images on x, y and z axes, using phase #4 as the zero position. Error bars are taken from the pooled standard deviation of results from the phase-alignment accuracy test (section 2.1.4))

As shown in Figure 2.18, most of the breathing motion occurs in four respiratory phases (first and last two) and the heart remains relatively stationary in 50% of the breathing cycle. This can be confirmed by looking at the CT frames over time (not shown). Also, the majority of motion occurs along the x axis, which correlates to the lateral (left-to-right) direction in the pig. The y and z axes correspond to the anterior-posterior (front to back) and cranial-caudal (superior-inferior) directions respectively.

Uptake polar maps are shown in Figure 2.19 and represent the summation of the last 3 dynamic frames. For normally perfused myocardium, the distribution of activity in these polar maps is expected to be completely uniform. However a reduction in activity values is seen at the apex in all polar maps. This is commonly known as *apical thinning* and relates to the fact that the apex is thinner than the outermost parts of the LV, leading to partial volume effects (see section 1.7) and an apparent reduction in uptake [92, 93].

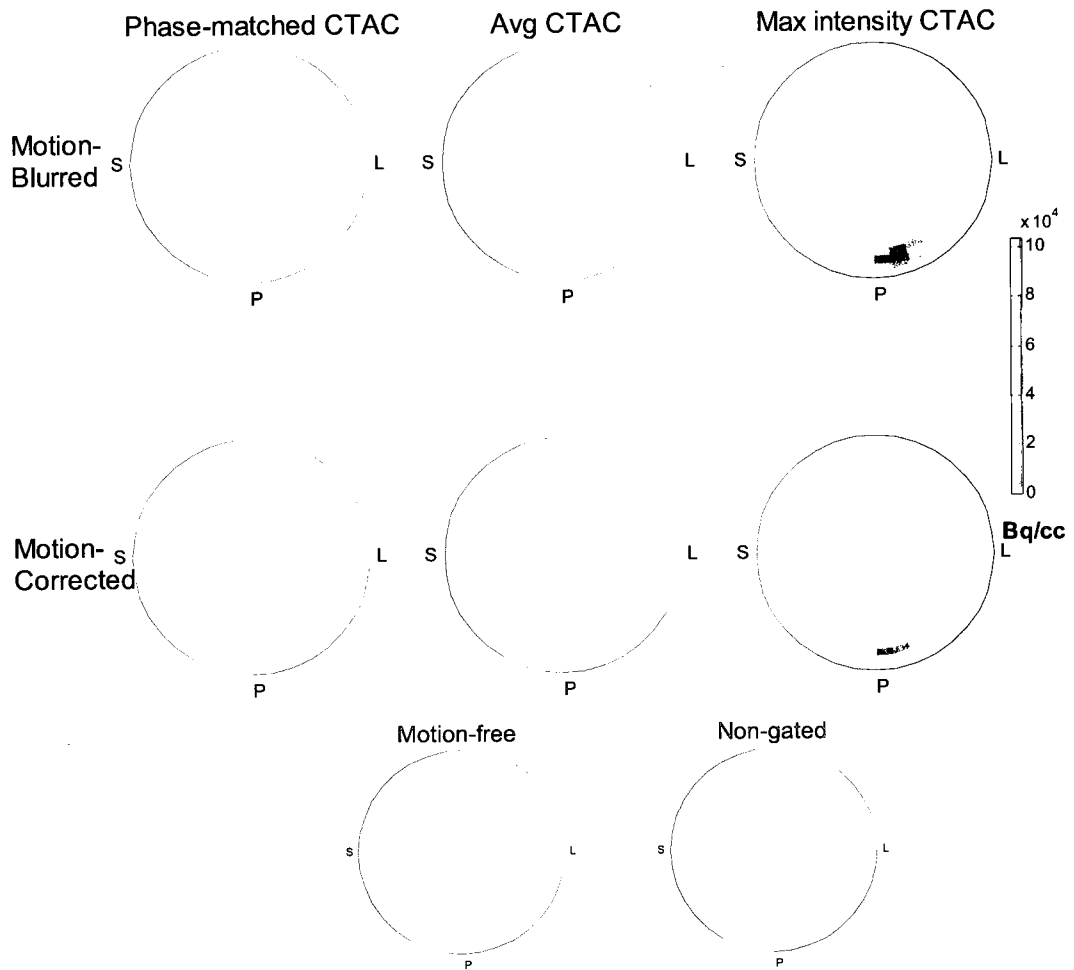


Figure 2.19 Uptake polar maps showing the distribution of activity values in later dynamic frames. A reduction of activity is seen in the apex which is caused by thinner apical thickness of the heart.

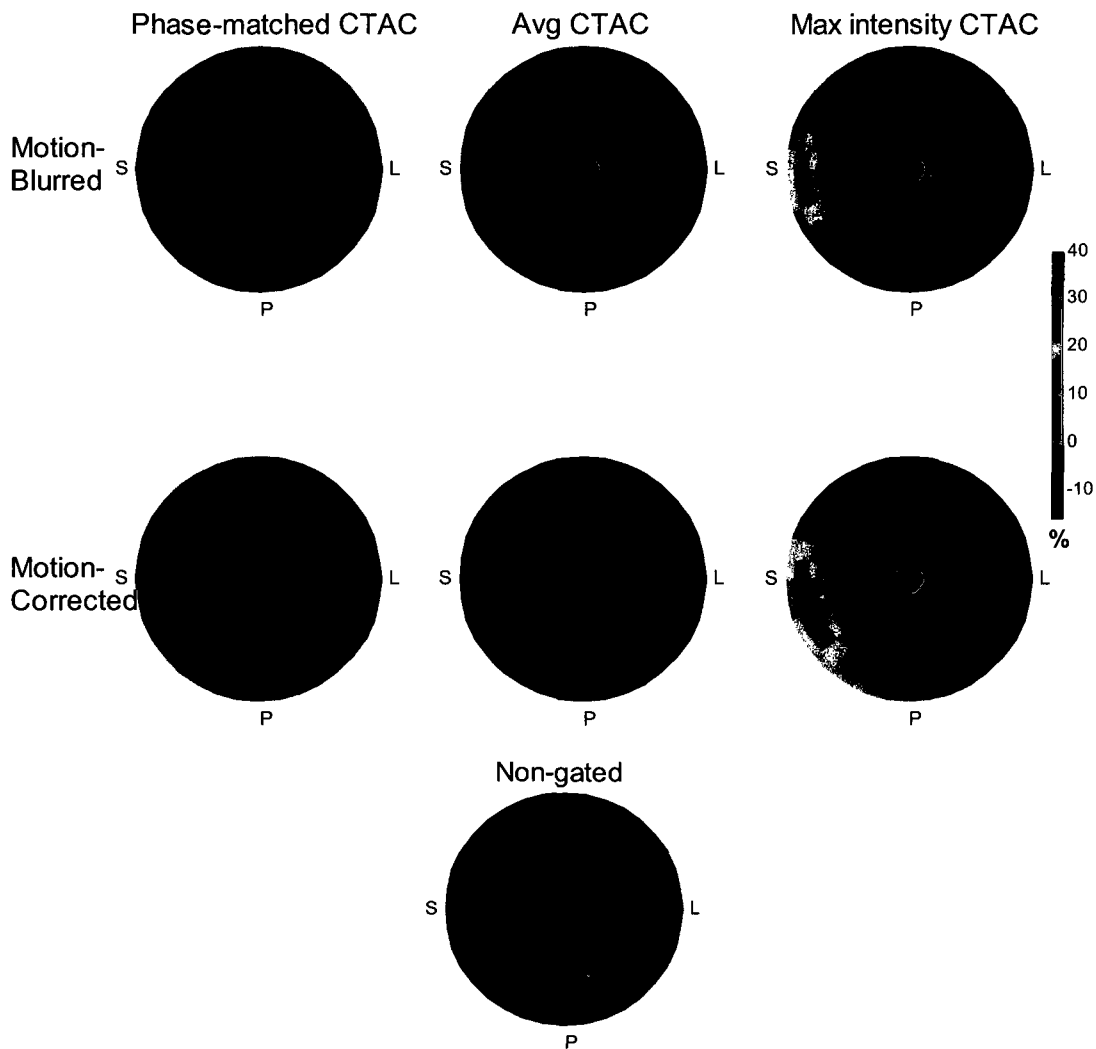


Figure 2.20 Percentage difference polar maps for the uptake polar maps shown in Figure 2.19 compared to the motion-free image.

In order to better visualize the differences due to motion-compensation and AC in Figure 2.19, percent differences were calculated for every pixel and shown in polar map views (Figure 2.20).

The activity levels for images that were corrected using the max-intensity CTAC approach are to be elevated compared to other correction methods (Figure 2.19). This is the result of an over-correction of attenuation, when compared to the motion-free image.

Figure 2.21 shows that this AC method also increases non-uniformity in the polar map as well as the mean error seen across all segments.

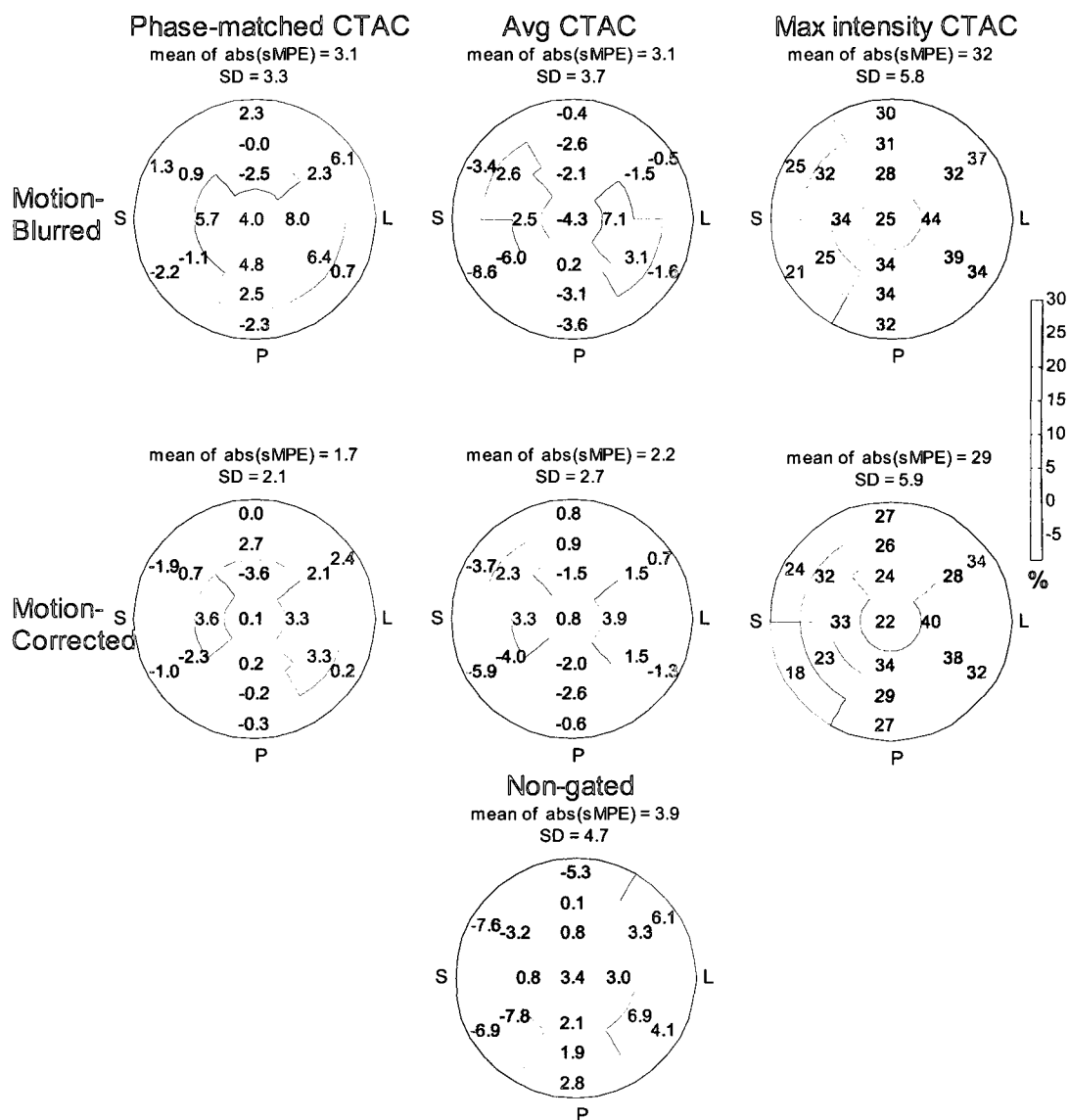


Figure 2.21 Absolute segmental mean percentage errors for the uptake polar maps shown in . Figure 2.19 relative to the motion-free polar map.

The motion-corrected phase-matched CTAC image shows the best image uniformity and the least mean segmental error as was expected. The Avg-CTAC image proves to be as accurate a correction as the phase-matched CTAC image when no motion-correction is applied. This supports the result from the simulated study for uptake images.

As uptake polar maps are usually evaluated on a relative basis in the clinic, the polar maps in Figure 2.19 were segmented according to the 17 segment model and normalized to their maximum segmental value in a similar manner to that done for the simulated data which were shown in Figure 2.13. Figure 2.22 shows these normalized polar maps.

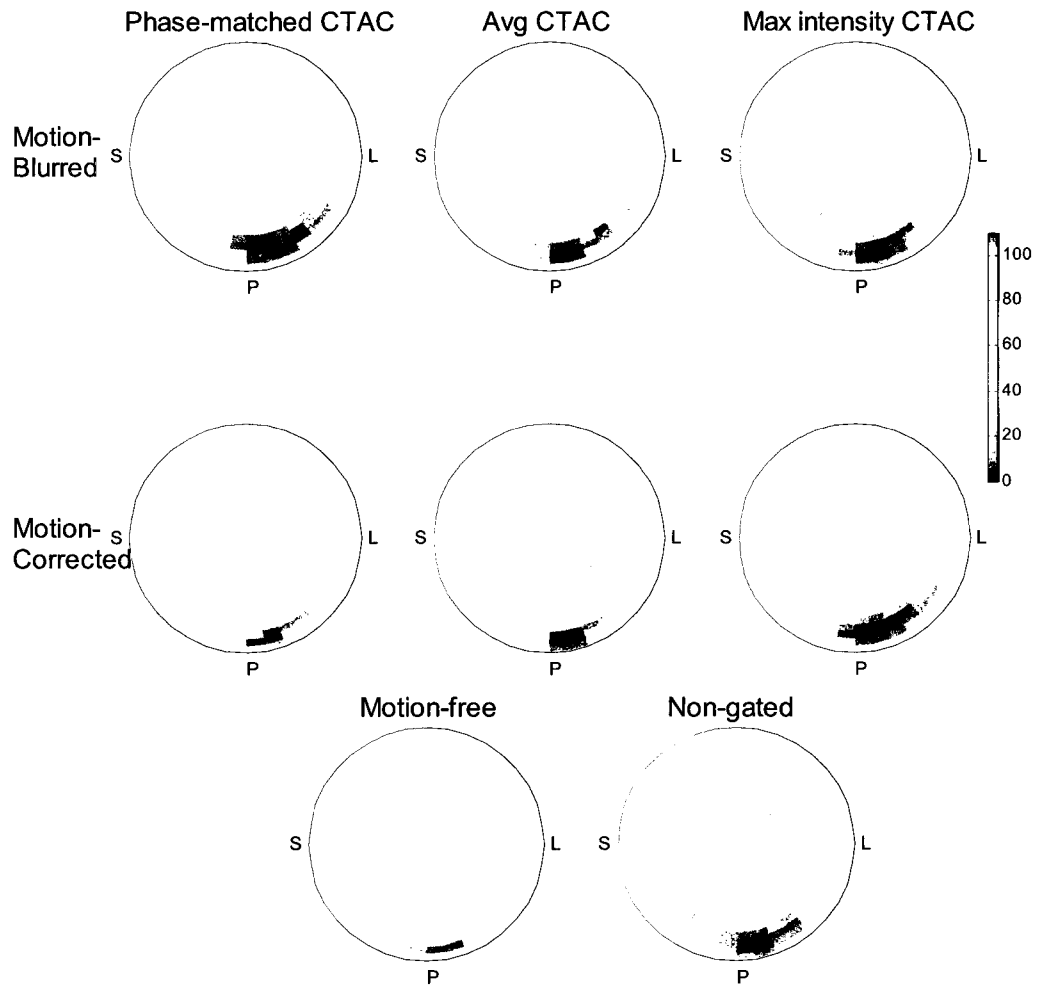


Figure 2.22 Uptake polar maps shown in Figure 2.19 that are normalized to the self-maximum segmental value

The error maps calculated from normalized data demonstrate a better estimation of relative image uniformity since normalization reduces the difference between the mean value in all polar maps and the motion-free map mean value, and are shown in Figure 2.23. Normalization helps reduce the large errors seen in the max-intensity CTAC polar

map previously seen in Figure 2.21. These results support the simulated data which suggested that the large errors seen in the max-intensity CTAC images were mostly due to a large error between its mean value and the mean value of the “motion-free” polar map. However, although MC reduces the difference with the motion-free image, the remaining errors are nevertheless larger compared to those seen for the phase-matched and average CTAC images, which suggests that the max-intensity CTAC does not produce a more accurate correction, even for relative (non-quantitative) images.

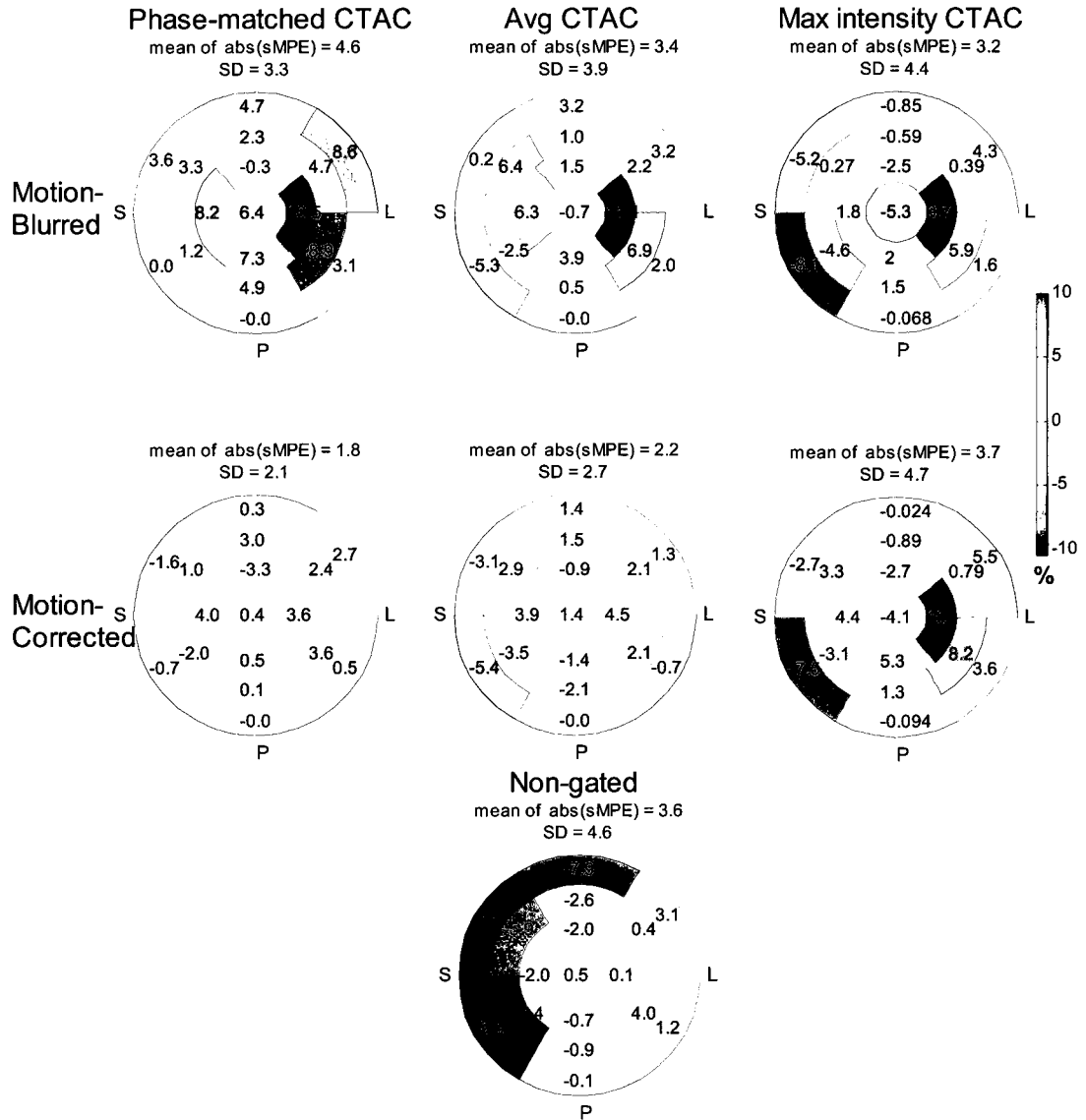


Figure 2.23 Segmental mean percentage error calculation for normalized uptake images, relative to the motion-free polar map shown in Figure 2.22.

In order to determine the significance of differences between the sMPE values in the motion-corrected and motion-blurred polar maps, a paired T-test analysis was done. Differences were significant ($p < 0.05$) only in the phase-matched CTAC images for the uptake polar maps.

Similar analyses have been completed for blood flow values. In Figure 2.24 the blood flow distribution in the LV is shown in units of mL/min/g.

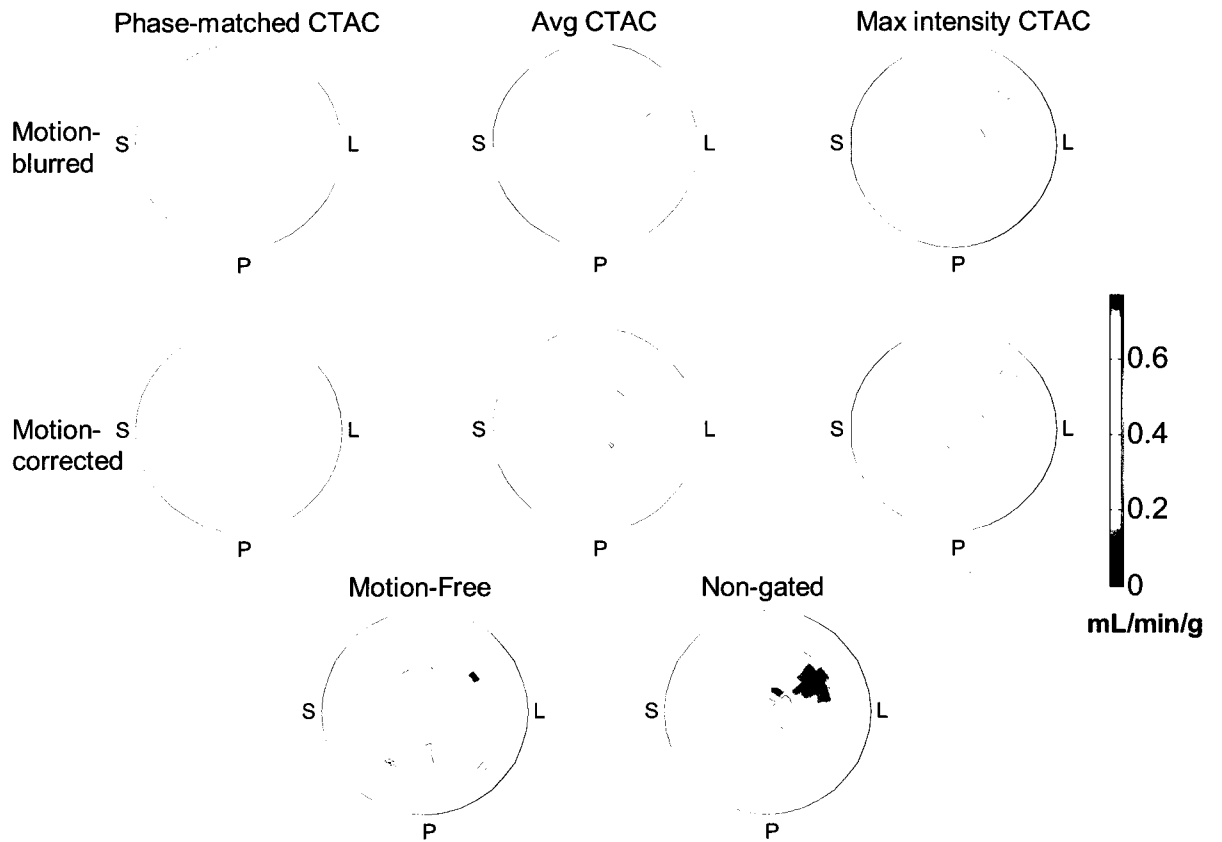


Figure 2.24 Absolute blood-flow polar maps showing image uniformity before and after motion correction.

Figure 2.25 shows difference polar maps relative to the motion-free image in Figure 2.24. The largest error is seen for the non-gated image.

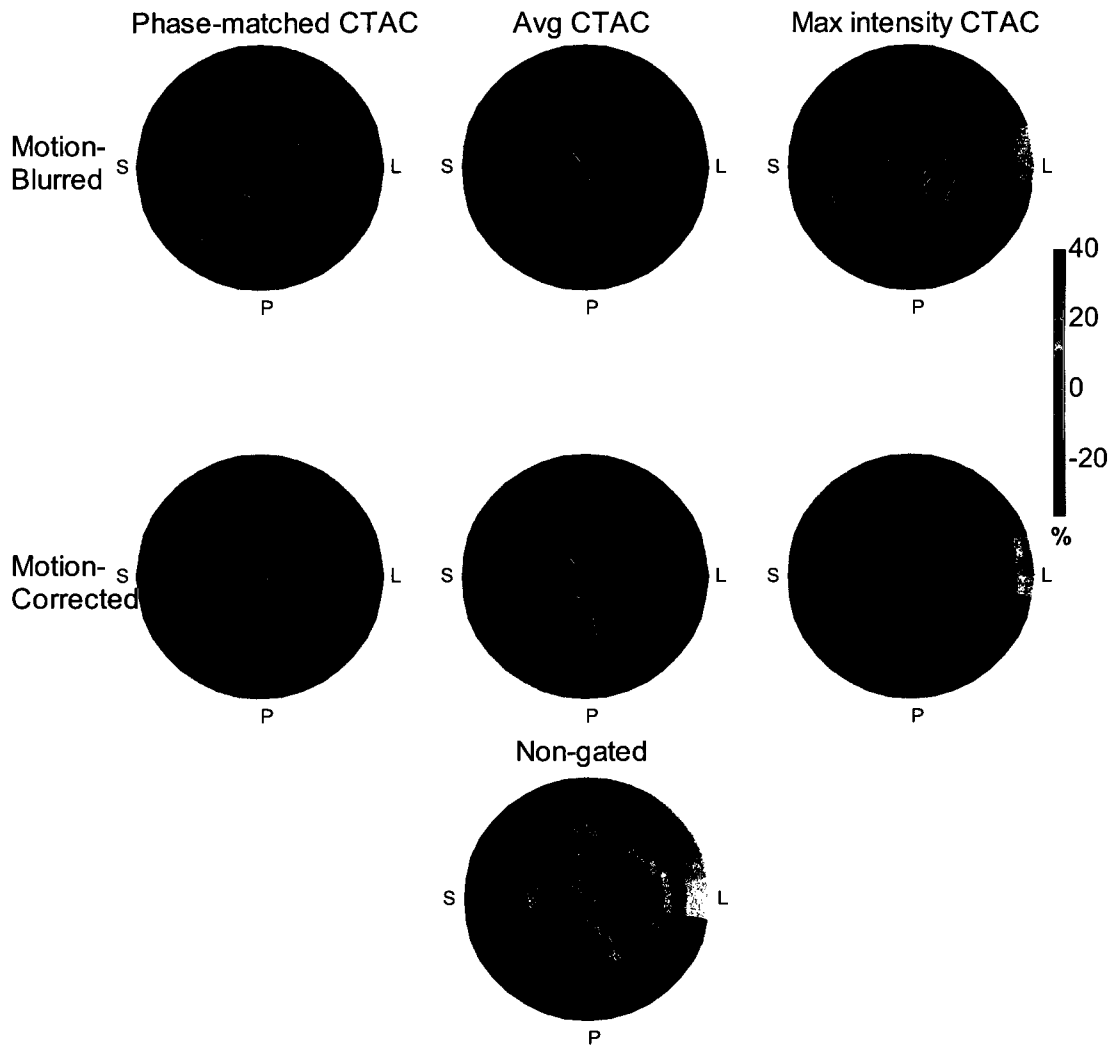


Figure 2.25 Percent difference maps for the absolute blood flow maps shown above in

Figure 2.26 shows the segmental mean percentage error calculation. The similarity with the motion-free image increase in all cases compared to the non-gated image, however the effect of MC between images with different CTAC approaches remains inconclusive as MC does not yield improved results in the case of the average CTAC method. Also, image uniformity does not improve in the case of the phase-matched CTAC image which is different than that seen for the uptake images or for the simulated data.

In the case of the blood flow polar maps, the T-test analysis did not show significant differences after MC at the 5% significance level.

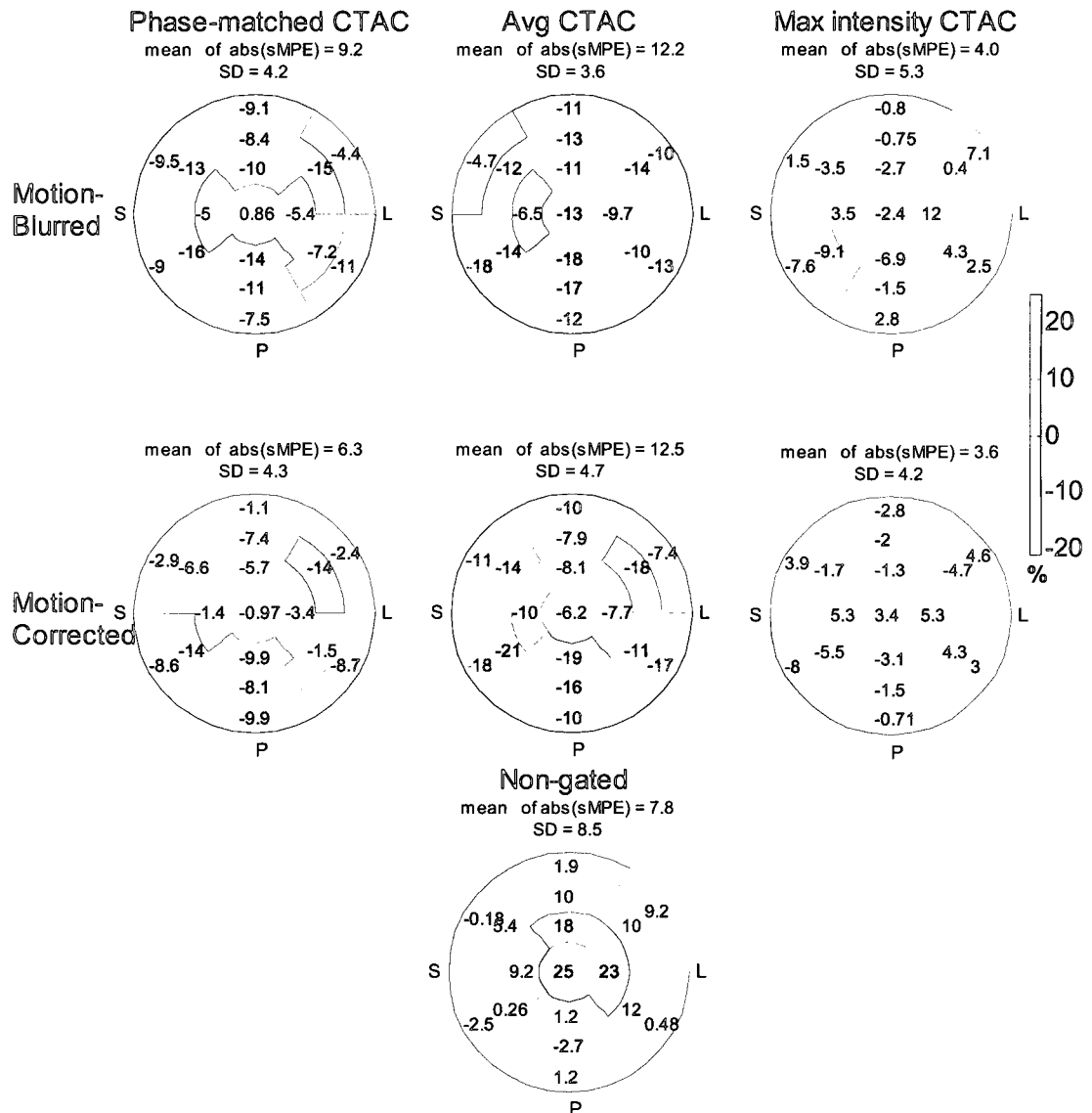


Figure 2.26 segmental mean percentage errors for the absolute blood flow maps shown in Figure 4.5 relative to the motion-free map

2.2.3 Discussion

One limitation of this technique is the elevated level of noise introduced when selecting a limited number of respiratory phase images to represent the motion-free

image. This can lead to in-homogeneities in this image which is used as the gold standard for comparison. 4D reconstruction algorithms should be investigated in order to limit the noise level in individual respiratory gates [94, 95]. Also, the high noise level reduced the accuracy of the fitting algorithms and so the fitting was repeated a number of times, and the average of the calculated motion vectors were used to provide a more accurate localization of the LV in the gated images and ultimately a better phase-alignment.

The analysis described in this chapter operates on the assumption that the extent of breathing motion during image acquisition remains constant, so that estimation of motion using the later dynamic frames can be used for motion compensation in earlier dynamic frames. The later dynamic frames are used for motion estimation since the LV is highly distinguishable and provides for more accurate estimation of location than the earlier frames. Although this can be assured - to some extent - while using a ventilator in animal scans, potential for error exists when this technique is applied to patient studies. Clinical studies would be needed to assess the prevalence and impact of changes in motion during the acquisition and, if found to be significant, more complete motion estimation techniques may need to be developed that could be applied on a frame-by-frame basis.

In this animal study, efforts were made in order to generate a relatively large breathing motion of the myocardium. However, the maximum range of motion measured in the swine only 5 mm which is rather moderate compared to that seen in patients, which can be as large as 1.5-2 cm cranial-caudally. Figure 2.18 shows that for the pig, the majority of motion occurs along the septal-lateral direction in the pig, different than that seen in humans which occurs cranial-caudally. Also configuration of the heart in the

animal is different than the configuration of the heart in humans. These factors can affect the magnitude and pattern of errors and create differences from what was simulated for humans in section 2.1, in which most motion occurred along the z axis. However, although the specifics of the animal results may differ from those of the simulation, the general conclusions are consistent between the two.

Also, Figure 2.18 shows that the breathing curve is distributed rather evenly between inspiration and exhalation. Human breathing patterns are very variable. A significant change in the breathing pattern might lead to more or less emphasis of certain phases of the respiratory cycle in the averaged image and a different distribution of motion averaging of the PET data. The effect of variations in the breathing pattern has not been evaluated in this study and is a potential avenue of future investigations.

An additional potential for error lies within manual registration of the CT to the PET data. In the case of respiratory phase-matched AC, manual registration was repeated for each of the 8 respiratory phases. Inaccuracies here could lead to mis-registration errors and could further complicate the correction process. Automated methods of CT-PET alignment are being developed by others [53] and use of these approaches should reduce possible errors and would also greatly facilitate implementation of our technique.

Although all corrected images show improvements over the non-gated images, the results from this chapter show that the optimal correction approach is different between uptake and flow images. Despite the smaller range of motion and other differences mentioned between the simulated and pig study, the results of the simulation study are supported by the pig study for the uptake images. The conclusions in both cases are that the phase-matched CTAC method which is the most complicated AC approach, yields the

best results among other approaches which improve after MC. However, the analysis with respect to blood flow is inconclusive. The differences between our simulations and the pig study may be attributed to the complicating factors stated above but further studies would be required to confirm this.

In conclusion, the motion compensation and attenuation correction techniques illustrated in this chapter show feasibility in live-subject imaging scenarios. A more extensive analysis is needed to verify application to clinical studies.

Chapter 3 Improved measurement of Defect Size and Severity using Respiratory Motion Compensation in Cardiac PET/CT

As discussed in previous chapters, respiratory induced motion of the myocardium has been shown to degrade image quality by blurring the acquired counts along the path of movement. We hypothesize that motion compensation (MC) would help increase the accuracy of the size and contrast of defects (myocardial regions of reduced activity indicative of reduced perfusion) by reducing the errors introduced by motion blurring in the uptake images. In Chapter 2, a method was introduced for automated realignment of gated emission image volumes, and its effect in improving image characteristics for normal studies was evaluated. In this chapter, we have extended this work to evaluate the impact of respiratory-motion correction on abnormal studies.

3.1 Methods

Simulation studies were conducted using the nonuniform rational b-splines (NURBS)-based cardiac torso phantom (NCAT) [85]. Activity and anatomical settings were identical to that of the study discussed in Chapter 2. Two phantoms were generated, one with a 50 mm and the other with a 30 mm lesion in the lateral wall of the left ventricle. The angular extent was 60° for both lesions. In order to simulate the lesions,

phantom activity values were separately set to zero at the location of the lesion. Orthogonal views of the phantoms are shown in Figure 3.1.

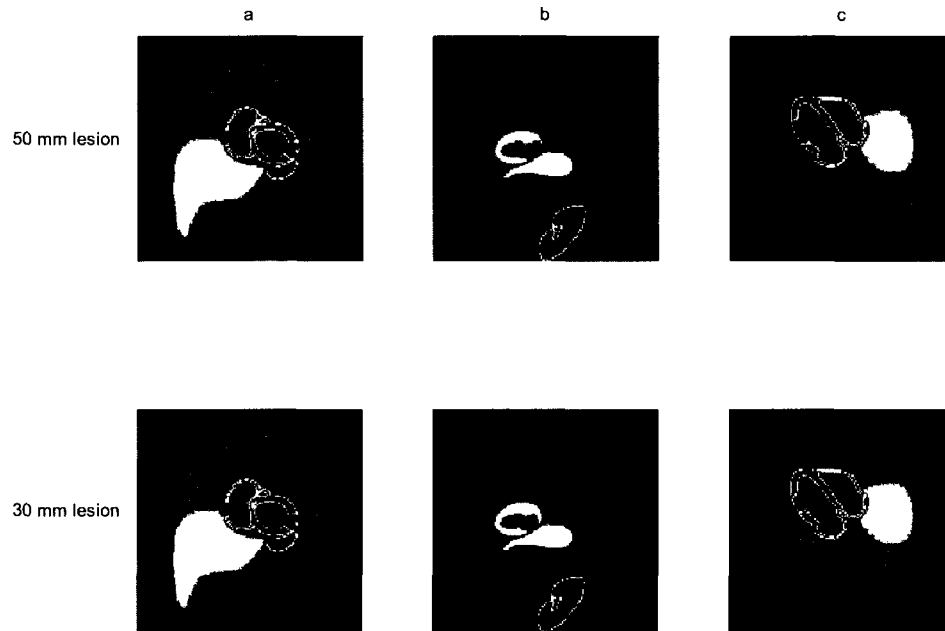


Figure 3.1 Orthogonal views of the heart showing (a) coronal, (b) sagittal and (c) transaxial views for phantoms with a 50 mm lesion (first row) and 30 mm lesion (second row) in the lateral wall of the left ventricle.

The activity and attenuation map images were used as input to SimSet in order to simulate a static ^{82}Rb -PET acquisition. The same number of photons (400 million) were generated leading again to low-noise data sets. Images were reconstructed using OSEM in the same manner as described in Chapter 2, however only the uptake images were used for this evaluation. Respiratory phase-matched AC was done in order to focus on the effect of motion blurring.

Image quantification and polar map generation were done using FlowQuant® software. Registration of respiratory phase images was done using the methods described in Chapter 2. The registered image volumes were averaged to represent the motion-corrected data set. Attenuation corrected respiratory phase images were averaged without registration to represent the motion-blurred data set. A single-phase PET image (end-

expiration) was selected as the standard for comparison as it contains no motion blurring. This image is labeled “motion-free” in the following figures. The motion-blurred and motion-corrected images were compared to this motion-free image in order to evaluate the improvement in defect size and severity.

The area of the perfusion defect was determined by the number of pixels in the polar map below a cutoff value of 70% of the normal wall uptake, in segments containing the defect. This is normalized by the number of pixels in the polar-map.

Mean Percentage Errors from the motion-free image were calculated for each segment (sMPE) using the standard 17-segment division of the heart (see section 1.7). The standard deviation of the sMPE for each polar map was used as a measure of variability compared to the “motion-free” image.

Segmenting the uptake data allowed for scoring of the polar maps similar to what is used for clinical evaluation in research studies at the UOHI. To determine the severity of the state of the disease in the image, each segment is scored based on comparison with the segment with maximum uptake (assumed to be normal heart tissue): score=0 for segments > 70% max, score=1 for 60-69%, score=2 for 50-59%, score=3 for 40-49%, and score=4 for <40%. The sum of the scores for each polar map is calculated and is referred to as the summed perfusion score (SPS). SPS is then rated: normal for SPS=0-3, mild for SPS=4-8, moderate for SPS=9-12 and severe for SPS=13-17.

To assess the feasibility of applying the developed method to clinical scans, the motion correction algorithm was retrospectively applied to a patient’s respiratory-gated static ⁸²Rb cardiac perfusion scan. The patient data were acquired in list-mode according to the UOHI clinical protocol using a Discovery Rx PET/CT scanner (GE Healthcare).

The patient study contained a visible area of reduced perfusion to allow for assessment of defect size and severity. The static scan is comparable to the uptake images from the simulation study. Measures of absolute flow quantification were not possible with this data set as the list-mode data were no longer available for reprocessing. Assessment of the feasibility of these methods for flow imaging was discussed in section 2.2. PET data were retrospectively binned into 8 respiratory phases using an acceptance window of 15 breaths per minute \pm 50%, corresponding to a range in the respiratory period of 2-6sec. . The respiratory trigger was obtained using a real-time patient monitoring (RPM) device (Varian Medical Systems) which optically tracks the transaxial motion of the chest using an external marker. Attenuation correction was done using a single fast CT acquisition, obtained near full expiration following the PET acquisition. The CT was manually aligned to the non-gated image. Image reconstruction was done using filtered backprojection (FBP) followed by a 14mm Hann filter. FBP was chosen for these images as this is the algorithm used for clinical evaluation. Evaluation of the effects of motion correction on the patient data set was done in the same manner as for the simulation studies. The ‘motion-free’ image for the patient data is again the end-expiration phase as this is the phase near which the CT image was acquired and should be accurately corrected for attenuation. End-expiration is also a period in the respiratory cycle during which there is minimal motion.

3.2 Results

Polar map comparisons for the simulation studies are shown in Figure 3.2 and Figure 3.3. The corrected images show improvement in defect size and contrast. Motion-corrected images show point differences of up to 40% when compared to the motion-

blurred data set. These differences occur mostly in the anterior-lateral, inferior-septal and apical regions for the simulation studies where most of the motion-averaging occurs.

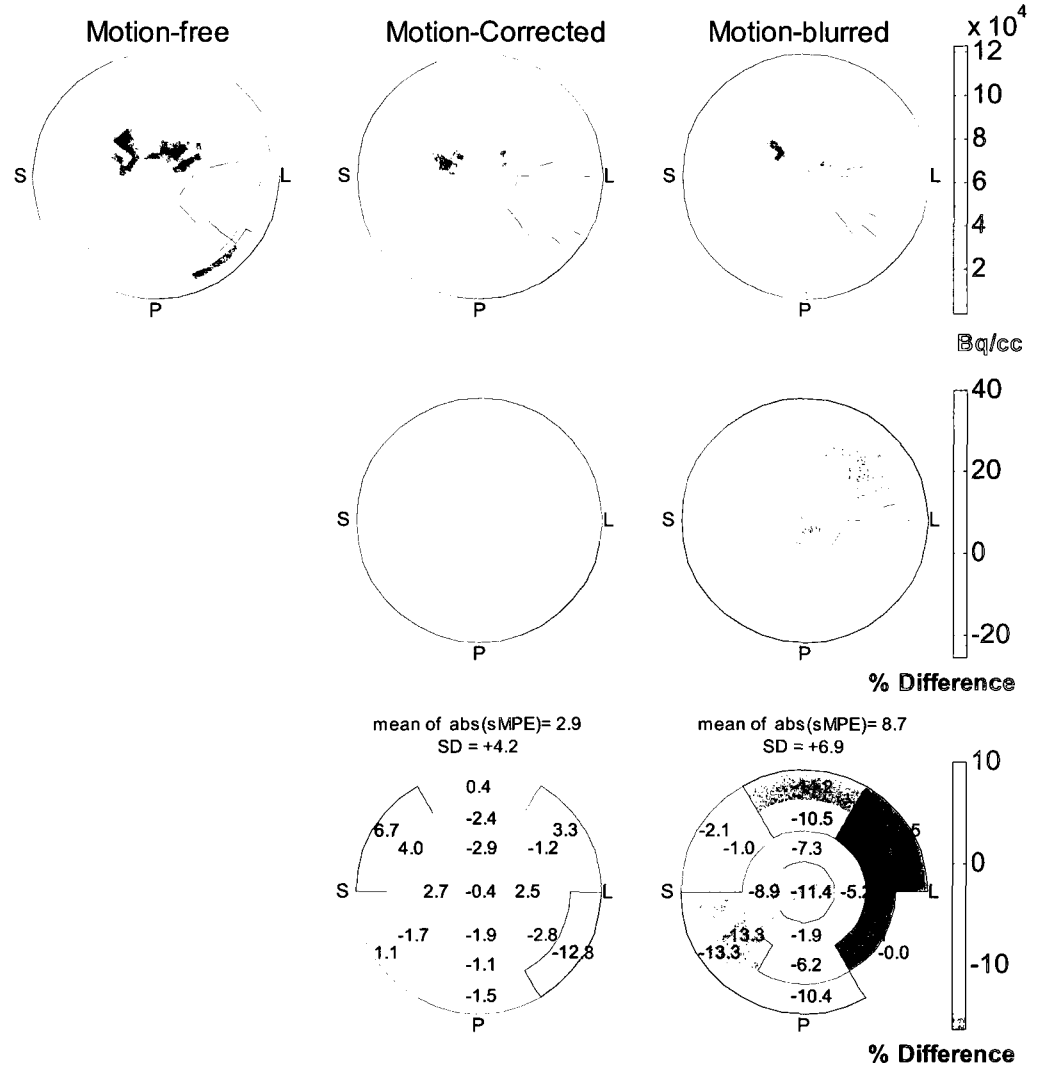


Figure 3.2 First row: uptake polar maps shown for the large simulated defect. Second row: Percentage difference polar maps for the polar maps shown in the first row compared to the motion-free image. Third row: Segmental mean percentage errors for the motion-corrected and motion blurred polar map compared to the motion-free polar map in the first row.

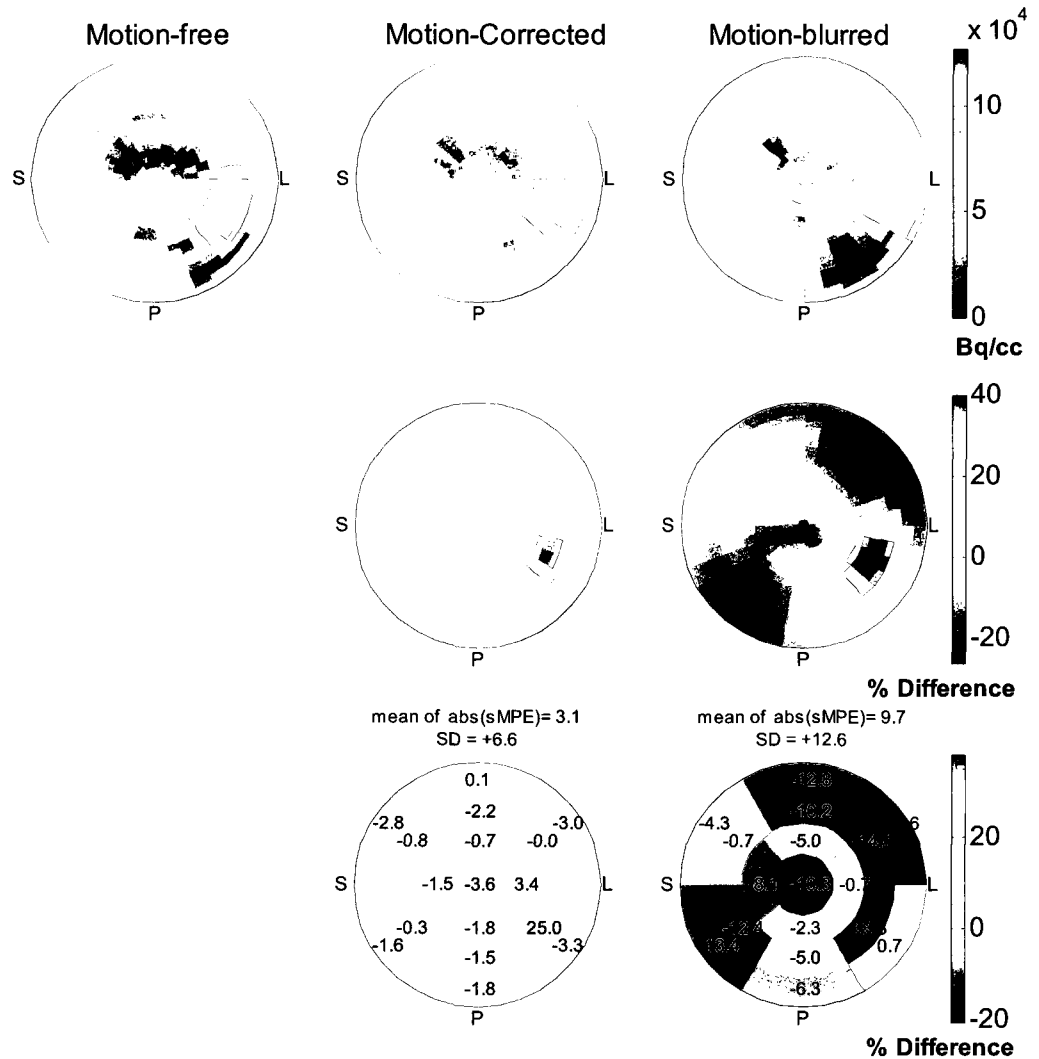


Figure 3.3 Polar map comparisons, similar to Figure 3.2, for the small simulated defect. First row: uptake polar maps shown for the small simulated defect. Second row: Percentage difference polar maps for the polar maps shown in the first row compared to the motion-free image. Third row: Segmental mean percentage errors for the motion-corrected and motion blurred polar map compared to the motion-free polar map in the first row.

Motion compensation improves the variability of the image compared to ‘truth’ by 2.7% for the image with the large simulated defect and by 6.0% for the small simulated defect. Motion compensation also improved the mean segmental error across all segments by 5.8% and 6.6% for the large and small defects respectively.

Polar map comparisons for the patient study is shown in Figure 3.4. The maximum displacement between respiratory phases for the patient scan was found to be

5.6, 2.1 and 10.1 mm on the x, y and z axes respectively. SPS was calculated to be “6”, “6” and “4” for the motion-free, motion corrected and motion blurred images, respectively.

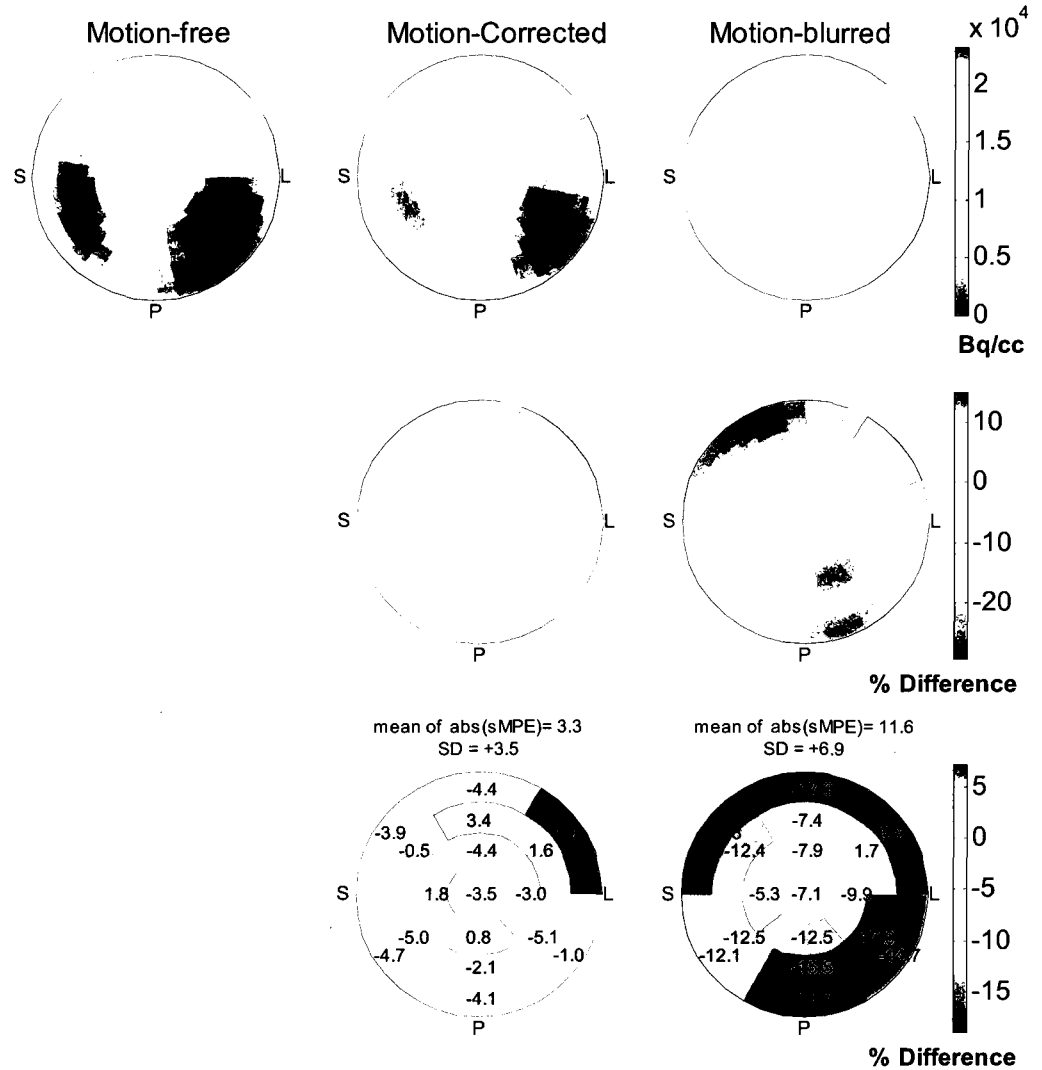


Figure 3.4 Polar map comparisons for the patient study. First row: uptake polar maps. Second row: Percentage difference polar maps for the polar maps shown in the first row compared to the motion-free image. Third row: Absolute segmental mean percentage errors for the motion-corrected and motion blurred polar map compared to the motion-free polar map in the first row.

The change in defect size was approximately 12% for the large defect and 17% for the small simulated defect, when compared to the motion-free image for each image.

The summary of SPS and defect size calculations are shown in Table 3.1 and Table 3.2.

As with the simulation study, the mean error and the variability with ‘truth’ improved in the patient images by 8.3% and 3.4% respectively. A summary of the SPS calculations and defect size changes after motion-compensation is shown below.

Table 3.1 Summed Perfusion Scores (SPS) for the clinical and simulated studies before and after motion-correction

	Motion-Blurred	Motion-Corrected	Motion-Free
Large simulated defect	3	5	5
Small simulated defect	2	2	2
Clinical image	4	6	6

Table 3.2 Defect size difference as a percentage of the motion-free defect size, before and after motion-correction.

	Motion-Blurred	Motion-Corrected
Large simulated defect	16.1%	4.3%
Small simulated defect	41.3%	24.1%
Clinical image	22.3%	5.7%

As seen in the table above, the difference with respect to the defect size in the motion-free image decreases after MC, by approximately 12% in the case of the large defect and by 17% for the small defect. Due to limited spatial resolution of PET scanners, it is difficult to visualize smaller defect sizes therefore a relatively large error (24%) in the small defect remains even after MC.

In order to determine the significance of differences between the sMPE values in the motion-corrected and motion-blurred polar maps, a paired T-test analysis was done. Differences were significant in all cases ($p < 0.001$).

3.3 Discussion

The SPS increases by 2 after motion correction in all cases except for the case with the small lesion size. SPS can represent the severity of disease, typically 0-3 is normal, 4-8 is mild, 9-12 is moderate and >12 is severe. A change of 2 thus represents a

shift of half of the width of a disease category and has the potential to alter the degree of disease assessed and thereby potentially alter patient management.

Unfortunately, 4DCT is not currently acquired as part of the clinical scanning protocol at the UOHI. Therefore, the effect of more sophisticated attenuation correction methods is yet to be directly explored. These simulation studies focused on the best possible method of AC, that of phase-matched AC. The degree to which a simpler approach to AC would degrade the benefits of motion-compensation has not been explored. By necessity, the clinical study used a simpler form of AC and thus may under-represent the potential for improvement in real scans. Other studies have shown that more accurate AC leads to improvements in image quality [43, 74, 76]. As well, our work with simulation studies in normal (homogeneous) hearts suggests that more accurate AC such as phase-matched attenuation correction will provide better results than the simple AC approach used for the clinical data in this chapter. Additional improvements in clinical imaging are, therefore, likely possible and merit further investigation.

A potential for error exists when estimating the ‘truth’ image in the patient study. In order to perform AC, the CT image was matched to the non-gated PET image rather than the end-expiration phase, as the clinical protocols currently in place do not take use of the gated data for PET-CT alignment. This can cause a discrepancy in the ‘truth’ values due to the possible mis-alignment of the PET and CT images.

Motion compensation was shown to increase the accuracy of the size and contrast of defects. The automated method of compensating for motion between respiratory phases is feasible for use on clinical images and shows promise for improving the quality of clinical cardiac PET images. However, a more comprehensive clinical study is

required to assess its true performance in a clinical setting on a broader range of patient data sets.

Chapter 4 Conclusions

The objective of this work was to develop correction methods to reduce image artifacts caused by respiratory motion in respiratory-gated ^{82}Rb -PET images. In order to accomplish this, fitting algorithms were used to localize and align the myocardium in respiratory-gated PET images in order to reduce the amount of motion blurring. Evaluation of the performance of these algorithms showed that the location of the center of the myocardium can be identified to a precision of (0.50, 0.60, 0.43) pixels on x , y and z axes in noise-free images. The application of these algorithms on low noise images, such as the simulated images, showed promising results. However, in the case of the animal study or the clinical images in Chapter 3, the fitting was repeated a number of times, and the mean of displacement vectors were used to provide a more accurate localization and ultimately a better phase-alignment.

In order to evaluate the effect of the correction methods, many experiments were carried-out. Simulated PET images were used to generate respiratory motion blurring effects in a controlled environment. In order to validate the simulation results in the case of a live-subject imaging scenario, the correction methods were applied to respiratory-gated ^{82}Rb -PET dynamic data set.

For uptake images, motion correction consistently provided better results than the non-corrected images. The degree of improvement was approximately 5% of the mean

error across all segmental values in the simulated and animal studies. In the case of images without MC, a similar distribution of motion-blurring errors was seen in respiratory phase-matched CTAC images and respiratory averaged CTAC images. This similarity suggests that the average-CTAC provides as accurate a correction as phase-matched CTAC, if no MC is performed. However, if motion-compensation is used, the differences between the two corresponding motion-corrected images indicate that a more accurate AC could lead to improved image accuracy (*i.e.* phase-matched CTAC).

Automated phase-alignment of the PET images for motion compensation can reduce respiratory-induced errors in the estimating perfusion-defect size and severity. The change of “2” in the summed perfusion score represents a shift of half of the width of a disease category and can potentially change the prognosis of the disease. The methods developed using simulated data show feasibility for application on clinical studies.

An improvement of approximately 5% in the accuracy of myocardial blood flow quantification may not have immediate clinical implications. On the same note however, this is not as trivial since it is comparable to the repeatability accuracy in serial ^{82}Rb MBF measurements. Recent studies show the average per sector repeatability coefficients for the calculations of MBF values is 8.5% [96] or have a mean difference of 6.18% between MBF measurements [97]. An improvement on this scale can help reduce this variability and secure the position of PET as the gold standard for measuring MBF.

In this work, only respiratory motion with large amplitudes were simulated. The magnitude of errors shown are not as severe for all patients, but rather the subset of patients with ‘large’ respiratory amplitudes. Studies show a prevalence of 7.5% for patients having a displacement between expiration and inspiration of $\geq 8\text{mm}$ [98], or

similar [68, 69]. Although this does not concern the majority of patients, however the number of patients involved is not trivial and could benefit from the increased accuracy.

The work completed in this thesis shows great promise for improving the quality of cardiac PET perfusion imaging but also suggests many potential directions for further improvements. Possible future work involves the incorporation of cardiac gating in order to reduce the motion blurring due to the contractile motion of the heart. It has been suggested by others [99] that correction of both respiratory and cardiac motion leads to improved image quality for FDG PET cardiac imaging. Extension of the developed method to include compensation for cardiac contraction is hypothesized to provide a similar level of improvement for ^{82}Rb imaging. This extension is not without challenges, however, as further division of the data through cardiac gating will greatly increase the noise in the individual images. 4D reconstruction techniques can provide lower noise levels that may compensate for the increase in noise caused by a second dimension of gating. 4D techniques may also reduce noise when using a subset of the data as the motion-free standard for comparison. More sophisticated simulations could provide a better representation of the magnitude of the effects of motion and using human datasets in the validation study would reveal clinical implications more easily. Data-driven gating techniques can be used which eliminate the need for external markers and reduce the amount of processing in order to calculate spatial shifts between the gated data. Automated techniques should be pursued for alignment of the CT to the PET images for AC in order to reduce the chance for misregistration errors.

The results presented in this thesis show that respiratory motion compensation holds great potential for improving the accuracy of myocardial perfusion imaging with

PET. The automated method developed herein has achieved success with simulated studies and is feasible for application to clinical studies. Incorporation of this method has the potential to further reinforce PET's position as the gold standard of myocardial perfusion measurement.

References

- [1] Koepfli P, Hany TF, Wyss CA, Namdar M, Burger C, Konstantinidis AV, et al. CT attenuation correction for myocardial perfusion quantification using a PET/CT hybrid scanner. *J Nucl Med* 2004;45:537-42.
- [2] Cackette MR, Ruth TJ, and Vincent JS. ^{82}Sr Production From Metallic Rb Targets and Development of an ^{82}Rb Generator System. 1993;44:917-22.
- [3] Klein R, Adler A, Beanlands RS, and deKemp RA. Precision control of eluted activity from a Sr/Rb generator for cardiac positron emission tomography. *Conf Proc IEEE Eng Med Biol Soc* 2004;2:1393-6.
- [4] deKemp RA, Yoshinaga K, and Beanlands RS. Will 3-dimensional PET-CT enable the routine quantification of myocardial blood flow? *J Nucl Cardiol* 2007;14:380-97.
- [5] Dawood M, Buther F, Stegger L, Jiang X, Schober O, Schafers M, et al. Optimal number of respiratory gates in positron emission tomography: a cardiac patient study. *Med Phys* 2009;36:1775-84.
- [6] Wahl RL and Wagner HN. Principles and practice of PET and PET/CT. 2nd ed., Philadelphia: Lippincott Williams & Wilkins,2009.
- [7] Phelps ME. PET : molecular imaging and its biological applications, New York: Springer,2004.
- [8] Orlov S. Theory of three-dimensional reconstruction. 1. Conditions of a complete set of projections. *Sov Phys Crystallogr* 1976;20:312.

- [9] Defrise M, Townsend DW, and Clack R. Three-dimensional image reconstruction from complete projections. *Phys Med Biol* 1989;34:573-87.
- [10] Cherry SR, Dahlbom M, and Hoffman EJ. 3D PET using a conventional multislice tomograph without septa. *J Comput Assist Tomogr* 1991;15:655-68.
- [11] Townsend DW, Geissbuhler A, Defrise M, Hoffman EJ, Spinks TJ, Bailey DL, et al. Fully three-dimensional reconstruction for a PET camera with retractable septa. *IEEE Trans Med Imaging* 1991;10:505-12.
- [12] Knesaurek K, Machac J, and Ho Kim J. Comparison of 2D, 3D high dose and 3D low dose gated myocardial ^{82}Rb PET imaging. *BMC Nucl Med* 2007;7:4.
- [13] Bailey DL. *Positron Emission Tomography : Basic Sciences*, New York: Springer,2005.
- [14] Germano G and Hoffman EJ. Investigation of count rate and deadtime characteristics of a high resolution PET system. *J Comput Assist Tomogr* 1988;12:836-46.
- [15] Eriksson L, Wienhard K, and Dahlbom M. A simple data loss model for positron camera systems. *Nuclear Science, IEEE Transactions on* 1994;41:1566-70.
- [16] Hoffman EJ, Guerrero TM, Germano G, Digby WM, and Dahlbom M. PET system calibrations and corrections for quantitative and spatially accurate images. *IEEE Trans on Nucl Sci* 1989;36:1108-12.
- [17] Johns HE and Cunningham JR. *The Physics of Radiology*. 4th ed., Springfield, Ill., U.S.A.: Charles C. Thomas,1983.

- [18] Humm JL, Rosenfeld A, and Del Guerra A. From PET detectors to PET scanners. *Eur J Nucl Med Mol Imaging* 2003;30:1574-97.
- [19] Kemp BJ, Kim C, Williams JJ, Ganin A, and Lowe VJ. NEMA NU 2-2001 performance measurements of an LYSO-based PET/CT system in 2D and 3D acquisition modes. *J Nucl Med* 2006;47:1960-7.
- [20] Ollinger JM. Model-based scatter correction for fully 3D PET. *Physics in Medicine and Biology* 1996;41:153-76.
- [21] Grootenk S, Spinks TJ, Sashin D, Spyrou NM, and Jones T. Correction for scatter in 3D brain PET using a dual energy window method. *Phys Med Biol* 1996;41:2757-74.
- [22] Levin CS, Dahlbom M, and Hoffman EJ. A Monte Carlo correction for the effect of Compton scattering in 3-D PET brain imaging. *Nuclear Science, IEEE Transactions on* 1995;42:1181-5.
- [23] Bentourkia M, Msaki P, Cadorette J, and Lecomte R. Object and detector scatter-function dependence on energy and position in high resolution PET. *Nuclear Science, IEEE Transactions on* 1995;42:1162-7.
- [24] Bailey DL and Meikle SR. A convolution-subtraction scatter correction method for 3D PET. *Phys Med Biol* 1994;39:411-24.
- [25] Bergstrom M, Eriksson L, Bohm C, Blomqvist G, and Litton J. Correction for Scattered Radiation in a Ring Detector Positron Camera by Integral Transformation of the Projections. *Journal of Computer Assisted Tomography* 1983;7.
- [26] Stearns CW. Scatter Correction Method for 3D PET using 2D Fitted Gaussian Functions. *J. Nucl. Med* 1995;36:105P.

- [27] Watson CC, Newport D, Casey ME, deKemp RA, Beanlands RS, and Schmand M. Evaluation of simulation-based scatter correction for 3-D PET cardiac imaging. *Nuclear Science, IEEE Transactions on* 1997;44:90-7.
- [28] Bailey DL and Meikle SR. A convolution-subtraction scatter correction method for 3D PET. *Physics in Medicine and Biology* 1994;39:411-24.
- [29] Iatrou M, Manjeshwar RM, Ross SG, Thielemans K, and Stearns CW. 3D implementation of Scatter Estimation in 3D PET. *Nuclear Science Symposium Conference Record, 2006. IEEE; 2006*, p. 2142-5.
- [30] Karp JS, Muehllehner G, Qu H, and Yan XH. Singles transmission in volume-imaging PET with a ^{137}Cs source. *Phys Med Biol* 1995;40:929-44.
- [31] Yu SK and Nahmias C. Single-photon transmission measurements in positron tomography using ^{137}Cs . *Phys Med Biol* 1995;40:1255-66.
- [32] Bacharach SL. PET/CT Attenuation Correction: Breathing Lessons. *J Nucl Med* 2007;48:677-9.
- [33] Kinahan PE, Townsend DW, Beyer T, and Sashin D. Attenuation correction for a combined 3D PET/CT scanner. *Med Phys* 1998;25:2046-53.
- [34] Di Carli MF, Lipton MJ, and MyiLibrary Ltd. *Cardiac PET and PET/CT imaging*, New York, NY: Springer,2007.
- [35] Ramachandran GN and Lakshminarayanan AV. Three-dimensional reconstruction from radiographs and electron micrographs: application of convolutions instead of Fourier transforms. *Proc Natl Acad Sci U S A* 1971;68:2236-40.

- [36] Prince JL and Links JM. Medical imaging signals and systems, Upper Saddle River, NJ: Pearson Prentice Hall,2006.
- [37] Lange K and Carson R. EM reconstruction algorithms for emission and transmission tomography. J Comput Assist Tomogr 1984;8:306-16.
- [38] Hudson HM and Larkin RS. Accelerated image reconstruction using ordered subsets of projection data. IEEE Trans Med Imaging 1994;13:601-9.
- [39] Hoffman EJ, Phelps ME, Wisenberg G, Schelbert HR, and Kuhl DE. Electrocardiographic gating in positron emission computed tomography. J Comput Assist Tomogr 1979;3:733-9.
- [40] Yamashita K, Tamaki N, Yonekura Y, Ohtani H, Saji H, Mukai T, et al. Quantitative analysis of regional wall motion by gated myocardial positron emission tomography: validation and comparison with left ventriculography. J Nucl Med 1989;30:1775-86.
- [41] Boucher L, Rodrigue S, Lecomte R, and Benard F. Respiratory gating for 3-dimensional PET of the thorax: feasibility and initial results. J Nucl Med 2004;45:214-9.
- [42] Nehmeh SA, Erdi YE, Ling CC, Rosenzweig KE, Schoder H, Larson SM, et al. Effect of respiratory gating on quantifying PET images of lung cancer. J Nucl Med 2002;43:876-81.
- [43] Nehmeh SA, Erdi YE, Pan T, Pevsner A, Rosenzweig KE, Yorke E, et al. Four-dimensional (4D) PET/CT imaging of the thorax. Med Phys 2004;31:3179-86.
- [44] Klein GJ, Reutter BW, Ho MH, Reed JH, and Huesman RH. Real-time system for respiratory-cardiac gating in positron tomography. Nuclear Science, IEEE Transactions on 1998;45:2139-43.

- [45] Klein GJ, Reutter RW, and Huesman RH. Four-dimensional affine registration models for respiratory-gated PET. Nuclear Science, IEEE Transactions on 2001;48:756-60.
- [46] Ohara K, Okumura T, Akisada M, Inada T, Mori T, Yokota H, et al. Irradiation synchronized with respiration gate. Int J Radiat Oncol Biol Phys 1989;17:853-7.
- [47] Kubo HD and Hill BC. Respiration gated radiotherapy treatment: a technical study. Phys Med Biol 1996;41:83-91.
- [48] Hanley J, Debois MM, Mah D, Mageras GS, Raben A, Rosenzweig K, et al. Deep inspiration breath-hold technique for lung tumors: the potential value of target immobilization and reduced lung density in dose escalation. International Journal of Radiation Oncology*Biology*Physics 1999;45:603-11.
- [49] Inada T, Tsuji H, Hayakawa Y, Maruhashi A, and Tsujii H. [Proton irradiation synchronized with respiratory cycle]. Nippon Igaku Hoshasen Gakkai Zasshi 1992;52:1161-7.
- [50] Schleyer PJ, O'Doherty MJ, Barrington SF, and Marsden PK. Retrospective data-driven respiratory gating for PET/CT. Phys Med Biol 2009;54:1935-50.
- [51] Buther F, Dawood M, Stegger L, Wubbeling F, Schafers M, Schober O, et al. List mode-driven cardiac and respiratory gating in PET. J Nucl Med 2009;50:674-81.
- [52] Visvikis D, Barret O, Fryer T, Turzo A, Lamare F, Cheze Le Rest C, et al. A posteriori respiratory motion gating of dynamic PET images. Nuclear Science Symposium Conference Record, 2003 IEEE; 2003, p. 3276-80 Vol.5.

- [53] Hutchins GD, Caraher JM, and Raylman RR. A region of interest strategy for minimizing resolution distortions in quantitative myocardial PET studies. *J Nucl Med* 1992;33:1243-50.
- [54] Klein R, Lortie M, Adler A, Beanlands RS, and deKemp R. Fully Automated Software for Polar-Map Registration and Sampling from PET Images. *Nuclear Science Symposium Conference Record, 2006. IEEE; 2006, p. 3185-8.*
- [55] Tilkemeier PL, Cooke CD, Grossman GB, Jr BDM, and Ward RP. *Imaging Guidelines for Nuclear Cardiology Procedures. American Society of Nuclear Cardiology 2009.*
- [56] Cerqueira MD, Weissman NJ, Dilsizian V, Jacobs AK, Kaul S, Laskey WK, et al. Standardized Myocardial Segmentation and Nomenclature for Tomographic Imaging of the Heart: A Statement for Healthcare Professionals From the Cardiac Imaging Committee of the Council on Clinical Cardiology of the American Heart Association. *Circulation* 2002;105:539-42.
- [57] Buzug TM. *Computed tomography : from photon statistics to modern cone-beam CT, Berlin: Springer,2008.*
- [58] Pan T, Lee TY, Rietzel E, and Chen GT. 4D-CT imaging of a volume influenced by respiratory motion on multi-slice CT. *Med Phys* 2004;31:333-40.
- [59] Pan T, Sun X, and Luo D. Improvement of the cine-CT based 4D-CT imaging. *Medical Physics* 2007;34:4499-503.
- [60] West JB. *Respiratory physiology-- the essentials. 5th ed., Baltimore: Williams & Wilkins,1995.*

- [61] Wang Y, Riederer SJ, and Ehman RL. Respiratory motion of the heart: kinematics and the implications for the spatial resolution in coronary imaging. *Magn Reson Med* 1995;33:713-9.
- [62] McQuaid SJ and Hutton BF. Sources of attenuation-correction artefacts in cardiac PET/CT and SPECT/CT. *Eur J Nucl Med Mol Imaging* 2008;35:1117-23.
- [63] Kamel E, Hany TF, Burger C, Treyer V, Lonn AH, von Schulthess GK, et al. CT vs ⁶⁸Ge attenuation correction in a combined PET/CT system: evaluation of the effect of lowering the CT tube current. *Eur J Nucl Med Mol Imaging* 2002;29:346-50.
- [64] Ter-Pogossian MM, Bergmann SR, and Sobel BE. Influence of cardiac and respiratory motion on tomographic reconstructions of the heart: implications for quantitative nuclear cardiology. *J Comput Assist Tomogr* 1982;6:1148-55.
- [65] McCord ME, Bacharach SL, Bonow RO, Dilsizian V, Cuocolo A, and Freedman N. Misalignment between PET transmission and emission scans: its effect on myocardial imaging. *J Nucl Med* 1992;33:1209-14; discussion 14-5.
- [66] Osman MM, Cohade C, Nakamoto Y, and Wahl RL. Respiratory motion artifacts on PET emission images obtained using CT attenuation correction on PET-CT. *Eur J Nucl Med Mol Imaging* 2003;30:603-6.
- [67] Martinez-Moller A, Souvatzoglou M, Navab N, Schwaiger M, and Nekolla SG. Artifacts from misaligned CT in cardiac perfusion PET/CT studies: frequency, effects, and potential solutions. *J Nucl Med* 2007;48:188-93.

- [68] Le Meunier L, Maass-Moreno R, Carrasquillo JA, Dieckmann W, and Bacharach SL. PET/CT imaging: effect of respiratory motion on apparent myocardial uptake. *J Nucl Cardiol* 2006;13:821-30.
- [69] Gould KL, Pan T, Loghin C, Johnson NP, Guha A, and Sdringola S. Frequent diagnostic errors in cardiac PET/CT due to misregistration of CT attenuation and emission PET images: a definitive analysis of causes, consequences, and corrections. *J Nucl Med* 2007;48:1112-21.
- [70] de Juan R, Seifert B, Berthold T, von Schulthess GK, and Goerres GW. Clinical evaluation of a breathing protocol for PET/CT. *Eur Radiol* 2004;14:1118-23.
- [71] Khurshid K, McGough RJ, and Berger K. Automated cardiac motion compensation in PET/CT for accurate reconstruction of PET myocardial perfusion images. *Phys Med Biol* 2008;53:5705-18.
- [72] Hong T-P and Lee C-Y. Induction of fuzzy rules and membership functions from training examples. *Fuzzy Sets and Systems* 1996;84:33-47.
- [73] Canny J. A computational approach to edge detection. *IEEE Trans. Pattern Anal. Mach. Intell.* 1986;8:679-98.
- [74] Pan T, Mawlawi O, Luo D, Liu HH, Chi PC, Mar MV, et al. Attenuation correction of PET cardiac data with low-dose average CT in PET/CT. *Med Phys* 2006;33:3931-8.
- [75] Pan T, Mawlawi O, Nehmeh SA, Erdi YE, Luo D, Liu HH, et al. Attenuation correction of PET images with respiration-averaged CT images in PET/CT. *J Nucl Med* 2005;46:1481-7.

- [76] Cook RAH, Carnes G, Lee T-Y, and Wells RG. Respiration-Averaged CT for Attenuation Correction in Canine Cardiac PET/CT. *J Nucl Med* 2007;48:811-8.
- [77] Alessio AM, Kohlmyer S, Branch K, Chen G, Caldwell J, and Kinahan P. Cine CT for Attenuation Correction in Cardiac PET/CT. *J Nucl Med* 2007;48:794-801.
- [78] Manjeshwar R, Xiaodong T, Asma E, and Thielemans K. Motion compensated image reconstruction of respiratory gated PET/CT. *Biomedical Imaging: Nano to Macro, 2006. 3rd IEEE International Symposium on; 2006, p. 674-7.*
- [79] Qiao F, Pan T, Clark JW, Jr., and Mawlawi OR. A motion-incorporated reconstruction method for gated PET studies. *Phys Med Biol* 2006;51:3769-83.
- [80] Dawood M, Lang N, Jiang X, and Schafers KP. Lung motion correction on respiratory gated 3-D PET/CT images. *IEEE Trans Med Imaging* 2006;25:476-85.
- [81] Klein GJ, Reutter BW, and Huesman RH. Non-rigid summing of gated PET via optical flow. *Nuclear Science, IEEE Transactions on* 1997;44:1509-12.
- [82] Dawood M, Buther F, Jiang X, and Schafers KP. Respiratory motion correction in 3-D PET data with advanced optical flow algorithms. *IEEE Trans Med Imaging* 2008;27:1164-75.
- [83] Slomka PJ, Nishina H, Berman DS, Kang X, Akincioglu C, Friedman JD, et al. "Motion-frozen" display and quantification of myocardial perfusion. *J Nucl Med* 2004;45:1128-34.
- [84] Germano G, Kavanagh PB, Su HT, Mazzanti M, Kiat H, Hachamovitch R, et al. Automatic reorientation of three-dimensional, transaxial myocardial perfusion SPECT images. *J Nucl Med* 1995;36:1107-14.

- [85] Segars WP and Tsui BMW. Study of the efficacy of respiratory gating in myocardial SPECT using the new 4-D NCAT phantom. Nuclear Science, IEEE Transactions on 2002;49:675-9.
- [86] Meyer C, Weibrecht M, and Peligrad DN. Variation of Kinetic Model Parameters Due to Input Peak Distortions and Noise in Simulated ^{82}Rb PET Perfusion Studies. Nuclear Science Symposium Conference Record, 2006. IEEE; 2006, p. 2703-7.
- [87] Shkvorets M, deKemp RA, and Wells RG. Respiratory-motion errors in quantitative myocardial perfusion with PET/CT. Nuclear Science Symposium Conference Record, 2007. NSS '07. IEEE; 2007, p. 3946-50.
- [88] Lortie M, Beanlands RS, Yoshinaga K, Klein R, Dasilva JN, and DeKemp RA. Quantification of myocardial blood flow with ^{82}Rb dynamic PET imaging. Eur J Nucl Med Mol Imaging 2007;34:1765-74.
- [89] Haynor DR, Harrison RL, and Lewellen TK. The use of importance sampling techniques to improve the efficiency of photon tracking in emission tomography simulations. Med Phys 1991;18:990-1001.
- [90] Livieratos L, Rajappan K, Stegger L, Schafers K, Bailey DL, and Camici PG. Respiratory gating of cardiac PET data in list-mode acquisition. Eur J Nucl Med Mol Imaging 2006;33:584-8.
- [91] Meikle SR, Dahlbom M, and Cherry SR. Attenuation Correction Using Count-Limited Transmission Data in Positron Emission Tomography. J Nucl Med 1993;34:143-50.

- [92] Bradfield JW, Beck G, and Vecht RJ. Left ventricular apical thin point. *Br Heart J* 1977;39:806-9.
- [93] Links JM, Becker LC, and Anstett F. Clinical significance of apical thinning after attenuation correction. *J Nucl Cardiol* 2004;11:26-31.
- [94] Rahmim A, Tang J, and Zaidi H. Four-dimensional (4D) image reconstruction strategies in dynamic PET: beyond conventional independent frame reconstruction. *Med Phys* 2009;36:3654-70.
- [95] Reader AJ, Matthews JC, Sureau FC, Comtat C, Trebossen R, and Buvat I. Iterative Kinetic Parameter Estimation within Fully 4D PET Image Reconstruction. *Nuclear Science Symposium Conference Record, 2006. IEEE; 2006, p. 1752-6.*
- [96] Knesaurek K, Machac J, and Zhang Z. Repeatability of regional myocardial blood flow calculation in ^{82}Rb PET imaging. *BMC Med Phys* 2009;9:2.
- [97] Manabe O, Yoshinaga K, Katoh C, Naya M, deKemp RA, and Tamaki N. Repeatability of rest and hyperemic myocardial blood flow measurements with ^{82}Rb dynamic PET. *J Nucl Med* 2009;50:68-71.
- [98] Wells R. Phase-specific CT alignment reduces respiratory errors in NH_3 PET perfusion imaging. *J NUCL MED MEETING ABSTRACTS* 2009;50:347-.
- [99] Le Meunier L, Slomka P, Fermin J, Huber B, Cheng V, Tamarappoo B, et al. Motion frozen of dual gated (cardiac and respiratory) PET images. *J NUCL MED MEETING ABSTRACTS* 2009;50:1474-.